Yun, Jae-Yul

BAROCLINIC INSTABILITIES OF NONZONAL OCEAN CURRENTS WITH APPLICATION TO THE KUROSHIO EXTENSION CURRENT

University of Hawaii PH.D. 1986

PLEASE NOTE:

In all cases this material has been filmed in the best possible way from the available copy. Problems encountered with this document have been identified here with a check mark __✓__.

1. Glossy photographs or pages _____
2. Colored illustrations, paper or print _____
3. Photographs with dark background __✓__
4. Illustrations are poor copy _____
5. Pages with black marks, not original copy _____
6. Print shows through as there is text on both sides of page _____
7. Indistinct, broken or small print on several pages __✓__
8. Print exceeds margin requirements _____
9. Tightly bound copy with print lost in spine _____
10. Computer printout pages with indistinct print _____
11. Page(s) _____ lacking when material received, and not available from school or author.
12. Page(s) _____ seem to be missing in numbering only as text follows.
13. Two pages numbered _____. Text follows.
14. Curling and wrinkled pages _____
15. Dissertation contains pages with print at a slant, filmed as received __✓__
16. Other _____

_____

_____

University
Microfilms
International

BAROCLINIC INSTABILITIES OF NONZONAL OCEAN CURRENTS WITH APPLICATION TO THE KUROSHIO EXTENSION CURRENT

A DISSERTATION SUBMITTED TO THE GRADUATE DIVISION OF THE UNIVERSITY OF HAWAII IN PARTIAL FULFILLMENT OF THE REQUIREMENTS FOR THE DEGREE OF

DOCTOR OF PHILOSOPHY

IN OCEANOGRAPHY

DECEMBER 1986

by

Jae-Yul Yun

Dissertation committee:

Lorenz Magaard, Chairman
Wan-Cheng Chiu
Peter Muller
James M. Price
Klaus Wyrtki

ACKNOWLEDGEMENTS

I wish to express my deep appreciation to the members of my committee and Dr. Dennis W. Moore for their helpful comments and discussions. I would especially like to thank Dr. Lorenz Magaard for his assistance and guidance throughout the course of my dissertation. Without his help, this work would have never been brought to completion. Special thanks are also due Dr. Klaus Wyrtki for his financial support during the first and last parts of the graduate school and Dr. James M. Price for his helpful corrections and suggestions in finalizing this work.

This research has been supported by the Office of Naval Research. This support is gratefully acknowledged.

ABSTRACT

Using the TRANSPAC XBT data at a depth of 300 m, the regional variability of energy, time scales, length scales, and phase propagation of internal temperature fluctuations in the mid-latitude North Pacific was examined. The results showed that the regional variability in the eastern half of the basin is substantially different from that in the western half.

In the eastern North Pacific, the energy of the internal temperature fluctuations is very low and fairly uniformly distributed. Time and meridional length scales are distributed over broad ranges, zonal length scales are relatively small, and the direction of phase propagation is almost due west. At the eastern boundary, the opposite tendency in time and length scale distribution holds.

In contrast, the energy in the western North Pacific is high, particularly along the main axis of the Kuroshio Extension Current (KEC), and decreases towards the east. It also decreases towards the north and south, with length scales of decay of about 1000 km. Time scales are small near the western boundary and increase eastward. Both zonal and meridional length scales are large near the western boundary and decrease eastward. Phase propagation along the KEC appeared to be eastward, while that in the outer regions north and south of the KEC seemed to be westward with

poleward components to the north and south, respectively.

In an attempt to explain these observed characteristics, three independent studies of baroclinic instabilities of nonzonal currents have been conducted. First, local baroclinic instability of nonzonal currents was explored. It was found that time scales are smaller, length scales are larger, and eastward phase speeds are higher whenever there were larger vertical shears, and/or more meridional orientations of the mean flow and propagating wave, and/or a less stable stratification. Secondly, radiation of energy from a mesoscale disturbance traveling along a nonzonal current was studied to determine the length scale of decay and also to determine any differences in radiation between a zonal and nonzonal flow (cf, Pedlosky, 1977). The results showed that the region in period-wavelength space where radiation occurs is much larger in the nonzonal cases than in the zonal case. Furthermore, in the nonzonal cases, the broad ranges of periods and wavelengths of the disturbance overlap the observed ranges. Lastly, radiating instability of zonal and nonzonal currents was explored, using a more realistic flow structure than was used in the second study. This more elaborate theory extended an earlier analysis of the purely zonal case (Talley, 1982). It was found that the nonzonal cases (30^{o} and 60^{o} mean flows) actually show better agreement with the observations than the zonal case.

TABLE OF CONTENTS

LIST OF TABLES

LIST OF ILLUSTRATIONS

PREFACE

For the past decade Professor Lorenz Magaard and his colleagues in the Department of Oceanography at the University of Hawaii have been actively involved in observational and theoretical studies of baroclinic Rossby waves in the North Pacific. They found that a major portion of the observed internal temperature fluctuations can be explained by the presence of baroclinic Rossby waves. The investigation herein is an extension of their research effort.

Performing various analyses on the TRANSPAC XBT data, provided by Dr. Warren White of the Scripps Institution of Oceanography, I found that in the eastern North Pacific internal temperature fluctuations can be explained by means of baroclinic Rossby waves over a broad range of frequencies. However, in the western North Pacific the analyses showed results different from earlier studies. In this region the distributions of energy, time scales, length scales, and phase propagation of internal temperature fluctuations show entirely different trends from those in the eastern North Pacific. Apparently, the observed characteristics in the western North Pacific cannot be totally explained by means of Rossby waves.

What then are the processes underlying the observed characteristics ? This was an intriguing question to me,

and I decided to investigate generation mechanisms that might be responsible for the observed internal temperature fluctuations in the mid-latitude western North Pacific.

It is well known that there are different generation mechanisms in different areas. Such mechanisms can be categorized as direct atmospheric forcing, topographic forcing, and forcing by means of current instabilities. In the mid-latitude western North Pacific, however, forcing based on the instability of mean flow is obviously an important candidate as a generation mechanism. These forcings include local baroclinic instability of the strong currents, local instability in the open ocean, radiation from rings, meanders and localized unstable disturbances, and radiating instability.

Local baroclinic instability is an obvious source along strong currents like the Kuroshio Extension Current (KEC). Hence, local baroclinic instability of a mean flow was chosen as the first theoretical task in an effort to explain the observed time scales, length scales and phase propagation of internal temperature fluctuations. However, the KEC exists in a rather narrow strip, and the conditions necessary for local baroclinic instability rarely exist in the open ocean. Furthermore, the energy of the internal temperature fluctuations has a maximum located at 35-36^{o}N and minima at about 45^{o}N and 25^{o}N, indicating a length scale of decay of about 1000 km. It seems that the local

baroclinic instability cannot be a major source responsible for such a large area of fairly energetic internal temperature fluctuations.

Another possible source of the energy manifest in the temperature fluctuations in the far-fields is radiation from unstable disturbances (Pedlosky, 1977). A model similar to Pedlosky's was applied to the KEC region as the second theoretical task. Finally, a third task sought to invoke a more realistic model of the current in a manner similar to that done by Talley (1982) in her study of radiating instabilities in zonal shear flows. Both nonzonal and zonal shear flows were investigated.

Some observations suggested that the mean flow in the mid-latitude western North Pacific may be nonzonal. Also, preliminary studies in the three tasks examining only zonal mean flows did not satisfactorily explain the observed characteristics. I therefore generalized my models to handle nonzonal mean flows and re-investigated the three tasks. Although these studies were aimed at comparing theoretical results with observations, an emphasis was placed on comparing the instability of zonal and nonzonal flows.

CHAPTER I.

SPATIAL AND TEMPORAL CHARACTERISTICS OF INTERNAL TEMPERATURE FLUCTUATIONS IN THE MID-LATITUDE NORTH PACIFIC

1. Introduction

Since the development of the TRANSPAC XBT program (White and Bernstein, 1979), many studies of the variability of energy, time scales, length scales and phase propagation of internal temperature fluctuations have been conducted. From them we have learned that the potential energy or the variance of internal temperature fluctuations is much higher in the western North Pacific, especially along the axes of the Kuroshio current system, than in the eastern North Pacific with a relatively sudden change at about 170°W (Roden, 1977; White, 1977; Wilson and Dugan, 1978; Kang and Magaard, 1980; Bernstein and White, 1981; White, 1982; Harrison et al, 1983; Mizuno and White, 1983). We also know that there are predominant interannual fluctuations (White and Walker, 1974; Price and Magaard, 1980; White, 1983) and near-annual ones with periods ranging from several months to two years (Bernstein and White, 1974; Emery and Magaard, 1976; Bernstein and White, 1981; White, 1982). This is also clearly shown in Magaard's (1983) composite model spectrum for the area of

20-25°N, 175-130°W. The most commonly observed wavelength of the internal temperature fluctuations both in the zonal and in the meridional direction is reported to be in a range of 400-1000 km (Roden, 1977; Wilson and Dugan, 1978; Kang and Magaard, 1980; Harrison et al, 1981). Phase propagation is basically westward with a speed of 1-4 cm/sec (Kang and Magaard, 1980; Bernstein and White, 1981; White, 1982). However, Mizuno and White (1984), using the same data as used in this study, found that the phase propagation is eastward along the axis of the Kuroshio Extension Current (KEC).

Although the most prominent features of internal temperature fluctuations in the mid-latitude North Pacific have already been determined in earlier studies, the regional characteristics have yet to be systematically studied. This chapter describes the results of an investigation of the geographical distribution of energy, time scales, length scales and phase propagation of the temperature fluctuations at a depth of 300 m in the mid-latitude North Pacific. Several standard analysis methods such as autocorrelation analysis, spectrum analysis, time-longitude and time-latitude contours, and harmonic analysis have been utilized.

2. The data

The investigation presented herein was based upon

temperature samples at 300 m depth, mostly from the TRANSPAC XBT program, but augmented with observations archived at the Japanese Oceanographic Data Center for the region near Japan. The individual XBT observations were first blocked in time into bins of 3-month intervals and then mapped onto a 0.5^{o} latitude by 0.5^{o} longitude grid, from the coast of Japan to the coast of California between 30^{o} and 45^{o}N. The number of total XBT observations per each 3 month interval in the study area ranged from 800 to 3300, increasing with season. The coverage in time runs from summer 1976 to spring 1980. The gridding of the seasonally blocked temperature was accomplished by fitting a linear trend surface to the nearest eight surrounding observations and then selecting the value at the grid point from this surface. This data set was produced by Dr. Warren White of the Scripps Institution of Oceanography, who made the data available for this study. Other recent investigations using this data set were conducted by White (1982) studying the eastern North Pacific (180^{o}-120^{o}W) and by Mizuno and White (1983) studying the western North Pacific (130^{o}E-170^{o}W).

3. Mean and standard deviation

Contours of the long-term (4 years) mean temperature

at a depth of 300 m (Fig. 1.1) indicate that the Kuroshio Current is oriented about 45-60° in a region south of Japan and then leaves the coast of Japan as the KEC. (The convention for direction of propagation of currents and waves used throughout this dissertation is that eastward propagation is designated by 0°, northward propagation by 90°, and so on) The mean temperature profiles indicate that the KEC may bifurcate at about 152°E, becoming two nonzonal branches. The northeastward (NE) branch is oriented about 20° (along the 6-8°C isotherms), and the southeastward (SE) branch is oriented about 330-350° (along the 11-14°C isotherms). This bifurcation of the mean flow may be triggered by the Shatsky Rise, a broad submarine ridge located near the point of bifurcation. Mean temperature gradients of about 3°C/100 km at 150°E, 1°C/100 km at 165°E along the SE branch, and 0.3°C/100 km at 160°W are seen.

Contours of the standard deviation of temperatures from the long-term mean (Fig. 1.2) show a drastic change at 173°W, along the main axis of the KEC suggesting that the vigorous current-related fluctuations terminate there. West of 173°W the standard deviation is mostly larger than 0.5°C, especially along the SE branch of the KEC. East of 173°W the standard deviation is mostly less than 0.5°C with a fairly homogeneous distribution. Along the

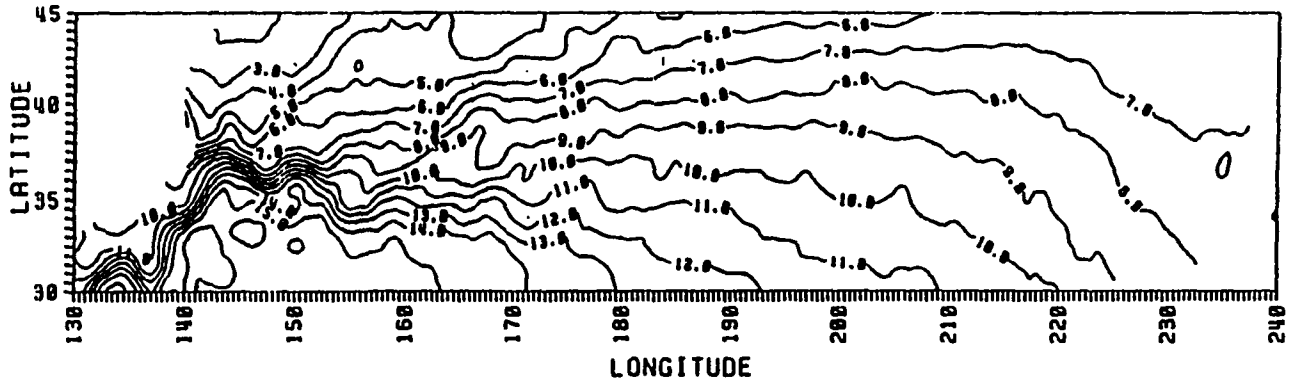

Figure 1.1 Mean temperature at 300 m depth.

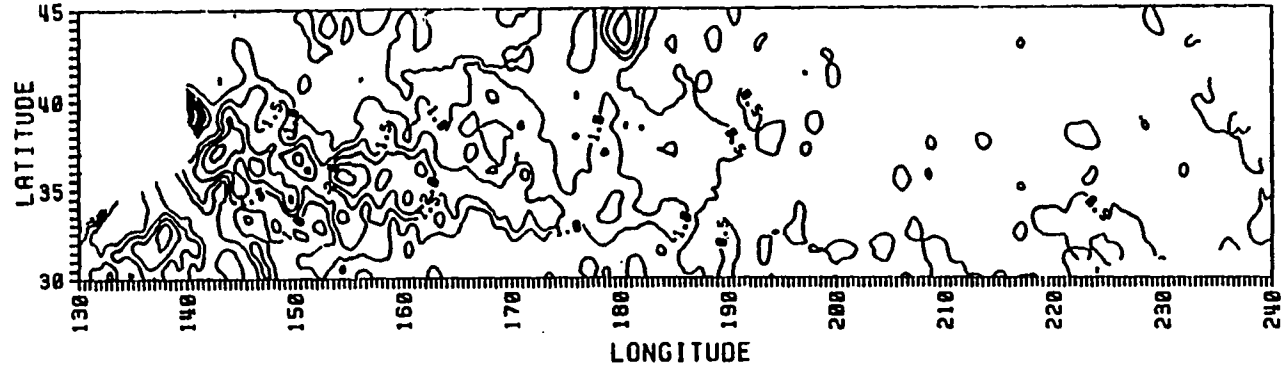

Figure 1.2 Standard deviation of the temperature fluctuations at 300 m depth.

SE branch, the standard deviation shows a distribution of highs and lows with intervals of 300-750 km between the neighboring maxima (or neighboring minima). We speculate that these intervals may be regarded as wavelengths of a fully developed, finite amplitude instability of the KEC.

The shape of the 1°C contour line of the standard deviation suggests that the energy sources are apparently located along the axes of the KEC and that the energy is transported to the east. The shape also indicates that the energy is radiated from the axes toward the north and south into the far-fields. In the far-fields there is evidence that the energy may propagate to the west as stable baroclinic Rossby waves. If areas with values of the standard deviation less than 0.5°C are regarded as areas of background fluctuations, the length scale of decay from the current-related source region to the region of the background fluctuations in the far-fields is about 1000 km.

4. Time scales

a. Autocorrelation analysis

As a preliminary step to investigate the dominant time scales manifested in the data, an autocorrelation analysis has been applied. The procedure will determine the first zero-crossing time lag (hereafter referred to as

ZXTL) at each grid point. In this analysis the time series have been used without any filtering and only grid points that have more than 12 consecutive data points are included.

As a general result, the autocorrelation functions had sharply lower values beyond the ZXTL. Therefore, one can consider the ZXTLs as decorrelation time scales. Table 1.1 displays the total number of estimated ZXTLs in each subarea (Fig. 1.3) and their distribution (in percentage of the total number) in 7 categories of time lags. The most commonly occuring ZXTL is less than three months. A comparable decorrelation time scale of about 2 months was found by Bernstein and White (1981) analyzing about 2 years of the TRANSPAC XBT data in the western North Pacific. The next most commonly occuring ZXTLs are 3 to 6 months.

The ZXTLs of less than three months occur most commonly in subareas I and VI (near both boundaries). The ZXTLs are generally more broadly distributed in lag in the interior than in the boundary region. In the interior region the ZXTLs are distributed over a narrower range in the western than in the eastern North Pacific. As one proceeds from subarea I to subarea IV, the distribution of the ZXTLs become broader with a gradual increase in number of larger time lags. However, the small ZXTLs of less than 3 months and 3 to 6 months are still dominant in subareas II and III. As one proceeds further east, from subarea IV

Table 1.1 Total number of estimated first zero-crossing time lags in each subarea and their distribution (in percentage of the total number) in 7 categories of time lags.

longitude band (total est.) / zero-crossing(months)	13°-15°E (693)	15°-17°E (989)	17°E-17°W (852)	17°-15°W (910)	15°-13°W (808)	14°-12°W (255)
	I	II	III	IV	V	VI
< 3	48	36	35	14	29	58
3-6	30	37	34	17	16	23
6-9	11	11	12	15	15	10
9-12	8	7	10	13	13	7
12-15	1	5	7	19	13	2
15-18	0	3	2	17	9	0
> 18	1	1	0	5	4	0

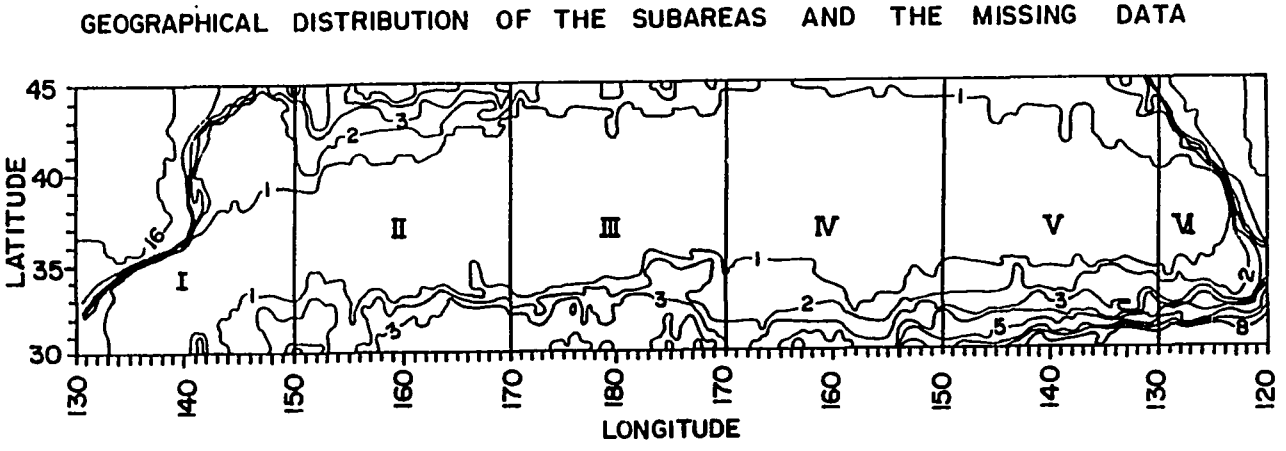

Figure 1.3 Distribution of subareas I-VI and contours indicating the numbers of the missing data point in time. Inside the label 1 there is no missing data point in time.

to the eastern boundary, the spread in time scales diminishes again.

A more detailed picture of the geographic distribution of the ZXTLs is presented by the contours of Figure 1.4. Here we see a region of larger time scales (ZXTLs 6 months and larger) between longitudes 155°-170°E, and latitudes 36°-43°N, in the northeastern branch of the KEC. This may be a consequence of the Shatsky Rise, since topography can scatter energy toward larger time scales (Rhines and Bretherton, 1974).

b. Frequency spectrum analysis

Frequency spectra have been estimated using the direct Fourier transform performed at each grid point. The Fourier coefficients were then smoothed by spatial averaging instead of a smoothing in the frequency domain, because of the small number (16) of points in time. The Fourier coefficients have been calculated from the time series at each grid point. These coefficients are averaged over each of the six subareas (Fig. 1.3), over the area west of 170°W, over the area east of 170°W, and over the entire study area. The final frequency spectra are then calculated from the spatially averaged coefficients. Therefore, a total of 9 smoothed spectra have been produced. The same estimation procedure was repeated after

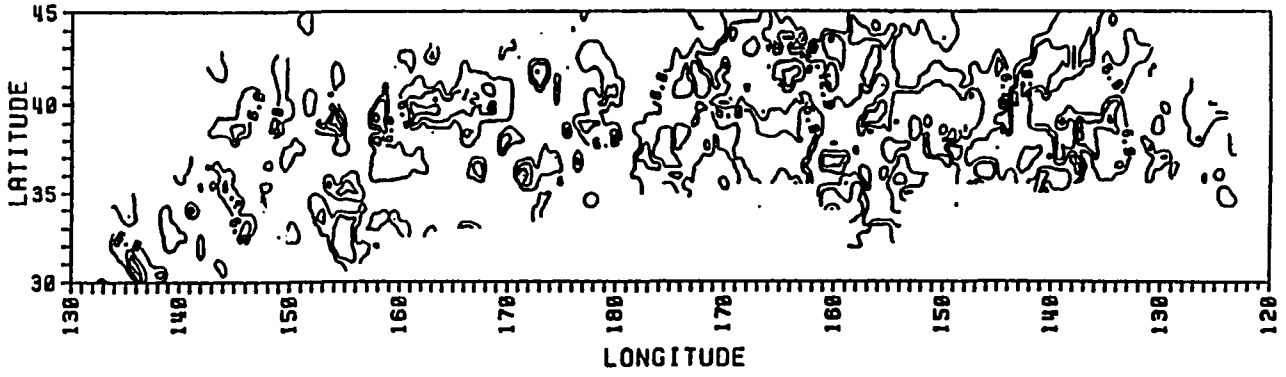

Figure 1.4 Geographical distribution of the first zero-crossing time lags [months] of the temperature at 300 m depth.

removing the linear trend in each time series to determine to what degree the linear trend affects the spectrum.

Complete, 16 points records did not exist at all grid points. Fig. 1.3 shows contours of the number of missing points. Only those records with no gaps were used in the computation of the smoothed spectra. Most of the field had records with no gaps, i.e., the area inside the 1-gap contour.

Since the data are not independent from one grid point to another, the effective number of degree of freedom has to be calculated to determine the confidence interval for each spectrum. Using the formula given by Emery and Magaard (1976), the effective number of degree of freedom was calculated for subarea I which has the smallest number of grid points (354); about 100 degree of freedom was found. Since all the other subareas contain a larger number of grid points than subarea I, the number of degree of freedom of 100 was taken for each subarea to assign 95% confidence intervals for the spectra. This was done to save much computer time, since the calculation of the number of degrees of freedom is laborious.

In the following figures, Figs. 1.5 and 1.6, the broken lines indicate the spatially smoothed spectra with the linear trends included, and the solid lines indicate those with the linear trends removed.

In subarea I, near the western boundary, the bulk of

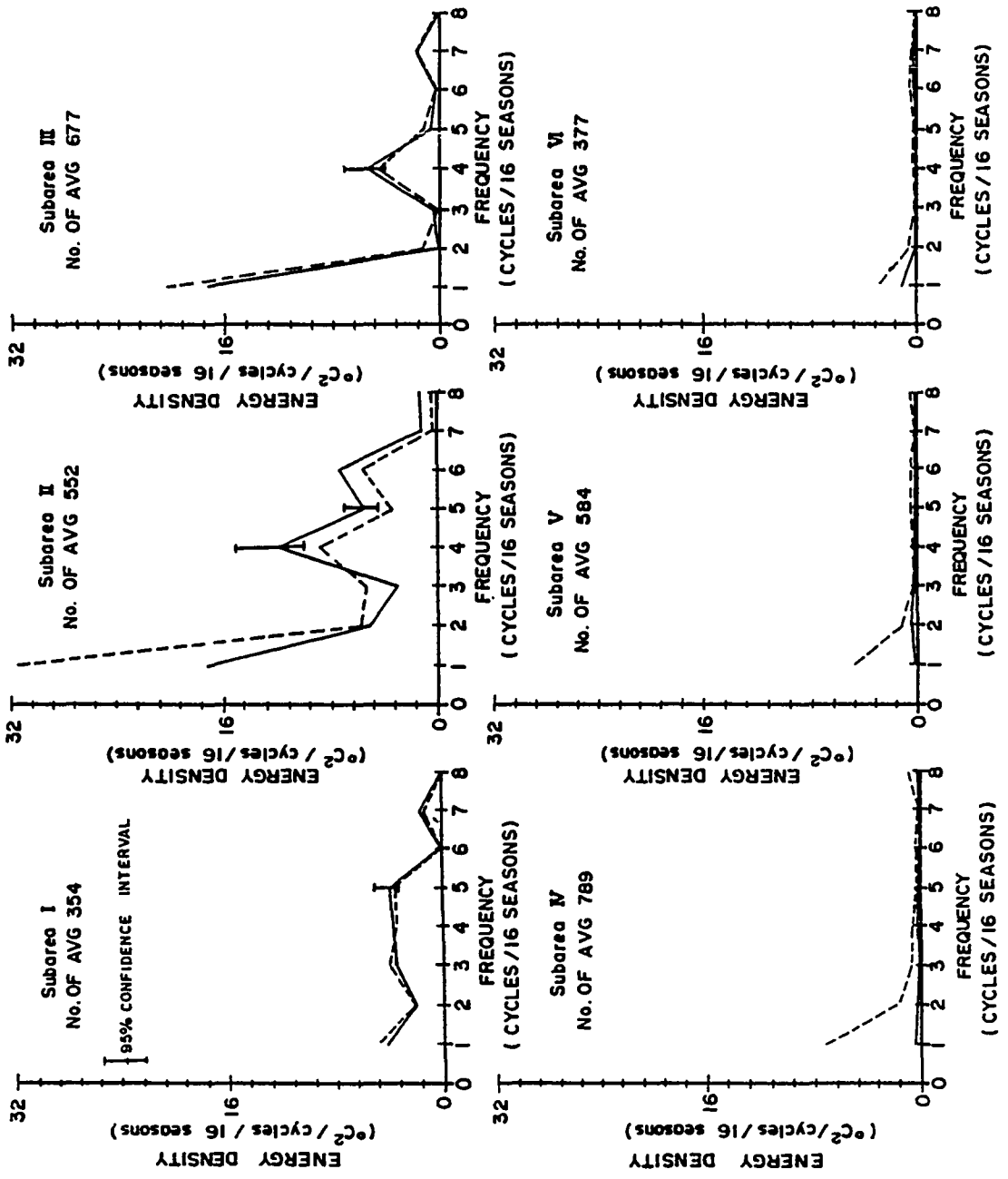

Figure 1.5 Spatially smoothed power spectra in each subarea. Solid (broken) lines indicate the spectra without (with) the linear trends.

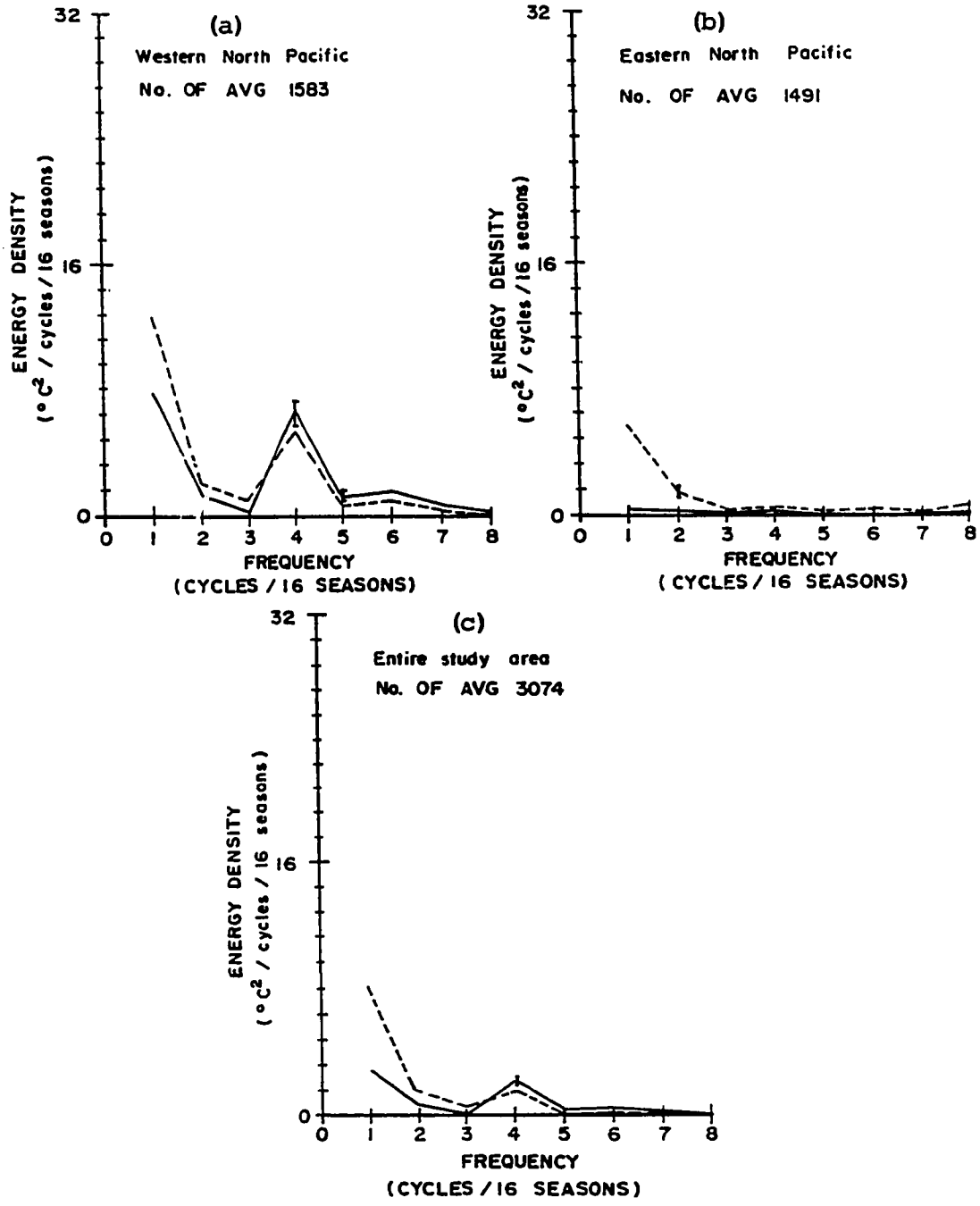

Figure 1.6 Spatially smoothed power spectra in the western half, the eastern half, and the entire study area. Solid (broken) lines indicate the spectra without (with) the linear trends.

the energy is found in the frequency range of 0.75-1.25 cycles/year (cpy) and is somewhat uniformly distributed. In this region the removal of the linear trends makes no difference for the shape of the spectra indicating a lack of very low frequency fluctuations. In subareas II and III (the interior western North Pacific) the energy levels are higher and less uniformly distributed in frequency. Distinct peaks are seen at 1 cpy both in subarea II (15% of the total energy) and in subarea III (16%). When the linear trends are removed, the peak in subarea II become larger, changing in % of the total energy content from 15% to 23% at 1 cpy, while the peak in subarea III show little change (from 16% to 21% at 1 cpy). The spectra illustrate that the linear trends account for a larger portion of the energy in subarea II than in subarea III, while the energy at the lowest frequency after the removal of the linear trend is higher in subarea III (67%) than in subarea II (33%).

In subareas IV and V (the interior eastern North Pacific) and in subarea VI (the eastern boundary), the energy level is very low at all frequencies compared to that in subareas II and III, as is anticipated from the distribution of the standard deviation. The spectra show the energy distribution over the relatively broad range of frequency. In these subareas the energy at the low frequencies decreases considerably when the linear trend is

removed; the high frequency estimates are less affected. Fluctuations of frequencies higher than the annual contribute more to the total energy in the eastern boundary than in the other subareas.

Hence, it is very clear that the spectra in subareas IV and V are distinct from those in subareas II and III. It is certain that long-term fluctuations in the eastern North Pacific are different from those in the western North Pacific. We speculate that the (comparatively) high energy at the very low frequency in subareas IV and V may indicate the existence of the same low frequency signal seen in Magaard's (1983) model spectrum. The spectra also indicate a different distribution in the small time scales.

In the more highly smoothed spectra representing the western and eastern halves of the field (Fig. 1.6a and 1.6b), one sees essentially the same structure previously explained, only with greater statistical certainty. The whole-field spectrum (Fig. 1.6c) is, as would be expected, with the dominant annual peak from the western region manifested in the whole-field average.

5. Length scales

a. Autocorrelation analysis

In a manner similar to that performed for the

investigation of the dominant time scales, the spatial autocorrelation functions in both zonal and meridional directions are computed in each subarea. The zonal first zero-crossing spcae lags (ZZXSL) are computed in each subarea from the zonal space series (40 grid points) of the temperature fluctuations at each latitude and season. The meridional zero-crossing space lags (MZXSL) are computed in each subarea from the meridional space series (30 grid points), at each longitude and season. Also, the ZZXSLs and the ZMXSLs can be regarded as the zonal and meridional decorrelation length scales as was done in the time scale analysis, since the autocorrelation functions were generally much smaller at lags larger than these scales.

Tables 1.2 and 1.3 show the total number of estimated ZZXSL and ZMXSL, respectively, in each subarea and their distribution (in percentage of the total number) in the given categories of space lags. In general, the MZXSLs are smaller than the ZZXSLs.

The distribution of ZZXSLs (Table 1.2) show a tendency towards larger length scales at the boundaries than in the interior. The most common ZZXSL in the whole field was 150-200 km. The distribution of the MZXSL (Table 1.3) in the western half of the field show a similar tendency; length sclaes get shorter towards the interior. However, the eastern boundary exhibits predominantly shorter meridional length scales.

Table 1.2 Total number of estimated zonal first zero-crossing space lags in each subarea and their distribution (in percentage of the total number) in 9 categories of space lags.

longitude band (total est.) / zero-crossing (km)	130-150E (159)	150-170E (451)	170E-170W (438)	170-150W (444)	150-130W (446)	140-120W (326)
	I	II	III	IV	V	VI
50-100	0	0	0	1	2	1
100-150	9	17	27	31	25	18
150-200	27	36	31	36	34	30
200-250	18	15	21	11	18	19
250-300	18	14	12	10	10	14
300-350	23	8	3	4	6	11
350-400	3	5	4	2	3	5
400-450	2	4	2	2	2	2
450-500	0	0	1	1	1	1

Table 1.3 Total number of estimated meridional first zero-crossing space lags in each subarea and their distribution (in percentage of the total number) in 8 categories of space lags.

longitude band (total est.) / zero-crossing (km)	140-150E (279)	150-170E (625)	170E-170W (640)	170-150W (640)	150-130W (631)	130-120W (164)
	I	II	III	IV	V	VI
50-100	1	1	2	3	7	12
100-150	21	28	38	21	39	50
150-200	25	39	31	28	28	27
200-250	46	24	19	13	12	9
250-300	7	7	8	17	10	1
300-350	0	1	1	14	2	1
350-400	0	0	1	4	1	0
400-450	0	0	0	0	1	0

b. Wavenumber spectrum analysis

Using the space series of the temperature data, wavenumber spectra are estimated by using the standard Blackman-Turkey method. For the zonal wavenumber spectra in the western North Pacific, the space series covering the distance from near Japan to the date line are used after removal of the spatial linear trends. Due to data gaps, not all records were the same length. The average record length is about 45 degrees in the zonal direction; the sampling rate is 0.5^{o}. In order to obtain composite zonal wavenumber spectra at latitudes, 30^{o}, 31^{o},.., ℓ^{o},..45^{o}, individual spectra are estimated for each season at latitudes ℓ^{o} and $(\ell+0.5)^{o}$. Then for each latitude ℓ^{o}, 32 individual spectra are averaged at each wavenumber (16 points in time x 2 latitudes = 32 spectra averaged). The effective number of degrees of freedom for the composite spectra is estimated using the formula given in Emery and Magaard (1976) and is about 60. This effective number of degree of freedom is used to determine the 95% confidence intervals in the composite spectra. The composite wavenumber spectra at several selected latitudes (33^{o}, 36^{o}, 39^{o} and 44^{o}N in the western North Pacific and 32^{o}, 35^{o}, 39^{o} and 44^{o}N in the eastern North Pacific) are shown in Figs. 1.7a and 1.7b.

The zonal wavenumber spectra in the western North

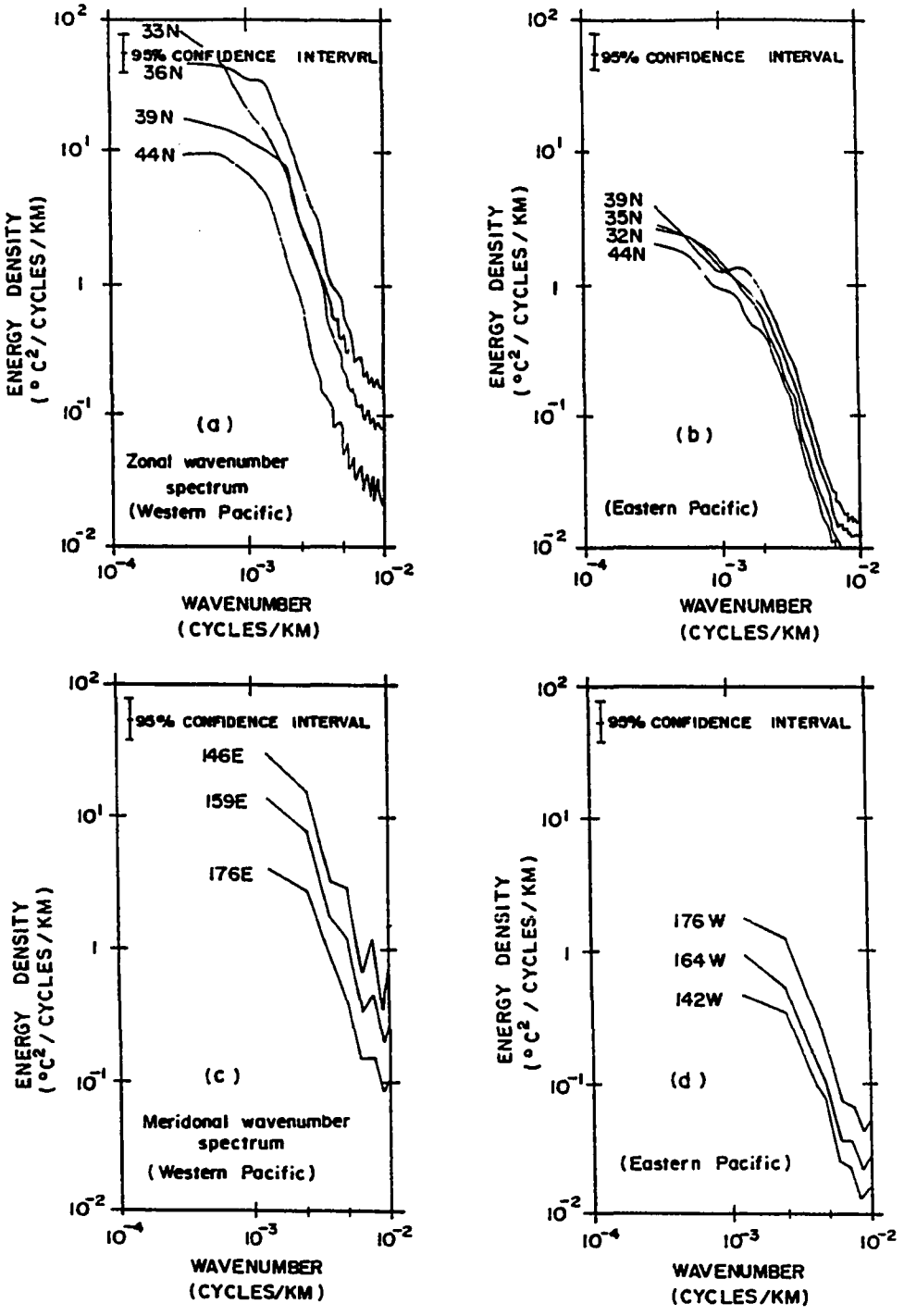

Figure 1.7 Zonal wavenumber spectra (a) at 33, 36, 39 and 44°N in the western North Pacific and (b) at 32, 35, 39 and 44°N in the eastern North Pacific. Meridional wavenumber spectra (c) at 146, 159 and 176°E, and (d) at 176, 164 and 142°W.

Pacific (Fig. 1.7a) exhibit energy levels that are highest at 35° and 36°N at most wavenumbers and lowest at all wavenumbers at 42-45°N. In the eastern North Pacific, the maximum energy levels are nearly two orders of magnitude smaller than the maximum energy in the western North Pacific. In the eastern North Pacific there is very little difference in energy levels among different latitudes. The slightly higher energy levels are at 39°N and the slightly lower ones are at 45°N in the eastern North Pacific.

The slopes of the zonal wavenumber spectra change at wavelengths of 600-750 km in the western North Pacific and at wavelengths of 420-500 km in the eastern North Pacific. The latter is less clear. The difference in the wavelengths at which the slope change occurs reflects the difference in dominant length scales. The slope changes are more gradual in the eastern than in the western North Pacific. In the western North Pacific the spectral slopes at 35-45°N are -2.7 to -3.2 (on a $\log_{10}$-$\log_{10}$ scale) at wavelengths of 100-750 km and nearly flat at wavelengths longer than 750 km. However, those at 31-35°N are -2.7 to -3.0 at wavelengths of 100-750 km and -1 to -1.2 at wavelengths longer than 750 km indicating a broader distribution of length scales at 31-35°N than at 35-45°N. The spectral slopes in the eastern North Pacific are -2.6 to -3.0 at wavelengths of 100-500 km.

Hence, they are gentler than those in the western North Pacific, indicating greater importance of the smaller scale fluctuations. The slopes at wavelengths longer than 500 km are about -1 (slightly flatter at 31-34°N) in the eastern North Pacific, comparable to those in the western half of the field.

Composite meridional wavenumber spectra are estimated using the meridional space series covering 15° of latitude. Each composite spectrum is obtained by averaging spectra over 2.5° of longitude (5 grid points) and 16 seasons. The effective number of degrees of freedom for these composite spectra is about 55. The spectra at several selected longitudes (146°, 159°, 176°E, 176°, 164° and 142°W) are shown in Figs. 1.7c and 1.7d. In the meridional wavenumber spectra the highest energy is found at 138.5-146°E at all wavenumbers.

The slopes of the spectra change at a wavelength of 400 km. Slopes of -2.5 to -3.4 are found (on a $\log_{10}$-$\log_{10}$ scale) over wavelengths of 100-400 km with steeper slopes in the west indicating more relative importance of small scale fluctuations in the east. The slopes at wavelengths longer than 400 km range from -0.4 to -1.0.

6. Phase propagation

a. Time-longitude and time-latitude contours

Time-longitude plots of the temperature variability

at each full degree of latitude are displayed to examine the direction of zonal phase propagation. Figs. 1.8a-h exhibit the contours at each odd-numbered latitude. In the figures contours sloping upward towards west indicate westward phase propagation.

In the eastern North Pacific the direction of zonal phase propagation is essentially westward except in the regions north of 44°N and near the eastern boundary. The westward phase propagation is most pronounced at 39°N with speeds of about 2 cm/sec.

In the western North Pacific the characteristics of the zonal phase propagation is more complicated. The westward phase propgagtion is relatively more evident at latitudes between 37° and 43°N and also at latitudes between 30° and 33°N. Between these zones, however, eastward propagation of phase is manifest. This had been seen earlier by Mizuno and White (1984). As in the case in the eastern half of the field, westward propagation is most pronounced at 39°N with speeds of about 2 cm/sec. Westward phase speed is seen to be higher towards the south; at 31°N, for example, the phase speed of 4.5 cm/sec is estimated over longitudes between 165°E and 168°W. The eastward phase propagation is most evident at 35°N with speeds of about 3 cm/sec.

Time-latitude plots of the temperature variability

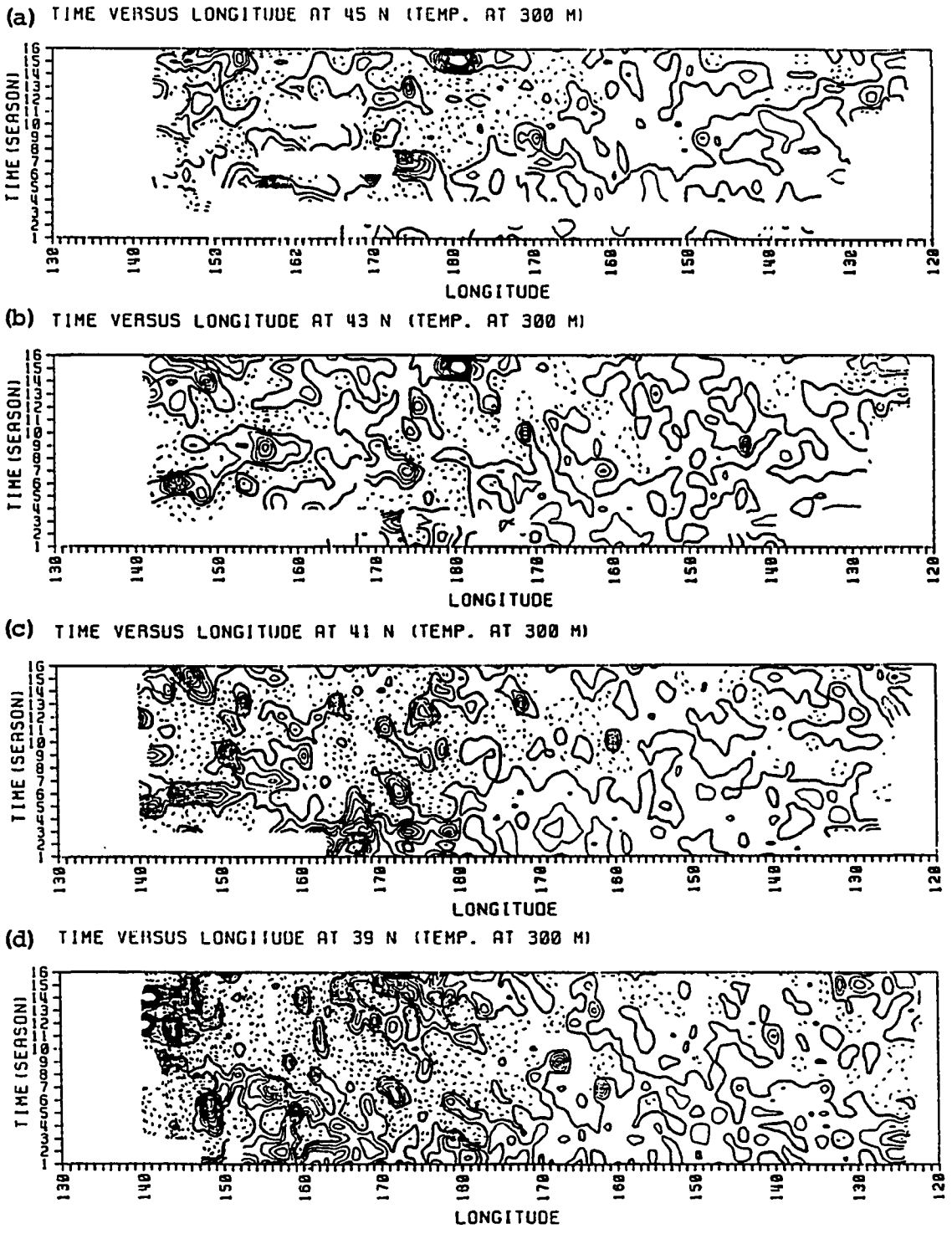

Figure 1.8 Time-longitude plots of the temperature variability at each odd-numbered latitude. The contour interval is 0.5°C.

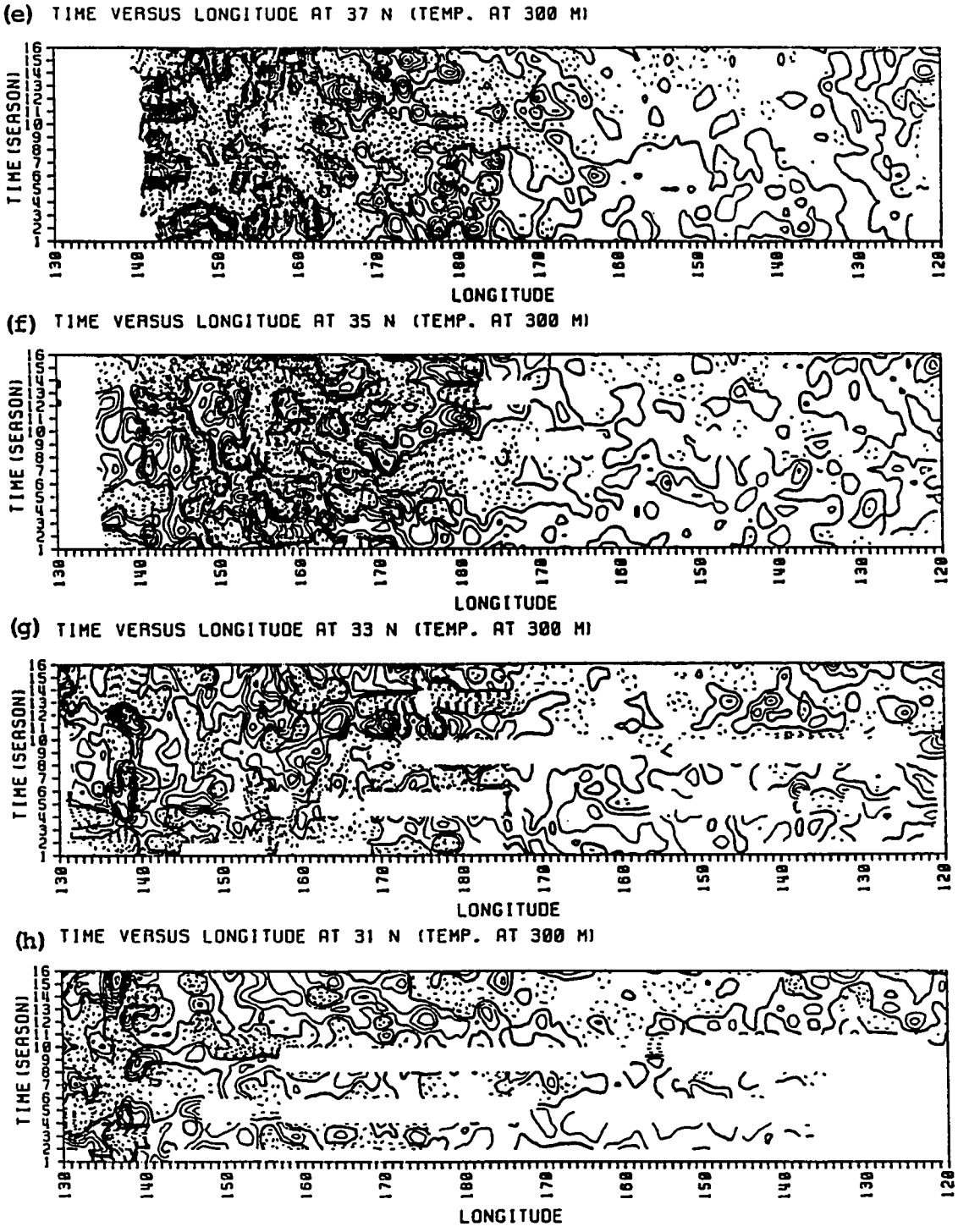

Figure 1.8 continued.

are displayed in Fig. 1.9 to examine the direction of meridional phase propagation. In this figure the contours sloping upwards towards the north indicate northward propagation. The slopes of the contours in the region 141°-171°E indicate phase propagation away from the axis of the KEC, northward and southward. A typical phase speed in both direction is approximately 1-2 cm/sec. The propagation of phase is not apparent in all seasons, i.e., not contiguous throughout the record.

b. Harmonic analysis

A 12-month harmonic was fitted to a smoothed version of the data to investigate phase propagation of the temperature fluctuations at the annual period. In order to enhance statistical significance, the original half-degree gridded data were averaged within 1° latitude by 1° longitude boxes (4 points in space) before fitting the 12-month sine curves. 20-40% of the total variance is contained in the annual harmonics (raw bandwidth of 10.7-13.7 months) of the time sequences of the western North Pacific and 10-20% from the eastern North Pacific time sequences. This is an agreement with the spectra previously computed.

The phases of the fitted harmonics have been mapped geographically to see if any systematic patterns exist that

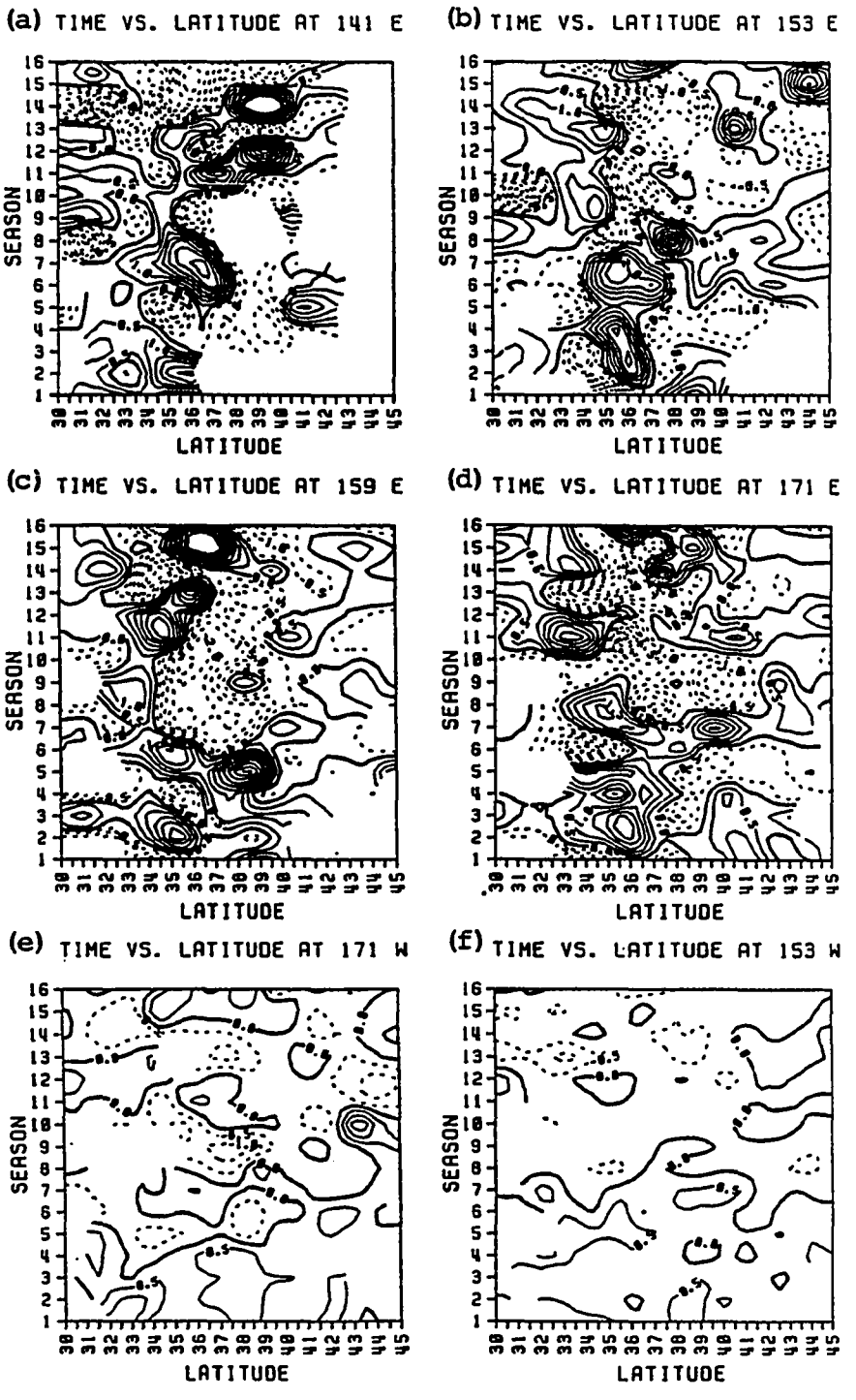

Figure 1.9 Time-latitude plots of the temperature variability at several selected longitudes. The contour interval is 0.5°C.

might indicate a propagating disturbances. Phases along zones at different latitudes are shown in Figs. 1.10a-h. Westward phase propagation can be inferred from lines sloping upward towards west. Essentially the same phase propagation is seen as was found in the time-longitude contours. The westward phase speed is roughly 2 cm/sec at latitudes north of the KEC. At 35 and 36°N, eastward phase is again seen and has a speed of about 3.8 cm/sec (Fig. 1.10f). Between 31° and 33°N, westward phase speeds are roughly 2.5-3.2 cm/sec.

Phase of the 12-month harmonic along meridions are shown in Fig. 1.11. Similarily looking curves were grouped in small block of longitude. The phases within 154-165°E show a considerably persistent pattern in which the relative minima of phase exist around 36°N, indicating northward propagation north of about 36°N and southward propagation south of about 36°N. The apparent phase speed is approximately 2.3 cm/sec in both directions. This tendency of phase propagation to the far-fields from about 36°N is apparent only in the western North Pacific. East of 165°E the direction of meridional phase propagation is not consistently northward or southward.

Contours of the phase of the annual harmonics over the entire field are displayed in Fig. 1.12. In this figure the shaded region shows phase less than 120°. There is a fairly regular pattern of high and low values in

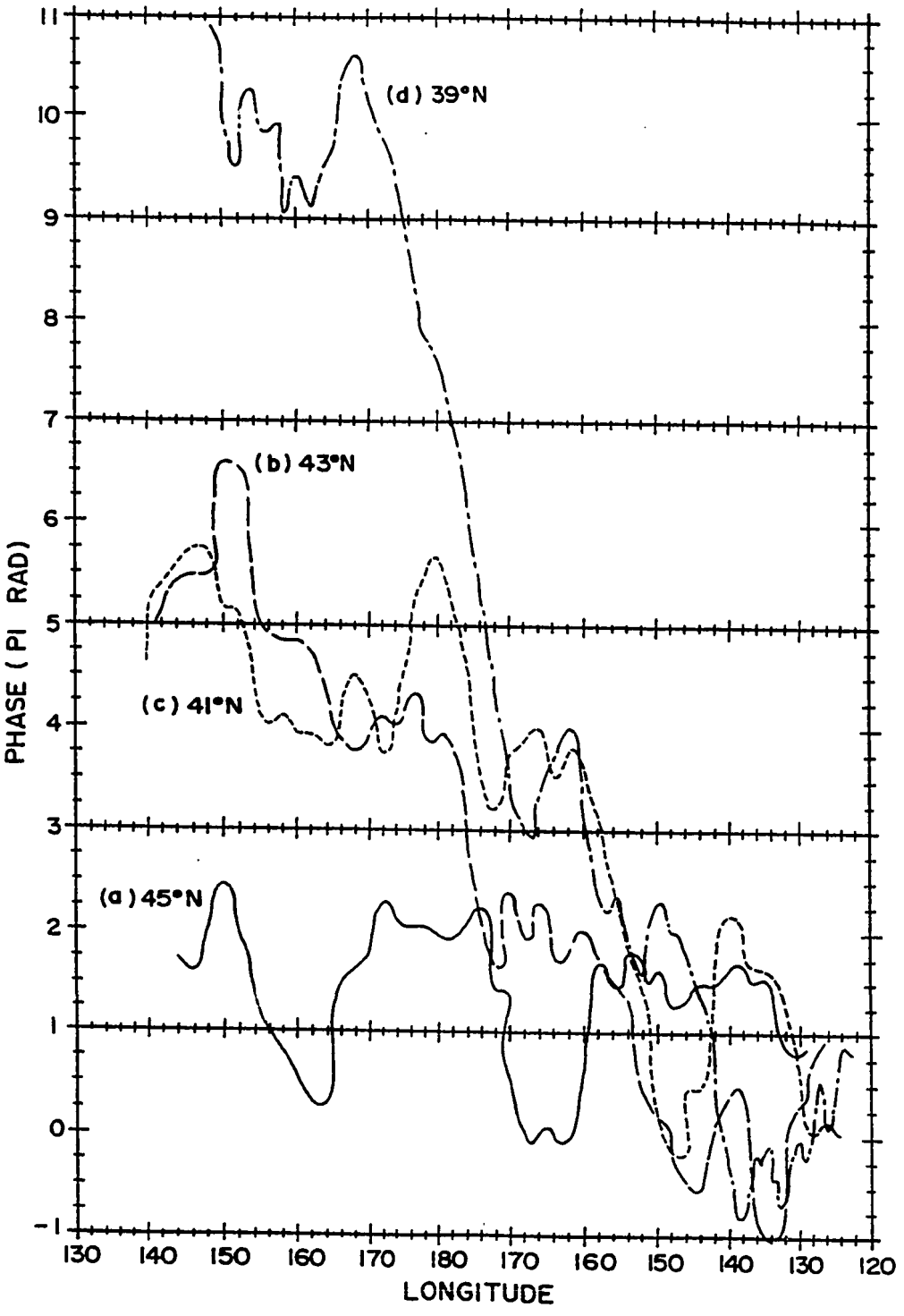

Figure 1.10 Phase of the annual harmonics along zones at latitudes of (a) 45°, (b) 43°, (c) 41°, (d) 39°, (e) 37°, (f) 35°, (g) 33°, and (h) 31°N.

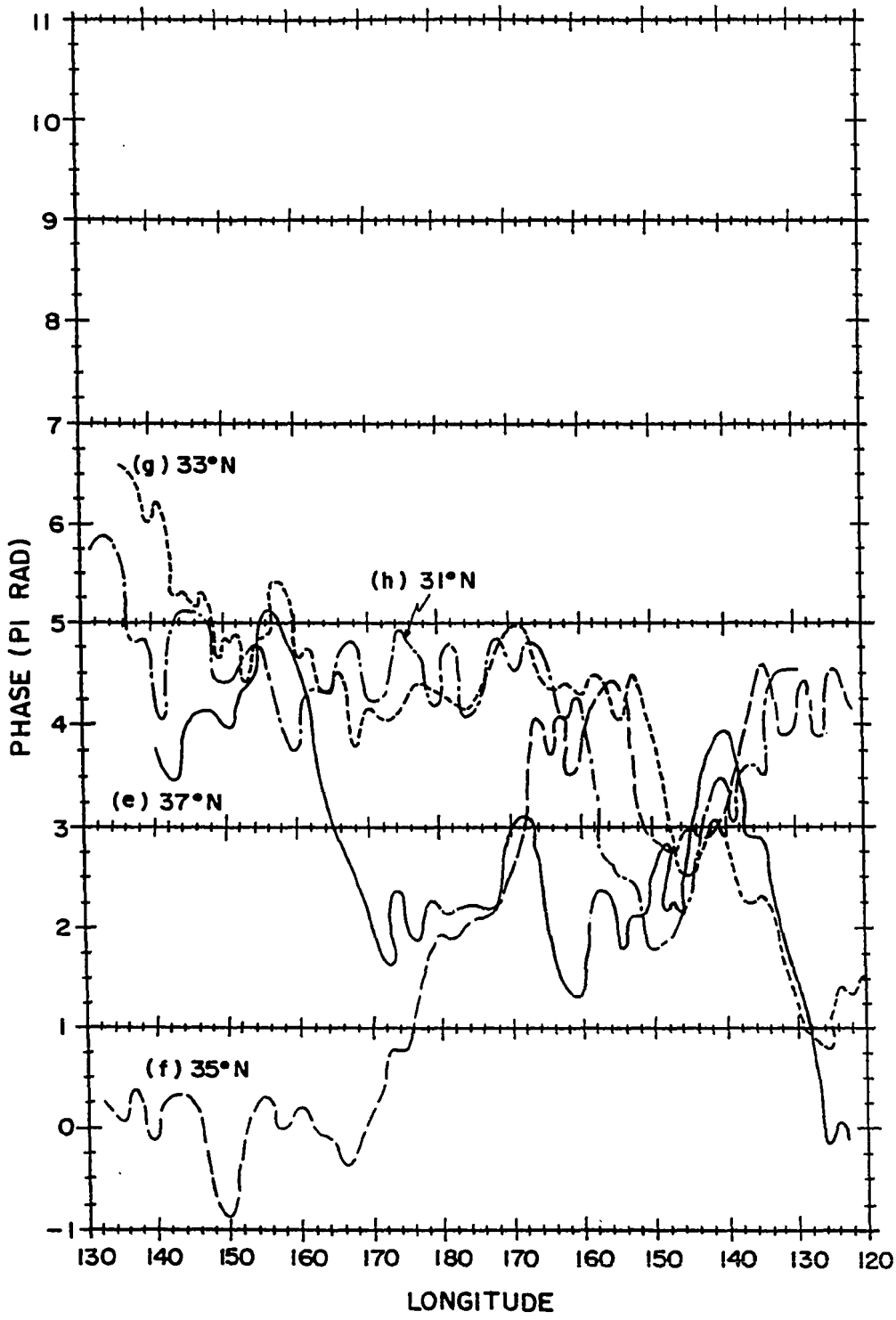

Figure 1.10 continued.

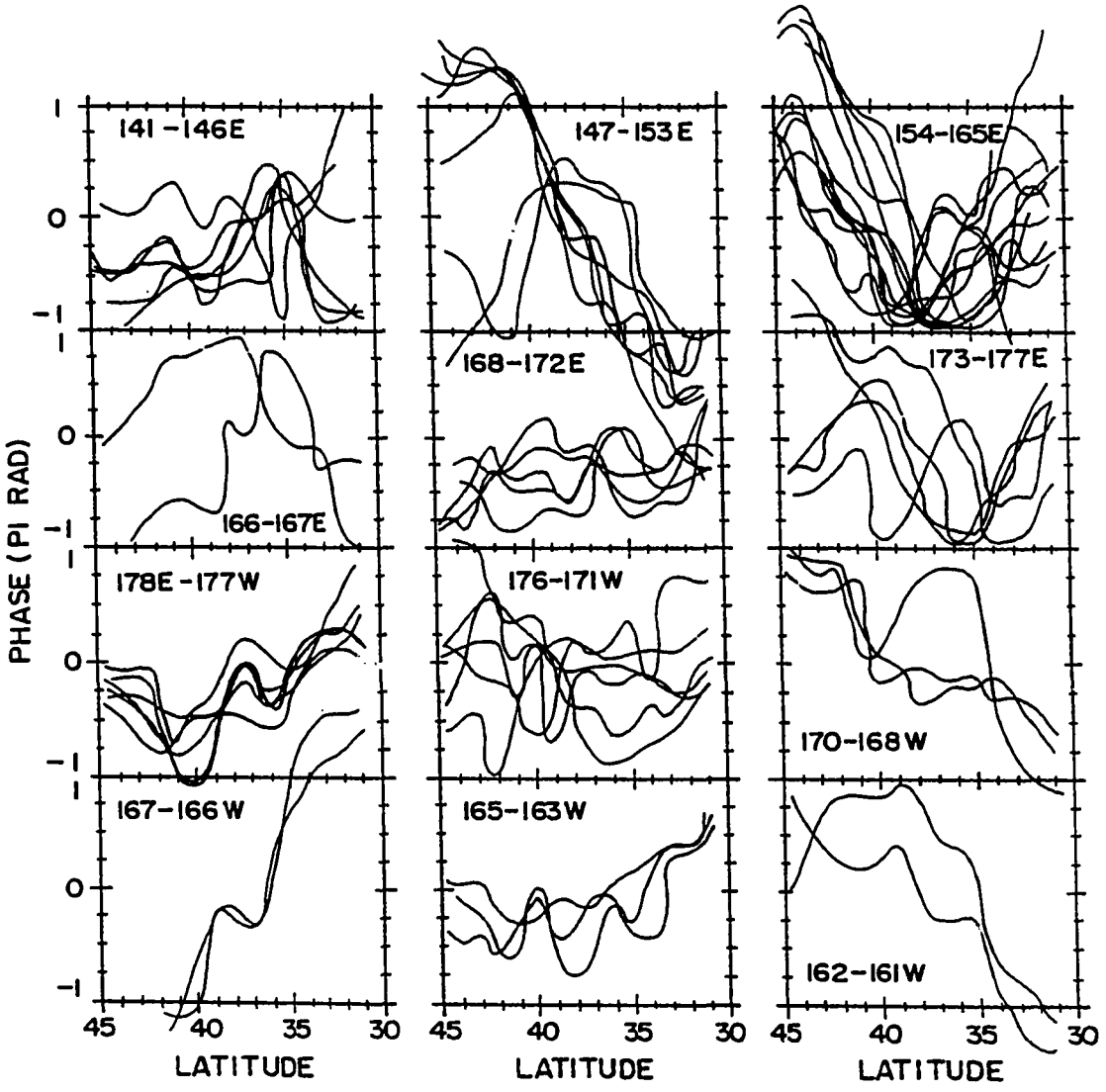

Figure 1.11 Phase of the annual harmonics along meridians at various longitudes. The range of longitudes within a box were selected to group similarly looking curves.

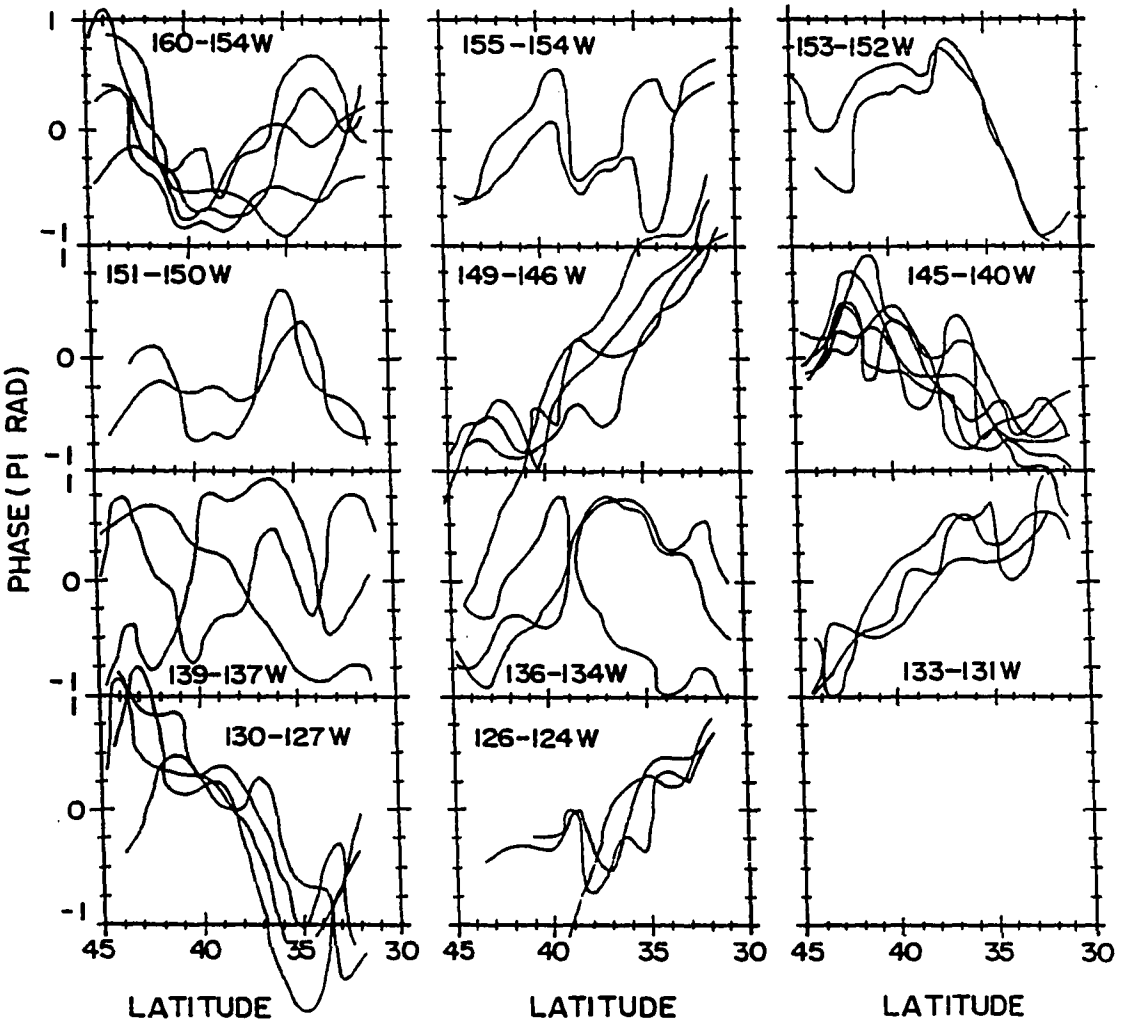

Figure 1.11 continued.

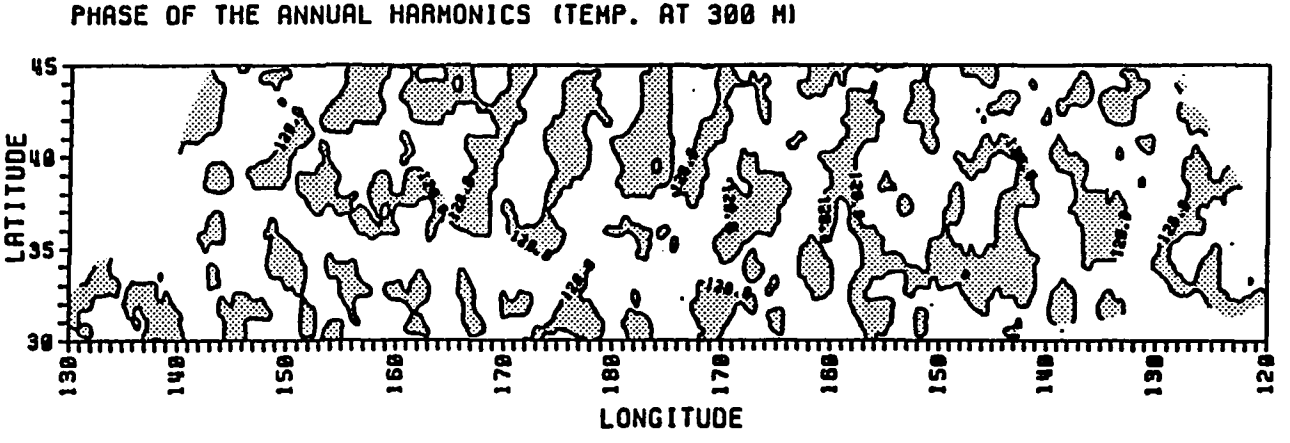

Figure 1.12 Phase of the annual harmonics in the study area. The shaded region indicates phase less than 120^{o}.

the eastern half of the field, wherein the direction of phase propagation is exclusively westward. In the western part of the field, this pattern persists, except along the main axis of the KEC, where phase propagation was eastward. The direction of phase propagation north and south of the KEC seems to assume a larger poleward component to the north and to the south respectively, than in the eastern half of the field, where phase propagates almost due west.

7. Summary and conclusions

The distributions of energy, time scales, length scales and phase propagation in the mid-latitude eastern North Pacific are substantially different from those in the western half of the basin. In the eastern North Pacific, the energy of the internal temperature fluctuations is very low and its distribution is fairly uniform. Time scales and meridional length scales are distributed over broad ranges, zonal length scales are relatively small, and the direction of phase propagation is almost due west. At the eastern boundary, time scales and meridional length scales are small but zonal length scales are distributed over a broad range. In contrast, the energy of the internal temperature fluctuations in the western North Pacific is high, particularly along the main axis of the KEC. The energy along the main axis decreases toward the east. It

also decreases towards the north or south, with length scales of decay of about 1000 km. Time scales are smaller near the western boundary than in the interior and increaseeastward. Both zonal and meridional length scales are larger near the western boundary and become smaller towards the interior region. Phase propagation along the KEC appears to be eastward, while phase propagation in the outer regions north and south of the KEC seems to be westward with poleward components to the north and to the south, respectively.

Considering the comparatively low energy and uniform structure of the internal temperature fluctuations in the eastern North Pacific, one might speculate that they are atmospherically generated. The higher energy of the temperature fluctuations in the western North Pacific and the manner in which the structure coincides with the dominant current, the KEC, suggests that some kind of current instability (perhaps baroclinic) is operating there. Of course, atmospheric forcing would be operating in the west too, and this process might be of secondary importance, a "background" effect.

CHAPTER II.

LOCAL BAROCLINIC INSTABILITY OF NONZONAL CURRENTS

1. Introduction

There have been many studies (e.g., Orlanski and Cox, 1973; Holland and Lin, 1975) on local baroclinic instability (hereafter referred to as instability) of major currents like the KEC. Owing to those studies, it is now widely accepted that instibility is an obvious source of energetic temperature fluctuations in the regions along such currents. However, to our knowledege, no attempt has been made to apply the instability theory specifically to the KEC region, in order to explain the observed spatial and temporal characteristics of internal temperature fluctuations.

Some observations (e.g., Mizuno and White, 1983; Chapter I) suggested that the basic flow (hereafter referred to as flow) in the mid-latitude western North Pacific might be nonzonal. Hence, local instability of nonzonal flows may be more suitable for explaining the observed characteristics. There have been some studies on instability of nonzonal flows (e.g., Robinson and McWilliams, 1974; Pedlosky, 1979; Kang, Price and Magaard, 1982). The earlier studies on instability of nonzonal mean

flows suggested that waves grow faster in a nonzonal flow than in a zonal flow. Because of limited applicability of the earlier nonzonal instability studies to the KEC region an investigation specifically focused on the instability of a nonzonal flow (modeling the KEC as a nonzonal flow) is desirable.

The purpose of this chapter is to explore local instability of nonzonal flows in an attempt to explain the observed distributions of dominant time scales, length scales and phase propagation of internal temperature fluctuations in the mid-latitude western North Pacific. In this study, we will see how wave period, phase speed, growth period, and longest possible wavelength of unstable waves depend on vertical shear, flow orientation, wave direction, and stratification, with the main interest in application to the KEC region. The results will be discussed in terms of critical shear, and effect of changing vertical shear, stratification, and flow orientation and wave direction on instability.

2. Formulation

The quasi-geostrophic vorticity equation for a two-layer model in the absence of bottom topography and friction (cf, Pedlosky, 1979) is

$$\left(\frac{\partial}{\partial t}+\frac{\partial\tilde{\psi}_n}{\partial x}\frac{\partial}{\partial y}-\frac{\partial\tilde{\psi}_n}{\partial y}\frac{\partial}{\partial x}\right)\left[\nabla_H^2\tilde{\psi}_n-(-1)^n\frac{1}{R_n^2}(\tilde{\psi}_2-\tilde{\psi}_1)+\beta y\right]=0, \quad n=1,2 \qquad (2\text{-}1)$$

where Ψ_n is the total geostrophic stream function. Rn ($=(g\frac{\Delta\rho}{\rho}D_n)^{\frac{1}{2}}/f_0$) is the Rossby radius of deformation (hereafter referred to as Rossby radius) at n_{th} layer (n=1 for the upper layer, and n=2 for the lower layer). β is the meridional gradient of the Coriolis parameter. Equation (2-1) is a dimensional form of Pedlosky's equation (6-5-21) (Pedlosky, 1979). The numerical value of β used in this dissertation is 1.9×10^{-11} sec^{-1} m^{-1}, its value at $35^{o}N$, the reference latitude of the KEC. The solution of the potential vorticity equation consists of a basic state $\psi_n(x,y)$ and a perturbed state $\phi_n(x,y,t)$,

$$\tilde{\psi}_n(x,y,t) = \psi_n(x,y) + \phi_n(x,y,t) \qquad (2\text{-}2)$$

The function ϕ_n represents the structure of the evolving perturbation field. Substituting (2-2) in (2-1), one obtains a linearized form of the potential vorticity equation.

$$\left(\frac{\partial}{\partial t}+\frac{\partial\psi_n}{\partial x}\frac{\partial}{\partial y}-\frac{\partial\psi_n}{\partial y}\frac{\partial}{\partial x}\right)q_n+\frac{\partial\phi_n}{\partial x}\frac{\partial\pi_n}{\partial y}-\frac{\partial\phi_n}{\partial y}\frac{\partial\pi_n}{\partial x}=0, \quad n=1,2 \qquad (2\text{-}3)$$

where $q_n=\nabla_H^2\phi_n-(-1)^n\frac{1}{R_n^2}(\phi_2-\phi_1)$

$\pi_n=\nabla_H^2\psi_n-(-1)^n\frac{1}{R_n^2}(\psi_2-\psi_1)+\beta y$

The basic state is characterized by

$$U_n=-\frac{\partial\psi_n}{\partial y}=\text{const.}, \qquad V_n=\frac{\partial\psi_n}{\partial x}=\text{Const.} \qquad (2\text{-}4)$$

In this dissertation, it is assumed that the basic flow is somehow maintained by some forcings in both layers. Equation (2-3) may then be rewritten as

$$\left(\frac{\partial}{\partial t}+U_n\frac{\partial}{\partial x}+V_n\frac{\partial}{\partial y}\right)\left[\nabla_H^2\phi_n+(-1)^n\frac{1}{R_n^2}(\phi_1-\phi_2)\right]$$

$$+\frac{\partial\phi_n}{\partial x}\left[\beta+(-1)^n\frac{1}{R_n^2}(U_2-U_1)\right]+(-1)^n\frac{\partial\phi_n}{\partial y}\left[\frac{1}{R_n^2}(V_2-V_1)\right]=0,\ n=1,2 \qquad (2\text{-}5)$$

We assume a plane wave solution of a form

$$\phi_n=A_n e^{i(kx+\ell y-\omega t)} \qquad (2\text{-}6)$$

Substituting (2-6) in (2-5) and equating the amplitude ratio A_2/A_1 obtained from both layers, we obtain

$$\omega=\vec{K}\cdot\vec{U}_2+\frac{(\vec{K}\cdot\vec{U}_S)K^2(K^2+\frac{2}{R_S^2})-k\beta(2K^2+\frac{1}{R_1^2}+\frac{1}{R_2^2})}{2K^2(K^2+\frac{1}{R_1^2}+\frac{1}{R_2^2})}\pm\Big[k^2\beta^2(\frac{1}{R_1^2}+\frac{1}{R_2^2})^2 \qquad (2\text{-}7)$$

$$+2k\beta(\vec{K}\cdot\vec{U}_S)K^4(\frac{1}{R_1^2}-\frac{1}{R_2^2})+(\vec{K}\cdot\vec{U}_S)^2K^4(K^4-\frac{4}{R_1^2R_2^2})\Big]^{\frac{1}{2}}/2K^2(K^2+\frac{1}{R_1^2}+\frac{1}{R_2^2})$$

where $\vec{K}=ki+lj$, $\vec{U}_S=\vec{U}_1-\vec{U}_2$ and $\vec{U}_n=u_ni+v_nj$, n=1,2. In this two-layer system, the upper and lower layers are coupled through the so-called vertical stretching term.

If there is no mean flow, (2-7) reduces to the two-layer form of the dispersion relations of baroclinic and barotropic Rossby waves,

$\omega=\frac{-k\beta}{K^2+\frac{1}{R_1^2}+\frac{1}{R_2^2}}$ and $\omega=\frac{-k\beta}{K^2}$,

respectively. If there exist only zonal flows (i.e., $v_1=v_2=0$), (2-7) assumes the form of Pedlosky's equation (7-11-6) for ω (Pedlosky, 1979).

In order to more easily examine the general case of non-zonal, non-meridional directions of flow and wave propagation, the velocity vector of the mean flow is converted into a flow speed and orientation, and similarly, the wavenumber vector is converted into a wavenumber and wave direction. That is,

$$\vec{U}=u\hat{\imath}+v\hat{\jmath}=\tilde{U}\cos\theta\hat{\imath}+\tilde{U}\sin\theta\hat{\jmath} \qquad (2\text{-}8a)$$

$$\vec{K}=k\hat{\imath}+l\hat{\jmath}=K\cos\Phi\hat{\imath}+K\sin\Phi\hat{\jmath} \qquad (2\text{-}8b)$$

where $\tilde{U}$ and K are the flow speed and wavenumber, respectively. Θ and Φ are the flow orientation and wave direction, respectively. Θ is assumed to be the same in both layers. The convention for Θ and Φ is as described in Chapter I, 0^o is due east, 90^o is due north, etc.. One can write (2-7), using (2-8), as

$$\omega = K\tilde{U}_2\cos(\Phi-\theta)+\{K\tilde{U}_S\cos(\Phi-\theta)K^2(K^2+\tfrac{2}{R_2^2})-K\beta\cos\Phi(2K^2+\tfrac{1}{R_1^2}+\tfrac{1}{R_2^2})$$
$$\pm[K^2\beta^2\cos^2\Phi(\tfrac{1}{R_1^2}+\tfrac{1}{R_2^2})^2+2K^6\beta\tilde{U}_S(\tfrac{1}{R_1^2}-\tfrac{1}{R_2^2})\cos\Phi\cos(\Phi-\theta)$$
$$+K^6\tilde{U}_S^2(K^4-\tfrac{4}{R_1^2R_2^2})\cos^2(\Phi-\theta)]^{\frac{1}{2}}\}/2K^2(K^2+\tfrac{1}{R_1^2}+\tfrac{1}{R_2^2}) \qquad (2\text{-}9)$$

where ω is now a function of K, Θ and Φ for a given flow condition of $\tilde{U}_1$, $\tilde{U}_2$, R_1 and R_2.

An instability occurs when the quantity under the square root is negative. One can find a critical shear, $\tilde{U}_{SC}$, by solving the quantity under the square root for $\tilde{U}_S$,

$$\tilde{U}_{SC}=\frac{K^2\beta(\frac{1}{R_1^2}-\frac{1}{R_2^2})\cos\Phi+\{\beta^2\frac{4}{R_1^2R_2^2}[(\frac{1}{R_1^2}+\frac{1}{R_2^2})^2-K^4]\cos^2\Phi\}^{\frac{1}{2}}}{K^2(\frac{4}{R_1^2R_2^2}-K^4)\cos(\Phi-\theta)} \qquad (2\text{-}10)$$

The flow will be unstable if $\tilde{U}_S>\tilde{U}_{SC}$. Since $\tilde{U}_{SC}$ must be real, it is required that $(\frac{1}{R_1^2}+\frac{1}{R_2^2})^2>K^4$. This condition eliminates waves of wavelengths shorter than about 100 km for any realistic stratification. Since R_n is defined as $(g\frac{\Delta\rho}{\rho}D_n)^{\frac{1}{2}}/f_o$, $(\frac{1}{R_1^2}+\frac{1}{R_2^2})^2>K^4$ for most cases of oceanic stratification. For long waves with wavelengths longer than $4.4R_1$, we have $\frac{4}{R_1^2R_2^2}-K^4>0$, since R_1R_2 is largest

when $R_1=R_2$. For scales of motion with which we are concerned, it seems reasonable to assume that $\frac{4}{R_1^2 R_2^2}-K^4>0$. If we restrict ourselves to the case of $|\phi-\theta|<90$ (i.e., $\cos(\phi-\theta)>0$), (2-10) is the only solution for the critical shear.

3. Results

An application of the model was made using combinations of a few representative values of oceanic shear and Rossby radii. (The influence of stratification on instability can be investigated using different Rossby radii.) The current profile at 152°E produced by Schmitz (1984) provided one pair of mean velocities (shear I in Table 2.1). Two other pairs were obtained by assuming that the upper layer speeds were propotional to the horizontal temperature gradients at 300 m. The temperature gradients in our data at 165°E and in the California Current region gave us the upper layer geostrophic speeds of 15 cm/sec and 7 cm/sec respectively. The corresponding lower layer speeds for these two cases werw guesses. The choice of Rossby radii for our two-layer system was obtained from Rossby radii of a continuous water column (denoted by R) using the relation of $\frac{1}{R^2}=\frac{1}{R_1^2}+\frac{1}{R_2^2}$ and approximate depth ratios between the upper and lower layers (D_1/D_2). Pairs of upper and lower layer radii and the corresponding

Rossby radii of a continuous water column are presented in Table 2.1. The value of R in radii I is a lower limit and that in radii IV is an upper limit of the Rossby radius in the mid-latitude western North Pacific (Emery et al, 1984). The value of R in radii III is the smallest and was chosen arbitrarily.

a. Cirtical shear

The critical shear $\tilde{U}_{sc}$ is given as a function of the Rossby radii, wavenumber, flow orientation, and wave direction. The critical shear is smaller for a less stably stratified ocean than for a more stably stratified ocean at a given wavelength. A stable stratification exists whenever a large $\Delta\rho/\rho$ or a small D_1/D_2 is present. The smaller the critical shear, the more likely the encountering of an unstable flow. Table 2.2 shows the critical shear as a function of Rossby radii and wavelength for a 30^o flow orientation and a 30^o wave propagation direction (hereafter referred to as a 30^o flow and wave). In these cases $\Delta\rho/\rho$ is kept constant and the depth ratio is varied to alter the stability of the stratification, represented in the table as the ratio of the Rossby radii. For a given pair of Rossby radii, flow orientation, and wave direction, shorter wavelengths concur with smaller critical shears. This indicates that a flow

Table 2.1 List of three vertical shears and five pairs of Rossby radii to be used for case study.

	U_1[cm/sec]	U_2[cm/sec]	Region of approx.
shear I	30	3	152°E
shear II	15	1	165°E
shear III	7	1	California Current

	R_1[km]	R_2[km]	R[km]	D_1/D_2
radii I	30	52	26	1/3
radii II	41	41	29	1/1
radii III	20	62	19	1/9
radii IV	49	69	40	1/2
radii V	56	56	40	1/1

Table 2.2 Critical shears [cm/sec] as a function of Rossby radii and wavelengths for a 30° flow and wave.

$R_1;R_2$[km] (Radii) / Wave-length[km]	30;52 I	41;41 II	20;62 III
300	5.8	4.2	8.2
500	12.5	10.8	19
700	24	20.8	35
900	38	35	60

with small vertical shear can be potentially unstable to a short wave but may not be unstable to a longer wave.

The critical shear also depends on wave direction. Figs. 2.1a and b show the critical shear as a function of wave direction and wavelength for two given flow orientations and one pair of Rossby radii (R_1/R_2). An eastward wave has a larger critical shear than waves of any other directions including a westward wave. This indicates that a flow is potentially less unstable to an eastward wave than to waves of any other direction. When both layers have the same depth, the critical shear is the same for both strictly westward and strictly eastward waves. For a 30^o flow, the critical shear decreases gradually at short wavelengths and rapidly at long wavelengths as the wave direction changes from zonal to meridional. This indicates that the effect of changing wave direction on critical shear is greater for a longer wave than for a shorter wave. For a 90^o flow and wave, the critical shear is zero; the flow can be unstable at any speed. At short wavelengths the critical shear decreases more rapidly with a 90^o flow than with a 30^o flow as the wave direction changes from zonal to meridional.

For a given vertical shear $\tilde{U}_s$ and flow orientation, the longest possible wavelength at which a wave may become unstable increases as the wave direction approaches 90^o. For a 30^o flow and wave, the longest possible wavelengths

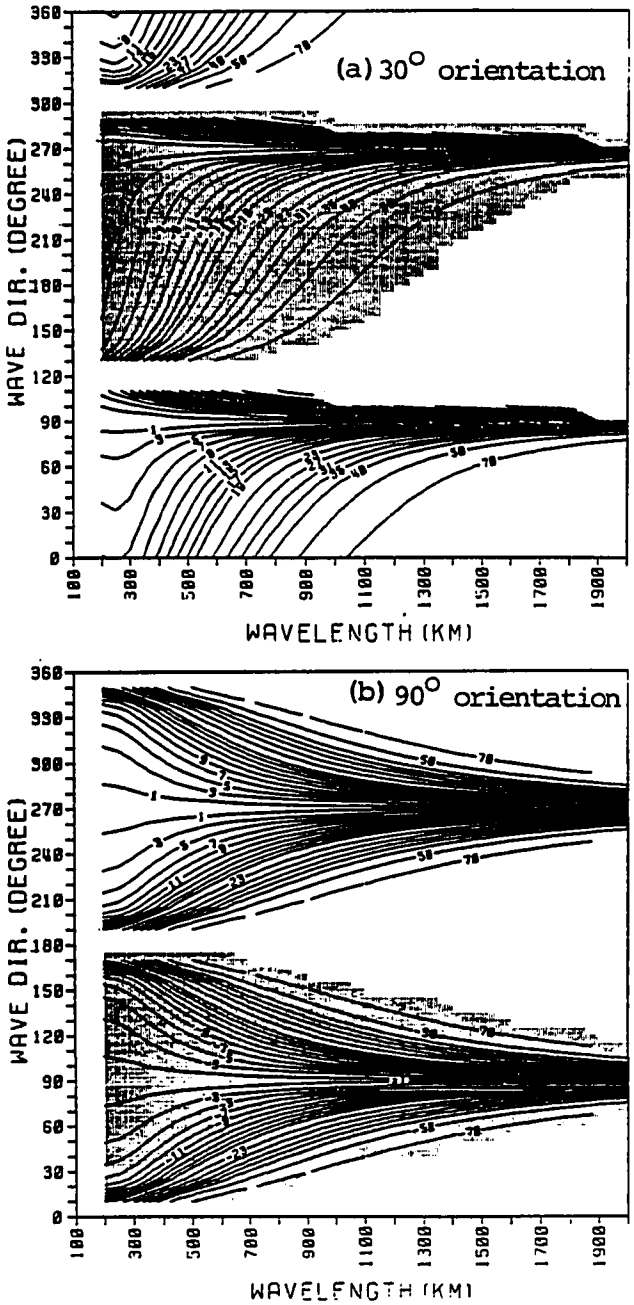

Figure 2.1 Critical shear [cm/sec] as a function of wavelengths and wave directions for radii I and flow orientations of (a) 30° and (b) 90°. (There is a $\pm 180^{\circ}$ redundancy, i.e., 30° gives the same result at 210°)

are 800, 540, and 350 km for given critical shears of 32, 15, and 7 cm/sec, respectively. Hence, waves with wavelengths longer than these will always be stable in such a regime. For realistic Rossby radii, waves shorter than 700, 500, and 300 km may be unstable along the axis of the KEC, near 152°E, 165°E, and 173°W, respectively.

b. Effect of changing vertical shear on instability

The effect of changing vertical shear on instability is such that for a given pair of Rossby radii, flow orientation and wave direction, strengthening the vertical shear shortens the wave period and growth period ($2\pi/\omega_i$) of unstable waves at each wavelength (Tables 2.3 and 2.4). The phase speed, under the same conditions, increases with vertical shear (Table 2.5). The longest possible wavelengths at which a wave may become unstable also increases with increasing vertical shear (Table 2.3). Considering that the observed dominant wavelength in subarea II (Chapter I) was in the range of 600-800 km, becoming smaller towards the interior, the range of the longest possible wavelengths and the decrease in wavelength with decreasing vertical shear agree well with the observations. The corresponding periods, phase speeds, and growth periods are also in agreement with the observed ranges.

Table 2.3 Wave periods [months] of unstable waves at selected wavelengths, vertical shears, flow orientations and wave directions for radii I. Also shown is the longest possible wavelengths of the unstable waves.

$U_1;U_2;$	Wavelength [km] / Wave dir.	1300	1100	900	700	500	300	Longest possible wavelength [km]
30;3;30°	330						3.5	470
	0					8.0	1.6	580
	30					4.1	1.3	670
	60				10.6	3.4	1.4	830
	90	10.2	8.6	7.0	5.4	3.7	2.1	>2000
15;1;30°	330						33.6	320
	0						6.0	390
	30						3.9	450
	60					21.7	3.6	500
	90	22.0	18.6	15.1	11.6	8.0	4.4	>2000
7;1;270°	210							260
	240						3.1	430
	270	19.9	16.8	13.6	10.5	7.3	4.1	>2000
	300						10.2	400
	330							

Table 2.4 Growth periods $2\pi/\omega_i$ [months] of unstable waves at selected wavelengths, vertical shears, flow orientations and wave directions for radii I.

$U_1;U_2;$	Wavelength [km] / Wave dir.	1300	1100	900	700	500	300
30;3;30°	330						3.1
	0					2.8	1.7
	30					2.1	1.4
	60				3.6	2.3	1.6
	90	8.7	7.4	6.1	4.9	3.7	2.7
15;1;30°	330						9.2
	0						3.8
	30						3.0
	60					5.3	3.3
	90	16.8	14.3	11.9	9.4	7.1	5.3
7;1;270°	210						
	240						7.4
	270	19.6	16.7	13.8	11.0	8.3	6.2
	300						9.6
	330						

Table 2.5 Phase speeds [cm/sec] of unstable waves at selected wavelengths, vertical shears, flow orientations and wave directions for radii I.

$U_1;U_2;$	Wavelength [km] / Wave dir.	1300	1100	900	700	500	300
30;3;30°	330						3.3
	0					2.4	7.1
	30					4.7	9.0
	60				2.5	5.7	8.4
	90	4.9	4.9	5.0	5.1	5.2	5.6
15;1;30°	330						0.3
	0						1.9
	30						3.0
	60					0.9	3.3
	90	2.3	2.3	2.3	2.3	2.4	2.7
7;1;270°	210						
	240						3.8
	270	2.5	2.5	2.6	2.6	2.6	2.8
	300						1.1
	330						

c. Effect of changing stratification on instability

Stratification influences the instability in such a way that the less stable the stratification is, the shorter the wave period and growth period become (Tables 2.6 and 2.7) while the phase speed becomes larger (Table 2.8). The longest possible wavelength at which a wave may become unstable is also longer for less stable stratification (Table 2.9). Hence, a flow may be unstable to a long wave if the ocean is weakly stratified.

Strong boundary currents such as the Kuroshio are typically deep, and therefore, in the two-layer approximation, their D_1/D_2 ratio is large. The KEC is strong in the west and decreases in strength eastward. If D_1/D_2 correspondingly decreases eastward, then the theory predicts longer length scales in the western part of the current than in the eastern part, as observed. However, since the zonal change in the Rossby radius (for a continuously stratified ocean) in the KEC region is small (Emery, et al., 1984), the effect of changing stratification would therefore be less important than the effect of changing vertical shear.

d. Effect of changing flow orientation and wave direction on instability

The longest possible wavelengths, wave periods, phase

Table 2.6 Wave periods [months] of unstable waves at selected wavelengths, Rossby radii and wave directions for shear I and a 30° flow.

$R_1;R_2$	Wavelength [km] / Wave dir.	1500	1300	1100	900	700	500	300
30;52	330							3.5
	0						8.0	1.6
	30						4.1	1.3
	60					10.6	3.4	1.4
	90	11.8	10.2	8.6	7.0	5.4	3.7	2.1
41;41	330						7.9	2.0
	0						2.6	1.0
	30					4.8	1.8	0.8
	60				8.4	3.4	1.8	0.9
	90	7.0	6.1	5.1	4.2	3.3	2.3	1.4
20;62	330							8.3
	0							3.2
	30						29.9	2.4
	60						9.0	2.4
	90	20.6	17.8	15.0	12.1	9.2	6.3	3.3
49;69	330						89.8	2.7
	0						4.8	1.3
	30					22.8	2.9	1.0
	60				130.7	6.3	2.5	1.1
	90	9.5	8.2	6.9	5.6	4.3	3.0	1.7
56;56	330						9.6	2.1
	0						2.7	1.0
	30					5.3	1.9	0.8
	60				9.0	3.5	1.8	0.9
	90	7.0	6.1	5.1	4.2	3.3	2.3	1.4

Table 2.7 Growth periods $2\pi/\omega_i$ [months] of unstable waves at selected wavelengths, Rossby radii and wave directions for shear I and a 30° flow.

$R_1;R_2$	Wavelength [km] / Wave dir.	1500	1300	1100	900	700	500	300
30;52	330							3.1
	0						2.8	1.7
	30						2.1	1.4
	60					3.6	2.3	1.6
	90	10.2	8.7	7.4	6.1	4.9	3.7	2.7
41;41	330						5.2	2.7
	0						2.2	1.5
	30					3.3	1.8	1.3
	60				5.6	2.9	2.0	1.5
	90	8.7	7.6	6.5	5.4	4.3	3.3	2.5
20;62	330							4.9
	0							2.4
	30						3.9	1.9
	60						3.5	2.2
	90	14.8	12.8	10.9	9.0	7.1	5.2	3.5
49;69	330						11.1	6.6
	0						3.0	3.2
	30					4.6	2.3	2.6
	60				8.3	3.4	2.4	2.9
	90	9.3	8.2	7.0	5.9	4.8	3.9	4.6
56;56	330						6.1	4.3
	0						2.5	2.4
	30					3.5	2.0	2.0
	60				5.8	3.0	2.2	2.3
	90	8.8	7.7	6.6	5.6	4.5	3.7	4.0

Table 2.8 Phase speeds [cm/sec] of unstable waves at selected wavelengths, Rossby radii and wave directions for shear I and a 30° flow.

$R_1;R_2$	Wavelength [km] / Wave dir.	1500	1300	1100	900	700	500	300
30;52	330							3.5
	0						2.4	7.1
	30						4.7	9.0
	60					2.5	5.7	8.4
	90	4.9	4.9	4.9	5.0	5.1	5.2	5.6
41;41	330						2.4	5.9
	0						7.6	11.5
	30					5.6	10.7	14.1
	60				4.2	8.0	10.9	12.9
	90	8.3	8.3	8.3	8.3	8.3	8.3	8.3
20;62	330							1.4
	0							3.6
	30						0.7	4.9
	60						2.1	4.9
	90	2.8	2.8	2.8	2.9	2.9	3.1	3.5
49;69	330						0.2	4.3
	0						4.0	9.0
	30					1.2	6.7	11.2
	60				0.3	4.3	7.6	10.5
	90	6.1	6.1	6.1	6.2	6.3	6.5	6.9
56;56	330						2.0	5.6
	0						7.1	11.2
	30					5.1	10.3	13.9
	60				3.9	7.7	10.7	12.8
	90	8.3	8.3	8.3	8.3	8.3	8.3	8.3

Table 2.9 Longest possible wavelengths [km] of unstable waves as a function of Rossby radii and wave directions for shear I and a 30° flow.

$R_1;R_2$ [km] (radii) / Wave dir.	30;52 I	41;41 II	20;62 III	49;69 IV	56;56 V
330	470	560	370	500	560
0	580	690	450	630	690
30	670	800	520	730	800
60	830	980	640	910	980
90	>2000	>2000	>2000	>2000	>2000

speeds, and growth periods of unstable waves change substantially with changing flow orientation and wave direction for a given pair of Rossby radii and vertical shear. Table 2.10 and Fig. 2.2 show that for a zonal flow the waves are unstable if the wavelengths are shorter than about 600 km (the longest possible wavelength is about 600 km for an eastward flow and wave, and only slightly longer than 600 km for a westward flow and wave). In contrast, for a nonzonal flow the longest possible wavelength of unstable waves increases as the flow orientation approaches 90^{o}.

The effect of changing flow orientation on period is to decrease wave period at each wavelength as the flow orientation changes from eastward to westward (Table 2.11 and Fig. 2.2). This is true as long as the angle between the flow orientation and wave direction is not too large (in most cases less than 60^{o}). The effect of changing wave direction on period is different between the zonal and nonzonal flow cases. For a zonal flow the wave period is shortest at all wavelengths when the flow and the wave travel in the same direction (Fig. 2.2a). For a nonzonal flow, however, the wave periods of unstable waves are shortest when the flow orientation is at some angle to the direction of wave propagation at wavelengths longer than 300 km. The wave direction at which the shortest possible

Table 2.10 Longest possible wavelengths [km] of unstable waves as a function of flow orientations and wave directions for shear I and radii I.

Wave dir. \ Flow ori. (Θ)	0	180	30	60	90
Θ-60	630	700	470	440	470
Θ-30	630	700	580	630	830
Θ+0	630	700	670	890	>2000
Θ+30	630	700	830	>2000	920
Θ+60	630	700	>2000	700	540

Table 2.11 Wave periods [months] of unstable waves at selected wavelengths, flow orientations and wave directions for shear I and radii I.

Flow ori. \ Wavelength [km] / Wave dir.	1700	1500	1300	1100	900	700	500	300
0								
300							10.2	2.7
330							5.9	1.6
0							5.1	1.3
30							5.9	1.6
60							10.2	2.7
180								
120						2.4	2.3	1.7
150						1.4	1.3	1.0
180						1.2	1.1	0.8
210						1.4	1.3	1.0
240						2.4	2.3	1.7
30								
330								3.5
0							8.0	1.6
30							4.1	1.3
60						10.6	3.4	1.4
90	13.4	11.8	10.2	8.6	7.0	5.4	3.7	2.1
60								
0								3.9
30							5.9	1.6
60						6.9	2.7	1.2
90	7.7	6.8	5.9	5.0	4.0	3.1	2.1	1.2
120						2.4	2.3	1.7
90								
30								3.5
60						10.6	3.4	1.4
90	6.7	5.9	5.1	4.3	3.5	2.7	1.9	1.0
120					1.9	1.8	1.6	1.0
150							1.8	1.5

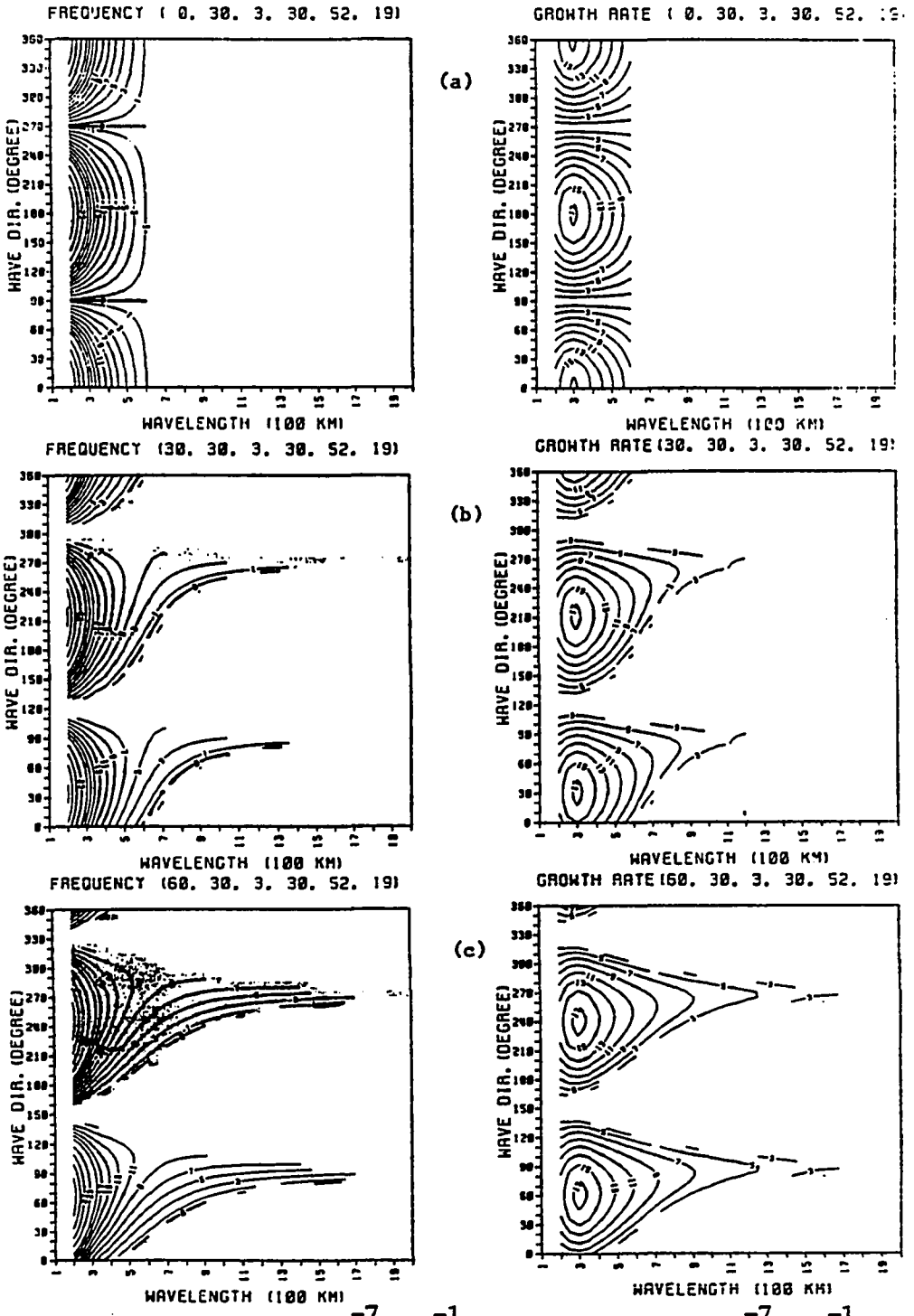

Figure 2.2 Frequency [10^{-7} sec^{-1}] and growth rate [10^{-7} sec^{-1}] as a function of wavelengths and wave directions at given flow orientations of (a) 0^{o}, (b) 30^{o}, and 60^{o}.

wave period occurs approaches 90^{o} as the wavelength becomes longer.

One can infer the effect on phase speed of changing flow orientation and wave direction from their effect on period. In general, the phase speeds are larger when the flow orientation and wave direction have a westward component. In Table 2.12, one may also notice that the phase speed of waves propagating with the westward component increases with increasing wavelength.

The growth period generally decreases as the flow orientation changes from eastward to meridional and also from meridional to westward at each wavelength of less than 700 km (Table 2.13 and Fig. 2.2). The effect of changing wave direction on growth period for various flow orientations is such that the growth periods are shortest when the basic flow and wave travel in the same direction at wavelengths shorter than 700 km. In a similar study, Robinson and McWilliams (1974) found that waves propagating parallel to the mean flow grow the fastest. As an example, Fig. 2.3b shows the growth rate for the case of shear I, radii I, and a wavelength of 400 km. However, for wavelengths of 700 km and longer, the fastest growth occurs when there is some angle between the flow orientation and the direction of wave propagation.

The equation for the growth rate (the terms under the square rootin equation 2-9) includes four terms; the first

Table 2.12 Phase speeds [cm/sec] of unstable waves at selected wavelengths, flow orientations and wave directions for shear I and radii I.

Flow ori.	Wavelength [km] / Wave dir.	1700	1500	1300	1100	900	700	500	300
0	300							1.9	4.3
	330							3.3	7.5
	0							3.8	8.6
	30							3.3	7.5
	60							1.9	4.3
180	120						11.3	8.5	7.0
	150						19.5	14.7	12.1
	180						22.5	17.0	14.0
	210						19.5	14.7	12.1
	240						11.3	8.5	7.0
30	330								3.3
	0							2.4	7.1
	30							4.7	9.0
	60						2.5	5.7	8.4
	90	4.9	4.9	4.9	4.9	5.0	5.1	5.2	5.6
60	0								3.0
	30							3.3	7.5
	60						3.9	7.1	10.0
	90	8.5	8.5	8.5	8.6	8.6	8.7	9.0	9.8
	120						11.3	8.5	7.0
90	30								3.3
	60						2.5	5.7	8.4
	90	9.8	9.8	9.9	9.9	10.0	10.1	10.4	11.3
	120					18.7	14.9	12.3	11.1
	150							10.9	8.0

Table 2.13 Growth periods $2\pi/\omega_i$ [months] of unstable waves at selected wavelengths, flow orientations and wave directions for shear I and radii I.

Flow ori. \ Wavelength [km] / Wave dir.	1700	1500	1300	1100	900	700	500	300
0	300						4.5	2.9
	330						2.6	1.7
	0						2.3	1.5
	30						2.6	1.7
	60						4.5	2.9
180	120					23.9	4.1	2.7
	150					13.8	2.4	1.6
	180					11.9	2.1	1.3
	210					13.8	2.4	1.6
	240					23.9	4.1	2.7
30	330							3.1
	0						2.8	1.7
	30						2.1	1.4
	60					3.6	2.3	1.6
	90	11.3	10.2	8.7	7.4	6.1	4.9	3.7	2.7
60	0							3.3
	30						2.6	1.7
	60					2.9	1.9	1.4
	90	6.5	5.8	5.0	4.3	3.6	2.8	2.1	1.6
	120						23.9	4.1	2.7
90	30							12.9	3.1
	60					19.0	3.6	2.3	1.6
	90	5.7	5.0	4.4	3.7	3.1	2.4	1.8	1.4
	120					10.8	3.0	2.2	1.6
	150							6.7	2.7

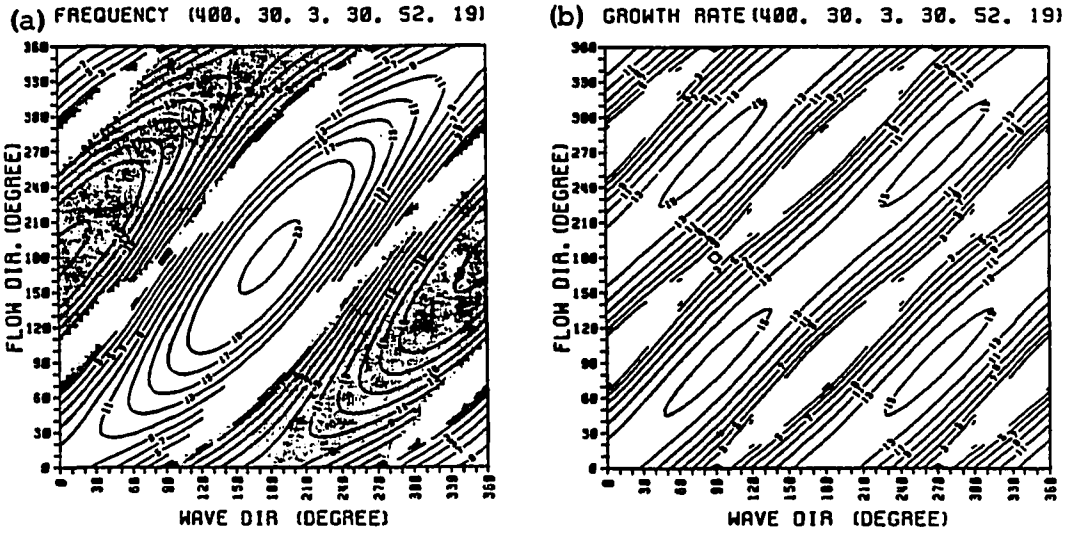

Figure 2.3 Frequency [10^{-7} sec^{-1}] and growth rate [10^{-7} sec^{-1}] as a function of flow orientations and wave directions for the case of shear I, radii I, and a wavelength of 400 km.

term is a function of the beta (β), the second term is a function of the beta and vertical shear, and the third and the fourth terms are functions of vertical shear. The second and the third terms only affect the growth rate change slightly. The second term will vanish if $R_1=R_2$. For the case of $R_1=R_2$, the growth rate for the westward flow is slightly higher than for the eastward flow because of this term. In general, the first and the fourth terms dominate in the growth rate. For a zonal flow and wave, $\cos(\Phi-\Theta)$ in the fourth term is largest but also $\cos\Phi$ in the first term is largest. Since the two terms differ in sign, the growth rate is therefore relatively small. However, for a nonzonal flow and wave traveling in the same direction, $\cos(\Phi-\Theta)$ is still large but $\cos\Phi$ becomes small, leaving a higher growth rate than for a zonal case. The physical explanation is that for a zonal flow and wave the particle motions enhance an instability but, since the particle motions are in the meridional direction, the beta-effect stablizes it. However, for a meridional flow and wave, the particle motions are zonal. Hence the particle does not feel the beta-effect, and there is no beta-stabilization. For a meridional flow and a zonal wave, the particle motion and flow are in the same direction, and there is no growth of waves. For a zonal flow and a meridional wave, no wave exists, since $\omega=0$.

An important effect of changing flow orientation and

wave direction on instability is to increase the size of the longest possible wavelength of unstable waves as flow and direction vary from zonal to meridional (600, 700, and 850 km for a 0^{o}, 30^{o}, and 60^{o} flow, respectively). Since the observed wavelengths appear to be predominantly longer than 600 km near the western boundary, and since the ranges of wave periods, phase speeds, and growth periods overlap the observed ranges in the nonzonal case, an instability mechanism based on a nonzonal basic flow apparently better explain the observed internal temperature fluctuations.

4. Summary and conclusions

The critical shear changes with changing stratification, wavelength, flow orientation, and wave direction. It is smaller for less stable stratification and for shorter wavelengths. The effect of flow orientation and wave direction is such that the critical shear is smallest when the flow and wave travel in the same direction. The critical shear is zero for a meridional flow and wave (Pedlosky, 1979), and increases as both the flow orientation and wave propagation approach a zonal direction. For a zonal flow and wave, the critical shear is smaller when both flow and wave travel westward than eastward. A 30^{o} flow and wave (an approximate

orientation of the KEC) produces critical shear values of 32, 15 and 7 cm/sec at wavelengths of 800, 540 and 350 km, respectively.

The effects on instability of an increase in vertical shear is to decrease the wave period and to increase the growth rate at each wavelength (for fixed stratification, flow orientation and wave direction), and to substantially increase the longest possible wavelength of unstable waves (e.g., from 500 km for shear II to 680 km for shear I both with radii IV, and a 30^{o} flow and wave). The magnitude of vertical shear is therefore an important parameter in determining instability.

The effect of increasing stability of stratification on instability is to stabilize the flow, and therefore there are less chances of a flow becoming unstable. Wave periods are longer and waves grow more slowly for more stable stratification if the vertical shear, flow orientation and wave direction are fixed. The accompaning phase speeds decrease with increasing stratification. The longest possible wavelengths of unstable waves increase for less stable stratification (e.g., 590, 680, and 770 km for radii III, I, and II, respectively). Hence, a flow in a weakly stratified ocean may become unstable to a fairly long wave. Changes in stratification, however, have less effect on instability than changes in vertical shear.

Flow orientation affects instability by increasing

the longest possible wavelengths and growth rates as the flow orientation changes from zonal to meridional. In the case of zonal flow, the longest possible wavelength is slightly longer and a wave grows slightly faster when the flow is westward rather than eastward. In general, the wave period decreases (the phase speed increases) as the flow orientation changes from eastward to westward.

The effect of changing wave direction on the longest possible wavelength, growth period, wave period, and phase speed is different for zonal and nonzonal flows. Waves grow faster, wave periods are shorter, and phase speeds are larger for a zonal flow, when the flow and wave travel in the same direction. However, the size of the longest possible wavelength varies little among different wave directions. For a nonzonal flow, the longest possible wavelength, growth period, wave period, and phase speed change substantially with changing wave direction. For any nonzonal flow orientation, the longest possible wavelength occurs at the 90^{o} wave direction. Waves grow the fastest when the flow and wave travel in the same direction, for wavelengths up to slightly less than 700 km. However, for wavelengths of 700 km and longer, the wave direction at which waves grow the fastest approaches 90^{o} as the wavelength increases. Similarly, for wavelengths longer than 300 km, the direction of the wave propagation at which the shortest wave period and the highest phase speed occur

approaches 90^{o} as the wavelength increases.

The analyses of the temperature data in Chapter I suggested that the time scale becomes larger and the length scale becomes smaller as one proceeds from the western boundary towards the interior region in the mid-latitude western North Pacific. This observed regional tendency of space and time scales can be explained by an instability analysis of a 30^{o} model flow in which the critical shear increases with increasing wavelength and also a stronger vertical shear accompanies a shorter period and a longer wavelength. The analyses also suggested dominant ranges of time scales, length scales and eastward phase speed. If the KEC is modeled as a zonal flow, the computed ranges of time scales, length scales and phase speed overlap the narrow portion of the observed dominant ranges. However, if the KEC is modeled as a nonzonal flow, the computed ranges agree better with the observed dominant ranges.

In conclusion, it is suggested here that the local baroclinic instability of mean shear flow with the southeastward and northeastward orientations is an important mechanism for the internal temperature fluctuations observed in the mid-latitude western North Pacific.

CHAPTER III

RADIATION OF ENERGY FROM A MESOSCALE DISTURBANCE TRAVELING ALONG A NONZONAL CURRENT

1. Introduction

In the vicinity of a strong current like the KEC, local instability is an obvious source of internal temperature fluctuations. However, the region of the strong current is confined to a rather narrow strip. In the region away from such a current, local instability (Gill et al., 1974; Robinson and McWilliams, 1974; Pedlosky, 1975) may not be a source, since the condition for instability is rarely met. Therefore, in the region away from strong currents, some other instability may be responsible for fairly energetic temperature fluctuations.

As a possible candidate for the source of the temperature fluctuations, Pedlosky (1977) suggested radiation of mechanical energy whose source is vigorous instability of strong currents like the Gulf Stream on the boundaries of the mid-ocean gyres. Pedlosky's result indicates that if the ocean itself south of the Gulf Stream is in eastward motion, such disturbances with positive phase speeds may radiate if the phase speed relative to the local current velocity is westward. In Pedlosky's study,

however, the basic flow and disturbance are restricted to the zonal direction.

In a preliminary instability analysis based upon a zonal flow, it was found that the results were not highly comparable with the observed dominant spatial and temporal characteristics. Since the basic flow might be nonzonal in the mid-latitude western North Pacific (Mizuno and White, 1983; Schmitz, 1984; Chapter I), it is interesting to see how the radiation characteristics change if the flow orientation is nonzonal.

The purpose of this chapter is to examine the radiation of energy to the cross-flow direction from a disturbance traveling along a nonzonal flow. In this study we will determine the length scale of decay for the periods and wavelengths within the observed dominant ranges. We will also determine any differences in radiation between zonal and nonzonal flows. The results will be discussed for the case of a zonal flow (also disturbance) and the case of a nonzonal flow (also disturbance), and effect of changing orientation of a flow (also disturbance) and stratification on radiation.

2. Formulation

The linearized potential vorticity equation (2-5), derived in Chapter II, can be converted into a more

convenient form for study in a nonzonal flow case using equation (2-8a), wherein the velocity vector are expressed in terms of a magnitude and direction. In order to obtain this new equation we substitute (2-8a) in (2-5), and then we rotate the Cartesian coordinate system in such a way that the new x-axis is along the flow and points in the direction of the flow, and the y-axis is in the cross-flow direction. A disturbance is assumed to travel in the same direction as background flow. This assumption is based on the results of Chapter II in which the growth rates are found to be high when both the flow and wave travel in the same direction for wavelengths up to about 700 km. The disturbance is also assumed to be periodic in the x-direction. In the rotated coordinate system, the potential vorticity equation is,

$$\left(\frac{\partial}{\partial t}+U_n\frac{\partial}{\partial x}\right)\left[\left(\frac{\partial^2}{\partial x^2}+\frac{\partial^2}{\partial y^2}\right)\phi_n-\frac{1}{R_n^2}(-1)^n(\phi_2-\phi_1)\right]$$
$$+\frac{\partial\phi_n}{\partial x}\left[\beta\cos\theta-\frac{1}{R_n^2}(-1)^n U_s\right]-\frac{\partial\phi_n}{\partial y}\beta\sin\theta=0,\quad n=1,2 \qquad (3\text{-}1)$$

where $U_s=U_1-U_2$. Following Pedlosky (1977), a radiation source is represented by the boundary condition at y=0,

$$\phi_n(x,\ y=0,t)=B_n e^{i(Kx-\omega t)} \qquad (3\text{-}2)$$

where K is real. An assumed solution which satisfies the boundary condition is

$$\phi_n=A_n e^{i(Kx-\omega t)+ily} \qquad (3\text{-}3)$$

where $\ell = \ell_r + i\,\ell_i$. In the region where $y>0$, ℓ_i must be non-negative so that ϕ_n is bounded as $y \to \infty$, and , similarly, the region where $y<0$, ℓ_i must be non-positive so that ϕ_n is bounded as $y \to -\infty$. Substituting (3-3) in (3-1), one obtains an expression for each layer that can be combined through the vertical stretching term. One obtains then a polynomial of the complex wavenumber in the cross-flow direction.

$$\ell^4 + A\ell^3 + B\ell^2 + C\ell + D = 0 \qquad (3\text{-}4)$$

where

$$A = \beta \sin\theta \left[\frac{1}{U_1 K - \omega} + \frac{1}{U_2 K - \omega} \right]$$

$$B = 2K^2 + \frac{1}{R_1^2} + \frac{1}{R_2^2} - \frac{(\beta\cos\theta + \frac{1}{R_1^2} U_s)K}{U_1 K - \omega} - \frac{(\beta\cos\theta - \frac{1}{R_2^2} U_s)K}{U_2 K - \omega} + \frac{\beta^2 \sin^2\theta}{(U_1 K - \omega)(U_2 K - \omega)}$$

$$C = \frac{\beta \sin\theta}{U_1 K - \omega}\left[K^2 + \frac{1}{R_2^2} - \frac{(\beta\cos\theta - \frac{1}{R_2^2} U_s)K}{U_2 K - \omega} \right] + \frac{\beta \sin\theta}{U_2 K - \omega}\left[K^2 + \frac{1}{R_1^2} - \frac{(\beta\cos\theta + \frac{1}{R_1^2} U_s)K}{U_1 K - \omega} \right]$$

$$D = K^4 + K^2\left[\frac{1}{R_1^2} + \frac{1}{R_2^2} - \frac{(\beta\cos\theta + \frac{1}{R_1^2} U_s)K}{U_1 K - \omega} - \frac{(\beta\cos\theta - \frac{1}{R_2^2} U_s)K}{U_2 K - \omega} \right] - \frac{\frac{1}{R_1^2}(\beta\cos\theta - \frac{1}{R_2^2} U_s)K}{U_2 K - \omega} - \frac{\frac{1}{R_2^2}(\beta\cos\theta + \frac{1}{R_1^2} U_s)K}{U_1 K - \omega} + \left[\frac{(\beta\cos\theta + \frac{1}{R_1^2} U_s)K}{U_1 K - \omega} \right]\left[\frac{(\beta\cos\theta - \frac{1}{R_2^2} U_s)K}{U_2 K - \omega} \right]$$

The amplitude ratios from the upper and lower layer expressions are respectively

$$\frac{A_2}{A_1} = -\frac{(U_1 K - \omega)(-K^2 - \ell^2 - \frac{1}{R_1^2}) + (\beta\cos\theta + \frac{1}{R_1^2} U_s)K - \beta \sin\theta\, \ell}{\frac{1}{R_1^2}(U_1 K - \omega)} \qquad (3\text{-}5)$$

$$\frac{A_2}{A_1} = \frac{\frac{1}{R_2^2}(U_2 K - \omega)}{(U_2 K - \omega)(-K^2 - \ell^2 + \frac{1}{R_2^2}) + (\beta\cos\theta - \frac{1}{R_2^2} U_s)K - \beta \sin\theta\, \ell} \qquad (3\text{-}6)$$

When there is no background mean flow (i.e., $U_1=U_2=0$), a dispersion relation for the baroclinic wave

$$\omega = \frac{-K\beta\cos\theta + \beta\sin\theta\, l}{K^2 + l^2 + \frac{1}{R_1^2} + \frac{1}{R_2^2}} \tag{3-7}$$

is obtained. Solving (3-7) for l,

$$l = \frac{1}{2}\left\{\frac{\beta\sin\theta}{\omega} \pm \left[\frac{\beta^2\sin^2\theta}{\omega^2} - 4\left(K^2 + \frac{\beta\cos\theta}{\omega} + \frac{1}{R_1^2} + \frac{1}{R_2^2}\right)\right]^{\frac{1}{2}}\right\} \tag{3-8}$$

If $\Theta=180^\circ$ (westward propagation),

$$l = \pm\frac{1}{2}\left[-4\left(K^2 - \frac{\beta K}{\omega} + \frac{1}{R_1^2} + \frac{1}{R_2^2}\right)\right]^{\frac{1}{2}} \tag{3-9}$$

In order to have radiation orthogonal to the direction of wave propagation, l must be real.

$$K^2 - \frac{\beta K}{\omega} + \frac{1}{R_1^2} + \frac{1}{R_2^2} \leq 0 \tag{3-10}$$

and therefore

$$\omega \geq \frac{\beta K}{K^2 + \frac{1}{R_1^2} + \frac{1}{R_2^2}} \tag{3-11}$$

If, on the other hand, $\Theta=0$ (eastward propagation),

$$l = \pm\frac{1}{2}\left[-4\left(K^2 + \frac{\beta K}{\omega} + \frac{1}{R_1^2} + \frac{1}{R_2^2}\right)\right]^{\frac{1}{2}} \tag{3-12}$$

Again requiring l to be real for radiation,

$$K^2 + \frac{\beta K}{\omega} + \frac{1}{R_1^2} + \frac{1}{R_2^2} \leq 0 \tag{3-13}$$

and therefore

$$\omega \leq \frac{-\beta K}{K^2 + \frac{1}{R_1^2} + \frac{1}{R_2^2}} \tag{3-14}$$

However, (3-14) can never be satisfied with positive β, K, and ω. Therefore there is no radiation in this case. Thus, in the absence of a mean flow, westward propagating disturbances will radiate orthogonal to the direction of wave propagation and can even be baroclinic Rossby waves. Disturbances propagating eastward in the absence of a mean current can neither radiate nor be baroclinic Rossby waves. This result was also found by Pedlosky (1977) in a study restricted to zonal flow. In fact, (3-4) reduces to

$$l^2 = \frac{1}{2}\left\{-2K^2 - \frac{1}{R_1^2} - \frac{1}{R_2^2} + \frac{(\beta + \frac{1}{R_1^2}U_s)K}{U_1K-\omega} + \frac{(\beta - \frac{1}{R_2^2}U_s)K}{U_2K-\omega}\right.$$
$$\pm\left\langle \left(\frac{1}{R_1^2} + \frac{1}{R_2^2}\right)^2 + \left[\frac{(\beta + \frac{1}{R_1^2}U_sK}{U_1K-\omega} - \frac{(\beta - \frac{1}{R_2^2}U_sK}{U_2K-\omega}\right]^2\right.$$
$$\left.\left. + 2\left(\frac{1}{R_1^2} - \frac{1}{R_2^2}\right)\left[\frac{(\beta - \frac{1}{R_2^2}U_s)K}{U_2K-\omega} - \frac{(\beta + \frac{1}{R_1^2}U_s)K}{U_1K-\omega}\right]\right\rangle^{\frac{1}{2}}\right\} \qquad (3\text{-}15)$$

for the case of $\Theta = 0^o$ and $U_1 \neq U_2 \neq 0$. Equation (3-15) is the dimensionalized equivalent of Pedlosky's equation (4.4) (Pedlosky, 1977).

It is interesting to note that the ratio of the amplitudes in the baroclinic, no mean current case is

$$\frac{A_2}{A_1} = \frac{R_1^2}{R_2^2},$$

a constant regardless of wavelength and orientation of a disturbance.

Equation (3-4) and (3-5) (or equivalently (3-6)) can now be used to study the general case of non-zonal current and non-zero current shear. Several cases have been

investigated. Table 3.1 lists the choices of upper and lower mean current speeds, Rossby radii, and layer depths. Radii I and II are based on the maximum Rossby radius (40 km) observed for continuous water columns in the mid-latitude western North Pacific (Emery et al, 1984). Radii III is based on the minimum Rossby radius (26 km) observed in the same area. The observed Rossby radii are converted to the two-layer analog by the procedure described in Chapter II. Solutions to the equations are obtained at increments of 20° orientation, one month period and 100 km wavelength.

3. Results

a. A case of a zonal flow and disturbance

In the case of a zonal background flow and disturbance (Fig. 3-1), the region where radiation occurs in period-wavelength space is generally small. The radiation region is smallest in the case where shear II was employed and largest when shear III was used. The shortest possible pairs of wavelength and period of a radiating disturbance are 300 km; 12 months, 400 km; 16 months, and 700 km; 15 months for shears I, II, and III, respectively. It is evident from a comparison with the observed time and length scales discussed in Chapter I that the radiation

Table 3.1 List of three background vertical shears and three pairs of Rossby radii to be used for case study.

	U_1[cm/sec]	U_2[cm/sec]
shear I	4	1
shear II	7	1
shear III	15	1

	R_1[km]	R_2[km]	R[km]	D_1/D_2
radii I	49	69	40	1/2
radii II	56	56	40	1/1
radii III	30	52	26	1/3

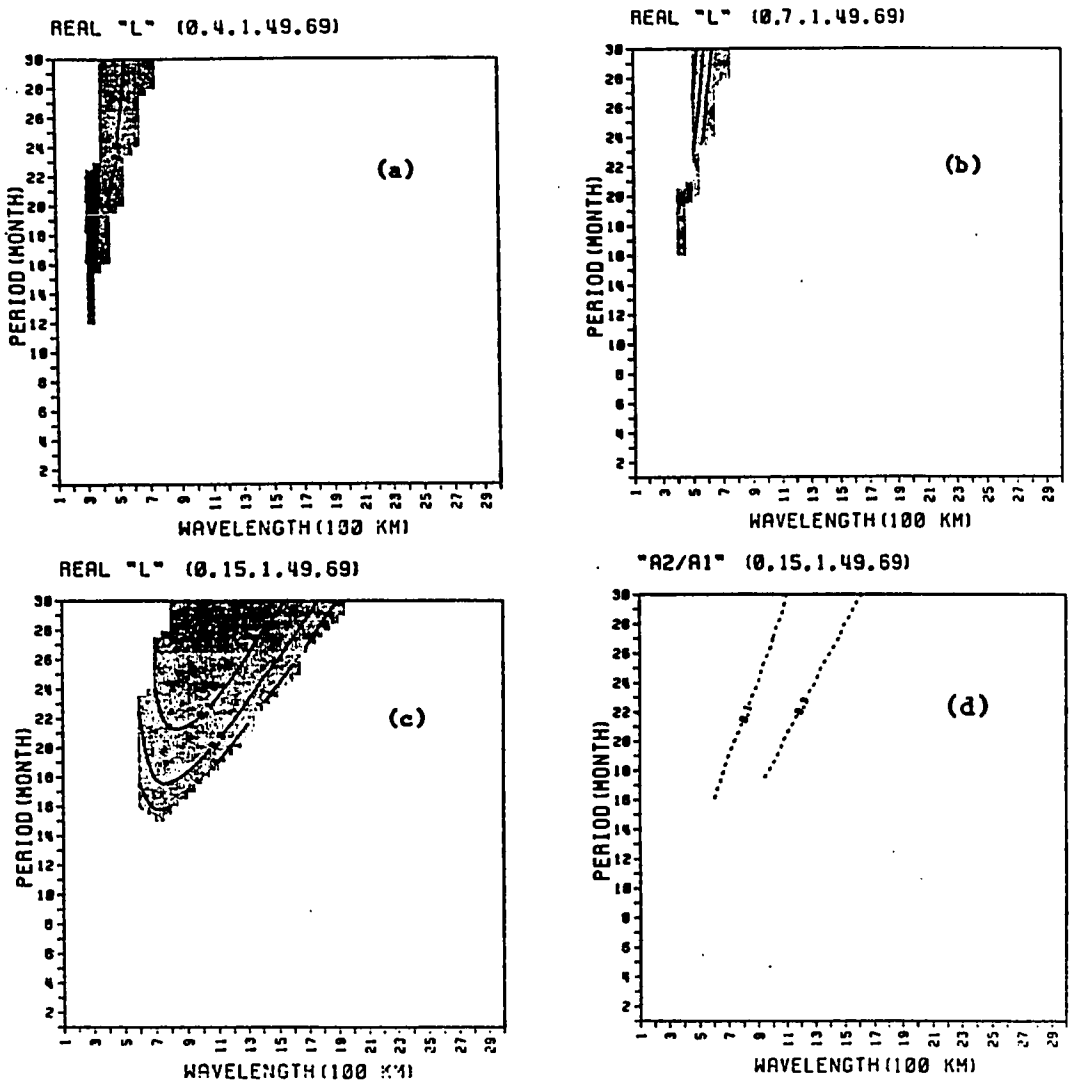

Figure 3.1 Real part of the cross-flow wavenumber for (a) shear I, (b) shear II, and (c) shear III in the case of an eastward flow and radii I. (d) Magnitude of amplitude ratio (A_2/A_1) in the case of shear III, radii I, and an eastward flow.

region in period-wavelength space does not overlap the observed dominant ranges of periods and wavelengths (<12 months; 600-800 km).

The ranges of the values of ℓ_r, which must be non-zero for radiation orthogonal to the disturbance and is hereafter referred to as the radiation wavenumber, are $0.53\text{-}2.15\text{x}10^{-7}$, $0.24\text{-}1.51\text{x}10^{-7}$, and $0.08\text{-}0.9\text{x}10^{-7}$ cm^{-1} for shears I, II, and III, respectively. This indicates that, at a given period and wavelength of a disturbance, the radiation wavenumber generally decreases with increasing vertical shear of the background flow. The radiation wavenumber determines the phase speed in the cross-flow direction (hereafter referred to as radiation phase speed). The radiation phase speed in this case increases with increasing background vertical shear. The radiation wavenumber and phase speed also vary with the phase speed of the disturbance. For shears I and II, and on the short wavelength side for shear III, the radiation phase speed (wavenumber) tends to increase (decrease) with increasing phase speed of the disturbance. A typical radiation phase speed is about 0.5 cm/sec at the shortest possible pairs of wavelength and period of a disturbance.

The ranges of the amplitude ratio (A_2/A_1) are 0.01-0.1, 0.01-0.15, and 0.0-0.46 for shears I, II, and III, respectively. In general, the amplitude ratio in the far-field at a given wavelength and period of a disturbance

increases with vertical shear. This indicates more penetration of radiated energy into the lower layer for stronger vertical shear. The amplitude ratios also show the tendency that the slower the disturbance travels, the greater is the radiated energy penetrating into the lower layer.

The amplitude ratio is determined by two terms, the relative vorticity and the planetary vorticity. For a weak background vertical shear (e.g., shear I), fixed wavelength, and increasing period of the disturbance, the relative vorticity term tends to increase the amplitude ratio, and the planetary vorticity term tends to decrease the ratio. For a strong background vertical shear (e.g., shear III), fixed wavelength, and increasing period of the disturbance, both the relative and planetary vorticity terms tend to increase the amplitude ratio in the far-field. As the wavelength of a disturbance increases at a fixed period, the opposite tendency of the above argument holds for both weak and strong vertical shear.

b. A case of a nonzonal flow and disturbance

We have seen that there is only a narrow region of pure baroclinic, surface-intensified ($A_2/A_1<1$) radiation in period-wavelength space for an eastward flow and disturbance. We have also seen that the wavelengths

and periods of a radiating disturbance are rarely within the observed dominant ranges. When the background flow and disturbance are nonzonal, the radiation region in period-wavelength space increases greatly. Furthermore, broad ranges of periods and wavelengths of a radiating disturbance are within the observed dominant ranges (Figs. 3.2-3.4).

For an exclusively nonzonal case, there are three different radiation regions in period-wavelength space. The three regions are a pure baroclinic, surface-intensified region (hereafter referred to as PBSI), a mixed baroclinic and barotropic region (hereafter, MBB) region, and a pure baroclinic, bottom-intensified region (hereafter, PBBI). The PBSI region closely resembles the radiation region of the zonal case. The MBB and the PBBI regions are very much different than the zonal case. A line along which the critical layer occurs generally demarks the boundary between the MBB and the PBBI regions. A critical layer is on where U_n-C=0, where n=1 or 2 and C is the phase speed of the disturbance. A pure baroclinicity is indicated whenever the phase of the amplitude ratio is 180^o. A surface-intensification is indicated by the magnitude of the amplitude ratio A_2/A_1 being smaller than 1, and a bottom-intensification by the magnitude being greater than 1.

Most of the observed dominant time and length scales

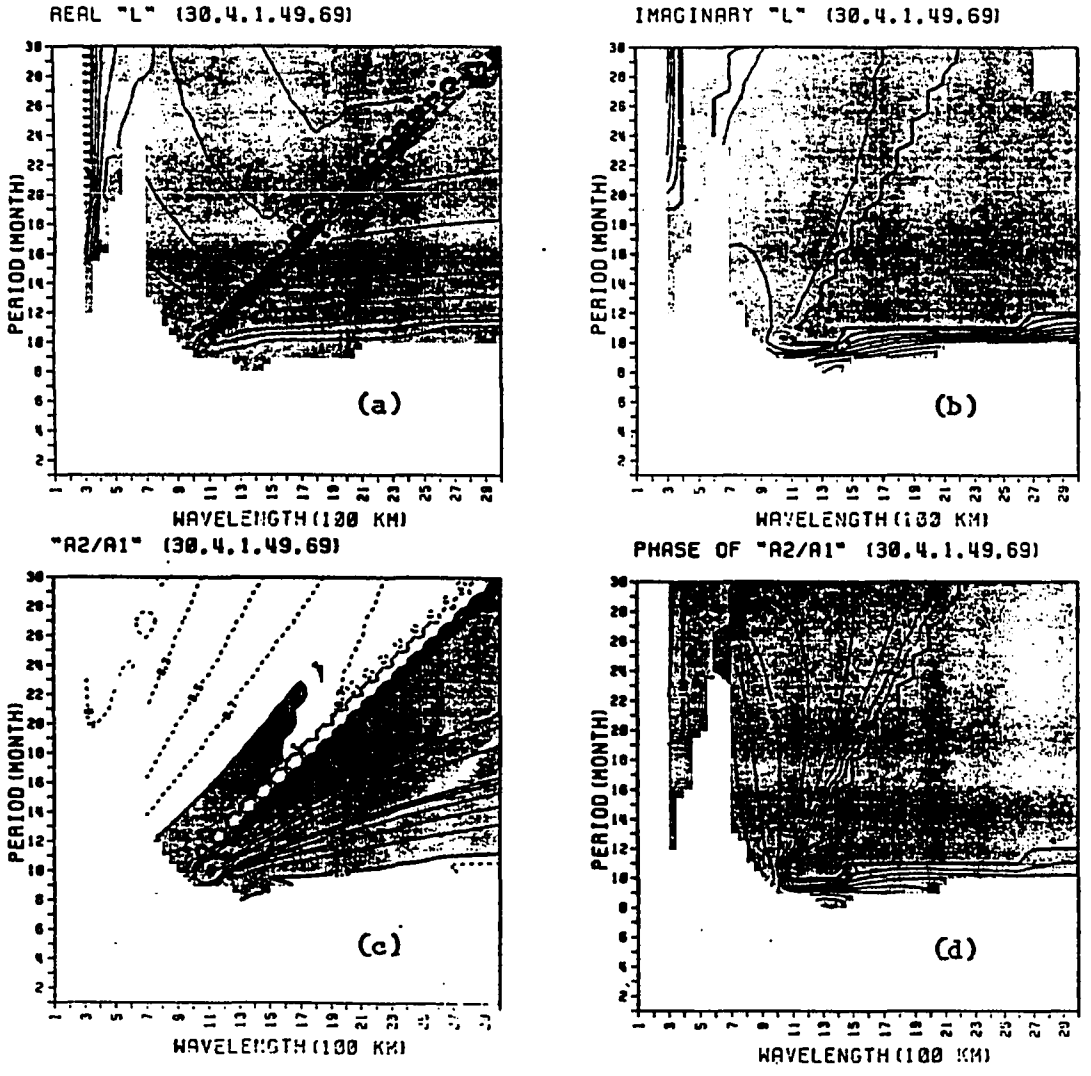

Figure 3.2 (a) Real part (ℓ_r) and (b) imaginary part (ℓ_i) of cross-flow wavenumber, and (c) magnitude and (d) phase of amplitude ratio (A_2/A_1) for shear I, radii I, and a 30° flow.

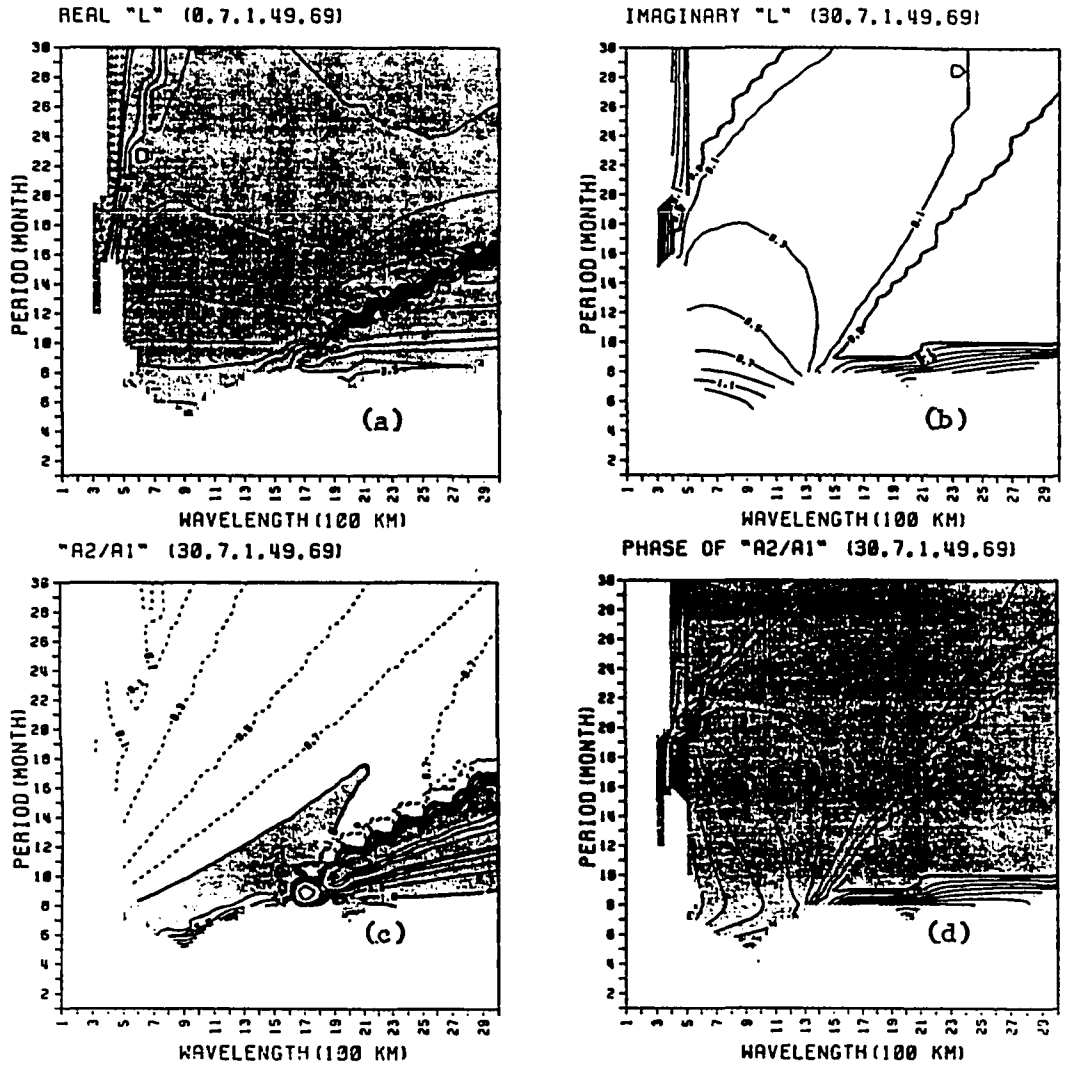

Figure 3.3 (a) Real part (ℓ_r) and (b) imaginary part (ℓ_i) of cross-flow wavenumber, and (c) magnitude and (d) phase of amplitude ratio (A_2/A_1) for shear II, radii I, and a 30° flow.

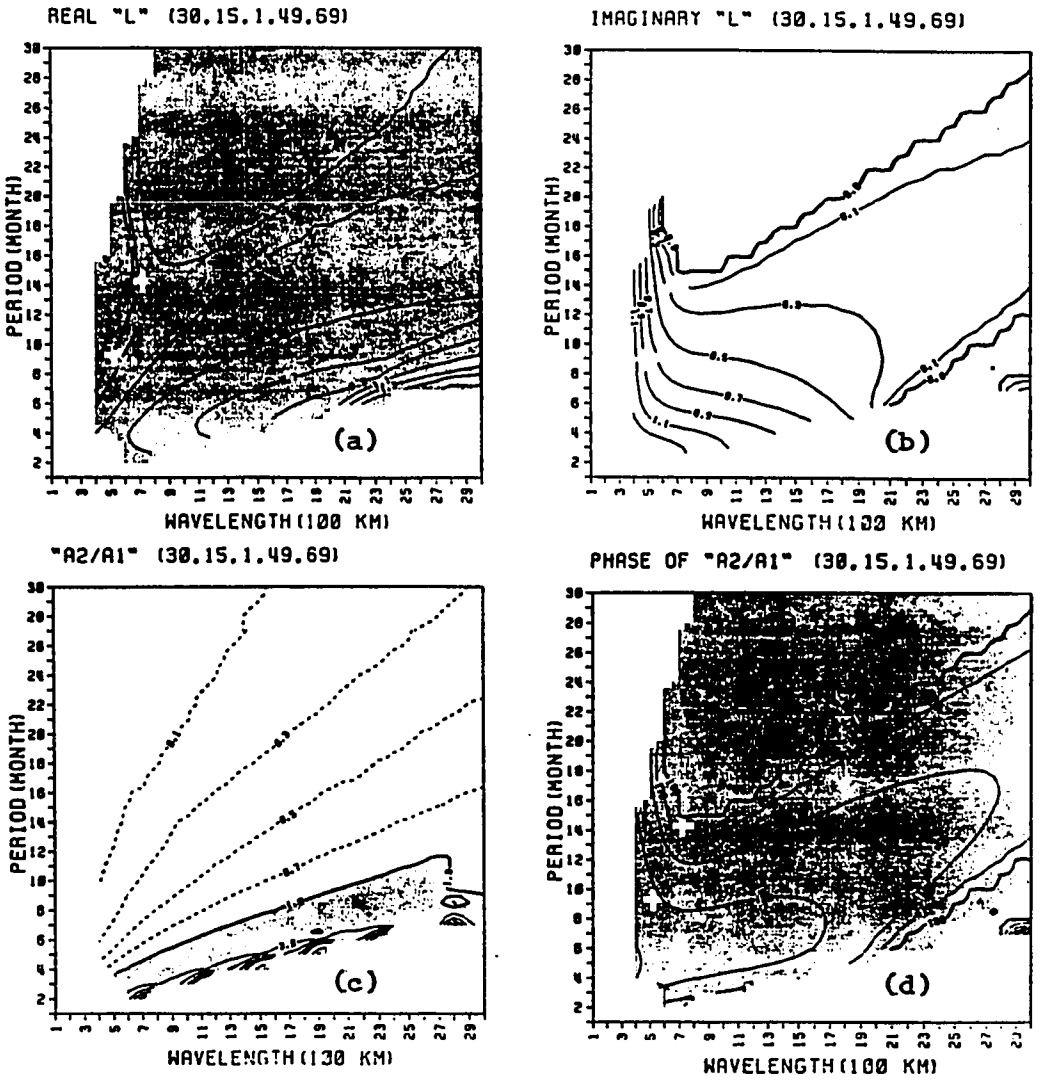

Figure 3.4 (a) Real part (ℓ_r) and (b) imaginary part (ℓ_i) of cross-flow wavenumber, and (c) magnitude and (d) phase of amplitude ratio (A_2/A_1) for shear III, radii, and a 30° flow.

are found in the MBB region. The size and location of each region in period-wavelength space vary with vertical shear. Figs. 3-2, 3-3, and 3-4 show that as the vertical shear increases, the PBSI region increases only slightly (similar to the zonal case), the MBB region increases greatly, and the PBBI region decreases drastically.

In the PBSI region the ranges of radiation wavenumbers are $0.01\text{-}1.04\text{x}10^{-7}$, $0.03\text{-}0.76\text{x}10^{-7}$, and $0.11\text{-}0.49\text{x}10^{-7}$ cm^{-1} for shears I, II, and III, respectively. As in the zonal case the radiation phase speeds generally increase (the radiation wavenumbers generally decrease) with increasing vertical shear. However, the radiation phase speeds are slightly higher in the nonzonal case than in the zonal case. The radiation phase speed change with changing phase speed of a disturbance is in a similar manner to those in the zonal case. In this region the ranges of amplitude ratios are 0.01-0.2, 0.0-0.26, and 0.0-0.32 for shears I, II, and III, respectively. The amplitude ratios appear to increase slightly with vertical shear. The amplitude ratios decrease with the phase speed of the disturbance, as in the zonal case, for shears I and III but increase with both wavelength and period for shear II.

The PBBI region is located on the long wavelength and short period side of the critical layer line in period-wavelength space. This region rarely agrees with

the observed dominant ranges of wavelengths and periods. The amplitude ratios indicate that the radiation region is purely baroclinic as in the PBSI region, but it is bottom-intensified. The radiation wavenumbers are in general higher in this region than in the PBSI region. In this PBBI region the radiation wavenumbers decrease with increasing vertical shear as in the PBSI region. The change of the radiation wavenumber with changing phase speed of a disturbance is opposite to that in the PBSI region, except for the case of shear II in which they are similar. The amplitude ratios are large, up to infinity, in this PBBI region.

The MBB region is located between the two pure baroclinic regions. In this region the radiation wavenumber has both real and imaginary parts, indicating that the radiation occurs, with amplitude decaying in the cross-flow direction. The size of the MBB region in period-wavelength space increases greatly with increasing vertical shear. Most importantly, the radiation region extends to shorter wavelengths and periods than in the PBSI and PBBI regions. Therefore, much of the wavelengths and periods in this MBB region overlap the observed dominant wavelengths and periods. Defining a realistic radiation region as a region with a length scale of decay (or e-folding length scale) of 500 km, the shortest possible pairs of wavelength and period are, with shears I, II, and

III, 700 km; 12 months, 500 km; 10 months, and 600 km; 8 months, respectively. For a fixed wavelength of 800 km and a period of 12 months, the corresponding length scales of decay are 785, 628, and 1013 km for shears I, II, and III, respectively. The shorter length scale of decay found for shear II seems to be related to the smaller radiation region seen for shear II in the purely zonal case. The occurence of the small length scale of decay is probably due to a larger ℓ_i caused by the flow speeds being closer to the phase speed for shear II than for other shears. For the observed range of wavelengths and periods, the range of length scales of decay is 500-1000 km, and the range of the radiation wavenumber is $0.15\text{-}1.5\text{x}10^{-7}$ cm^{-1}, decreasing with the vertical shear. In this region the radiation phase speed increases with increasing vertical shear and also increases with increasing phase speed of the disturbance. The radiation phase speed at wavelengths and periods overlapping the observed dominant phase speed ranges from 1 cm/sec to 2.5 cm/sec.

For the observed dominant range of wavelengths, the magnitude of the amplitude ratios is 0.3-1.1, also decreasing with the vertical shear. The phase of the amplitude ratio increases with increasing vertical shear. The amplitude ratio indicates that the radiation region becomes more surface-intensified and also becomes closer to baroclinic, as the vertical shear increases. The amplitude

ratio increases with the phase speed of a disturbance for all three background shears as in the zonal case and in the PBSI region.

c. Effect of changing orientation of flow and disturbance on radiation

In the previous two sections, we have seen that the radiation region in period-wavelength space is larger, and furthermore, broader ranges of wavelengths and periods overlap the observed dominant ranges in the nonzonal case than in the zonal case.

In order to see further the effect of changing orientation of the flow and disturbance on radiation, a solution is obtained as a function of the flow orientation and wavelength of a disturbance for given shear II, radii I, and a period of 12 months (an observed dominant period). The solution is displayed in Figs. 3.5a-d. The figures show clearly the effect of changing flow orientation on the wavelength range of radiating waves (the shaded area in Fig. 3.5a). The figures also show a symmetry about 180^{o}, indicating an applicability of the previously discussed 30^{o} flow case in the case of a 330^{o} flow orientation.

The distribution of the radiation wavenumber (positive signs for the solid line and negative signs for the dotted line in Fig. 3.5a) indicates outward radiation

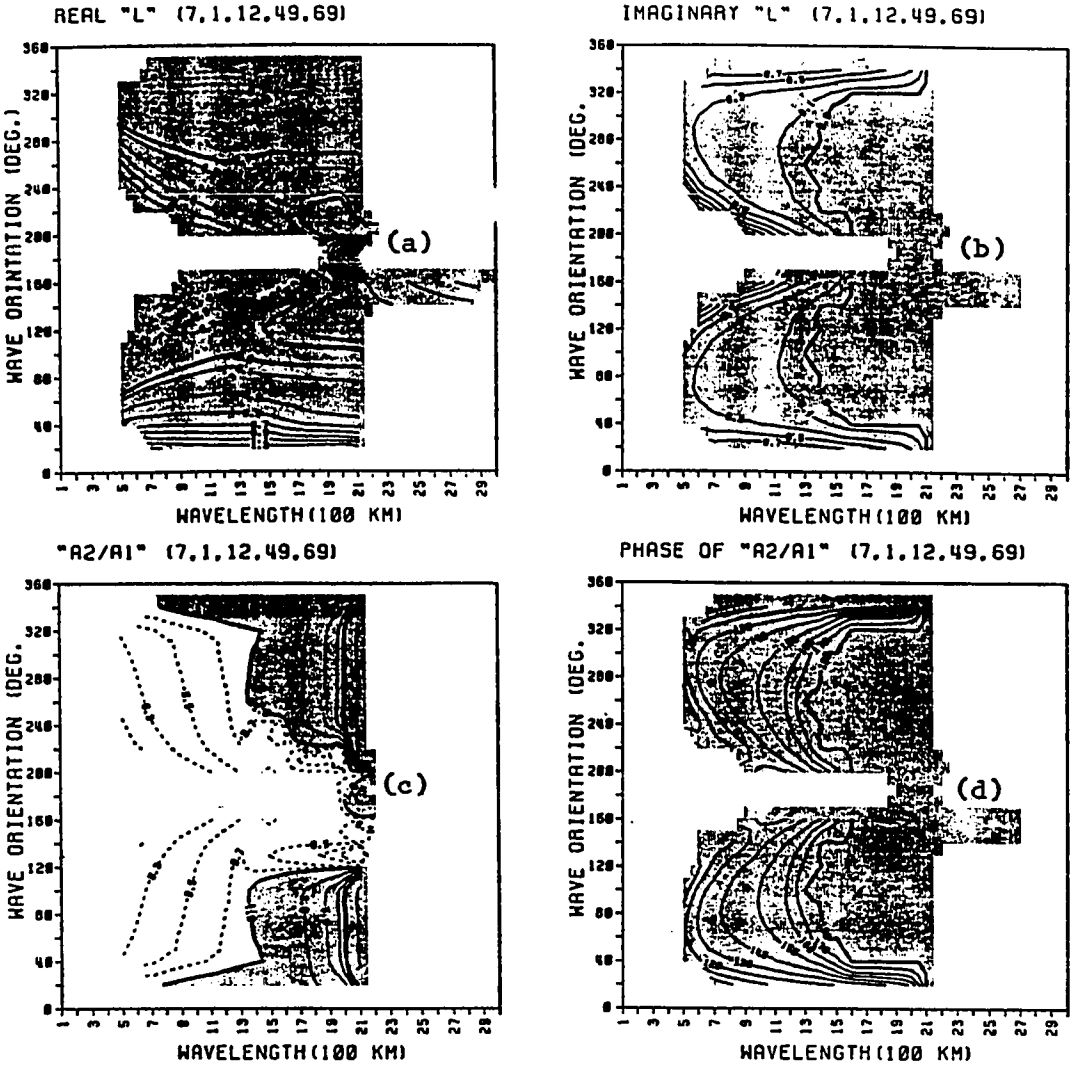

Figure 3.5 (a) Real part (ℓ_r) and (b) imaginary part (ℓ_i) of cross-flow wavenumber, and (c) magnitude and (d) phase of amplitude ratio (A_2/A_1) as a function of wavelength and wave direction for shear II, radii I, and a period of 12 months.

away from the source. The imaginary wavenumbers in Fig. 3.5b indicate that the length scale of decay increases as the flow orientation changes from 20^{o} to 60^{o}. The radiation also becomes more surface-intensified and closer to baroclinic as the flow orientation changes from 20^{o} to 60^{o}.

If one considers the KEC as a zonal flow, the observed dominant range of wavelengths of the internal temperature fluctuations can hardly be explained by this process. However, if one considers the KEC as a 30^{o} flow, the computed wavelengths are within the observed dominant range, and the computed length scales of decay are comparable with the observed length scales of decay seen in standard deviation of the temperature fluctuations. In general, as the flow orientation approaches 60^{o} (an approximate orientation of the Kuroshio Current), the wavelength range, length scale of decay, and layer of intensification tend to be more reaslistic.

d. Effect of changing stratification on radiation

Depending on how stably stratified the ocean is, the size of each radiation region varies. The effect of stratification on radiation can be determined by comparing Figs. 3.3, 3.6, and 3.7. The sizes of the PBSI and PBBI regions seem to depend more on changing depth ratio

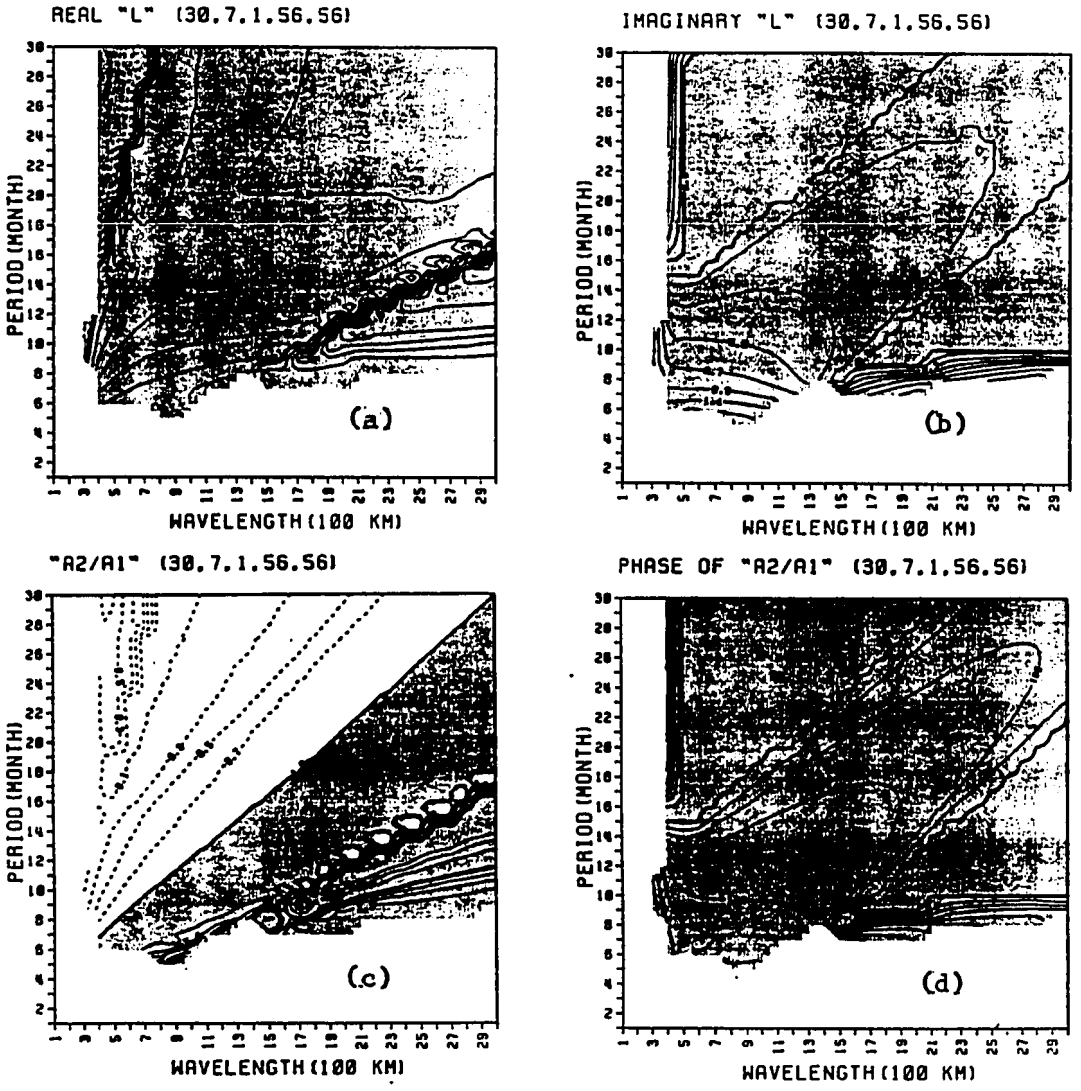

Figure 3.6 (a) Real part (ℓ_r) and (b) imaginary part (ℓ_i) of cross-flow wavenumber, and (c) magnitude and (d) phase of amplitude ratio (A_2/A_1) for shear II, radii II, and a 30° flow.

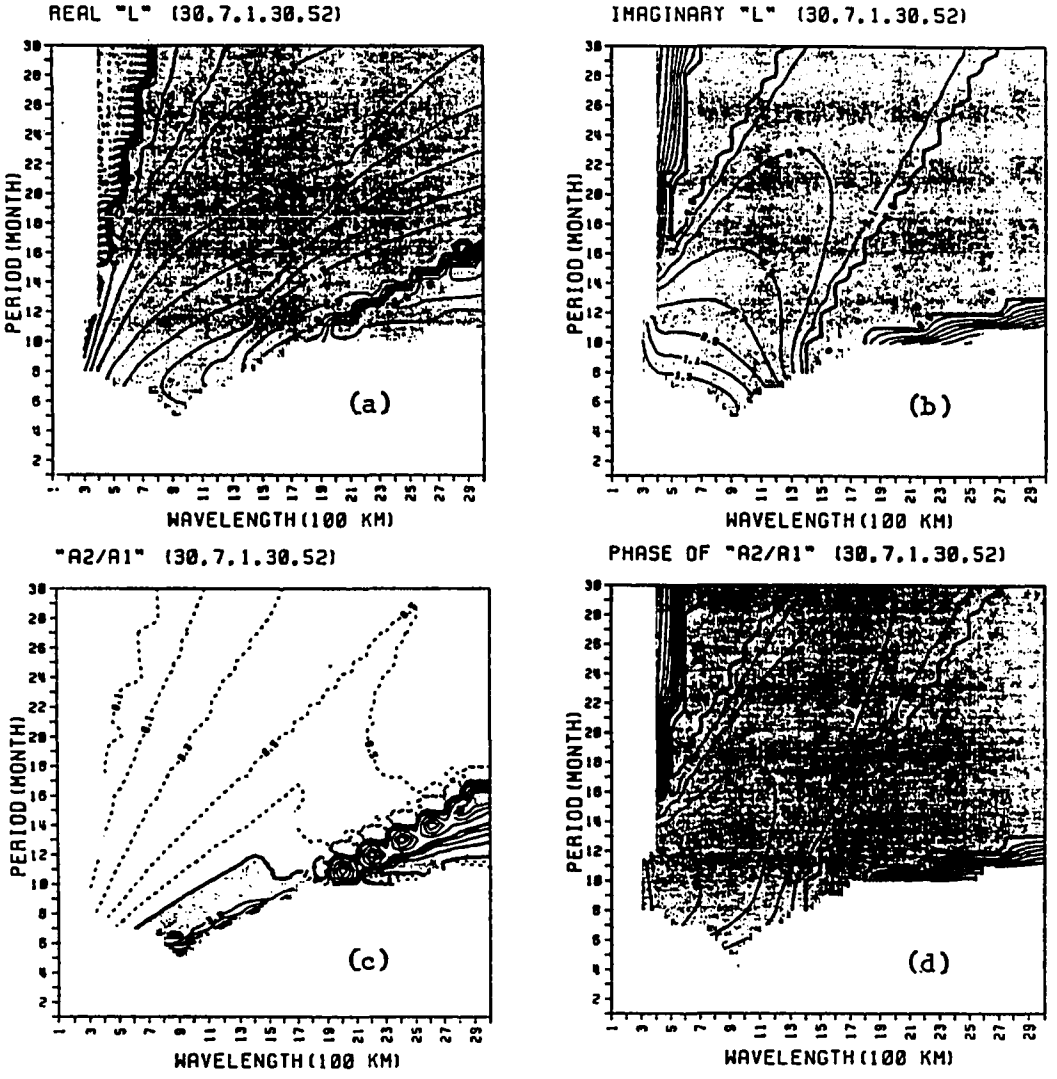

Figure 3.7 (a) Real part (ℓ_r) and (b) imaginary part (ℓ_i) of cross-flow wavenumber, and (c) magnitude and (d) phase of amplitude ratio (A_2/A_1) for shear II, radii III, and a 30° flow.

(D_1/D_2) than on changing density difference between the layers ($\Delta\rho/\rho$) as indicated by changing size of the radiation region. The PBSI region is larger for a larger depth ratio (i.e., the case of radii II), while the PBBI region is smaller. In both the PBSI and PBBI regions the amplitude ratios are larger in the case of radii II, indicating more energy penetrating into the lower layer when both layer depths are the same. In the MBB region where the radiation occurs in the ranges of wavelengths and periods of the disturbance overlaping the observed ranges, the length scales of decay are larger for larger D_1/D_2 and for larger $\Delta\rho/\rho$ (i.e., the cases of radii II and I). For example, at a period of 11 months and a wavelength of 600 km the length scales of decay are 654, 542, and 350 km in the cases of radii II, I, and III, respectively. The radiation phase speeds are higher for less stable stratification (i.e., the case of radii III). The magnitude of the amplitude ratios are larger for the cases of radii II and I as in the PBSI and PBBI regions. The phase of the amplitude ratio is larger for the case of radii III than for the cases of other radii, indicating that the smaller the depth ratio is, the closer is the radiation becoming to baroclinic. Hence, it appears that in a two-layer system the radiation characteristics depends more on the depth ratio than on the size of an equivalent Rossby radius for a continuous water column.

In general, for the observed dominant wavelengths and periods, the radiation is more realistic (i.e., longer length scales of decay and more surface-intensified) for a larger D_1/D_2. Since the stratification with larger $\Delta\rho/\rho$ and larger D_1/D_2 is more likely to exist near the western boundary region (the stronger current region) along the KEC than in the interior region, the effect of stratification also seems to explain the regional tendency of the space and time scale distribution of the energetic temperature fluctuations in the far-field away from the strong current.

4. Summary and conclusions

In this chapter we have investigated the possibility of explaining the energetic temperature fluctuations away from strong currents by a "spatial instability" (by considering complex ℓ instead of complex ω), using a simple background shear flow structure and a propagating unstable disturbance in parallel with the flow. As suggested by Pedlosky (1977) a zonal eastward background flow and a propagating disturbance can radiate energy to the north and south. However, chances of radiation are slim for a disturbance with the observed space and time scales. When the orientation of the background flow and the traveling disturbance (both in the same direction) is

slightly rotated (30^{o}), the radiation characteristics become substantially different. The size of the radiation region in period-wavelength space becomes wide and, furthermore, broad ranges of wavelengths and periods overlap the observed wavelength and period ranges. In the nonzonal case, the radiation region consists of a pure baroclinic, surface-intensified region, a mixed baroclinic and barotropic region, and a pure baroclinic, bottom-intensified region. However, radiation in the observed dominant ranges of wavelengths and periods only occurs in the mixed baroclinic and barotropic region, where radiation is accompanied by amplitude decay towards the cross-flow direction. For the observed Rossby radii and realistic approximation of the flow speed in the KEC region, the length scales of decay are found to be 500-1000 km. This scales agree well with the observed length scales of decay inferred form the standard deviation of the internal temperature fluctuations.

The size of the mixed baroclinic and barotropic region changes greatly with changing vertical shear and moderately with changing Rossby radii. In general, as the background vertical shear increases, the analytical wavelengths and periods more overlap the observed ranges, and the length scales of decay become longer for given wavelength and period (within the observed ranges). The radiation phase speed for a disturbance at given wavelength

and period (within the observed ranges) increases with increasing vertical shear. In the mixed baroclinic and barotropic region with wavelength and period overlaping the observed ranges, the energy penetrates less into the lower layer and the wave away from the strong current is more nearly baroclinic as the vertical shear increases.

The radiation characteristics change more with changes in the depth ratio than with changes in the size of the equivalent Rossby radius for a continuous water column. The length scale of decay for a disturbance with the observed ranges of wavelengths and periods is larger when the depth ratio is larger. Also, more energy penetrates into the lower layer with a larger depth ratio while the wave becomes less baroclinic.

As a concluding remark, the distribution of standard deviation of internal temperature fluctuations with long length scales od decay to the north and south, the observed dominant length and time scales, and the eastward phase propagation along the KEC can be explained by the strong vertical shear and the existing stratification if the KEC is modeled as a nonzonal flow.

CHAPTER IV

RADIATING INSTABILITY OF NONZONAL CURRENTS

1. Introduction

In an effort to explain the fairly energetic internal temperature fluctuations observed in regions away from the KEC, we have examined radiation of energy from a disturbance traveling along a generally nonzonal flow (Chapter III). The result showed more radiation of energy in the nonzonal case than in the zonal case. Time scales, length scales, and phase speeds obtained for the nonzonal case appeared to be in ranges close to those observed. However, the flow structure used in the model was not so realistic.

In that model, the mean current was uniform in each horizontal direction. A next step towards greater realism could be the incorporation of a horizontal current profile similar to Talley's (1982) model used to study radiating instability. Three horizontal regions are now introduced. One represents the KEC and has a strong flow with strong vertical shear. It is flanked to the north and south by two other regions of weaker current and weaker vertical shear. The current and vertical shear in the flanking regions are equal.

There is, however, no horizontal shear in the linearized model used herein, and the geometry of the flanking regions is simpler than that used by Talley (1982) in order to obtain analytical solutions in the nonzonal cases. (Talley considered only the zonal case.)

The word radiate is commonly used to describe the propagation of neutrally stable waves which do not extract any energy from vertical or horizontal shear. Baroclinic instability implies the growth of a wave at the expense of available potential energy. The term radiating instability implies a mixture of both. All unstable currents have two types of instability, trapped and radiating ones. In the trapped instability, the instability energy from a source penetrates only a short distance into neighboring regions. On the other hand, the unstable radiating mode has a slowly decaying envelope imposed on the wavelike structure in the cross-flow direction. These waves look nearly like Rossby waves, since they neighbor stable, free, baroclinic Rossby waves in frequency-wavenumber space. The radiation takes the form of destabilized Rossby waves in regions away from the current. These modes thus have larger length scales of decay than those of the trapped modes.

In general, in the situation described in this chapter, there is one contiguous region of stable waves in frequency-wavenumber space, bordered by one contiguous region of unstable waves. The region of unstable waves is

sometimes further partitioned into one or more regions of radiating instability, adjacent to the region of stability, and a region of trapped instability. Sometimes the unstable region contains only trapped instabilities and sometimes only radiating instabilities.

The existence of the radiating modes requires an ambient potential vorticity gradient, as do Rossby waves. The existence of the radiating modes also crucially depends on the overlapping of the phase speeds and x-wavenumbers of the unstable perturbations with Rossby wave phase speeds and x-wavenumbers in the far-field. This is the phase speed condition of McIntyre and Weissman (1972). According to this condition, an unstable wave will not radiate if its eastward phase speed is greater than the flow speed in the far-field. Therefore, conditions for radiation in an eastward current are much more restrictive. In the more general nonzonal orientation of a mean flow and with certain phase speeds of disturbances in the flow and with certain vertical current shear in the far-field, radiating instabilities are possible. Talley (1982) demonstrated that the latter condition is particularly necessary for radiating instabilities.

The purpose of this chapter is to explore radiating instability of nonzonal shear flows in order to explain the characteristics of the temperature fluctuations observed in the mid-latitude North Pacific (Chapter I). First, we

derive a necessary condition for instability, and bounds on the real and imaginary phase speeds in nonzonal flows. Then cross-flow structure functions and related quantities are derived. Finally, the model is applied to three flow orientations; 0^{o} (strictly eastward), 30^{o}, and 60^{o}.

The model current used in this study is a rough approximation of the actual, observed flow in the mid-latitude western North Pacific. This flow structure is, however, much more realistic than that used in Chapter III. The model current is symmetric about y=0. Therefore, We only need to consider the +y half plane, divided into two regions of constant velocity using Rayleigh's (1879) broken line method.

2. Some general properties of a nonzonal flow instability

In order to determine differences in the characteristics of a nonzonal flow instability from a zonal one, a necessary condition for instability, and bounds on the real and imaginary phase speeds of unstable waves are derived using Pedlosky's (1979) approach. A general, linearized form of a non-dimensional potential vorticity equation for a basic flow and wave traveling in an arbitrary direction is

$$\left(\frac{\partial}{\partial t}+U\frac{\partial}{\partial X}\right)\left[\nabla_H^2\phi+\frac{\partial}{\partial z}\frac{1}{B}\frac{\partial\phi}{\partial z}\right]+\frac{\partial\phi}{\partial x}\frac{\partial\Pi}{\partial y}-\beta\sin\theta\frac{\partial\phi}{\partial y}=0 \qquad (4\text{-}1)$$

where $\frac{\partial \pi}{\partial y} = \beta\cos\theta - \frac{\partial^2 U}{\partial y^2} - \frac{\partial}{\partial z}\frac{1}{B}\frac{\partial U}{\partial z}$, B is the Burger number (which is given as R_i^2/L^2, where R_i is the internal Rossby radius and L is the characteristic length scale), and θ is the orientation of the flow and wave. Boundary conditions are assumed to be,

$$\frac{\partial \phi}{\partial x} = 0 \quad \text{at} \quad y = \pm 1$$

and

$$\frac{\partial \phi}{\partial z} = 0 \quad \text{at} \quad z = 0, -H$$

Assuming a form of the solution

$$\phi = Re\, \Phi(y,z)\, e^{ik(x-ct)} \tag{4-2}$$

where Re denotes the real part of the expression it prefaces, and substituting (4-2) in (4-1), one obtains

$$(U-c)\left[\frac{\partial^2 \Phi}{\partial y^2} + \frac{\partial}{\partial z}\frac{1}{B}\frac{\partial \Phi}{\partial z} - k^2\Phi\right] + \Phi\frac{\partial \pi}{\partial y} + \frac{i\beta\sin\theta}{k}\frac{\partial \Phi}{\partial y} = 0 \tag{4-3}$$

In order to derive the necessary condition for instability, (4-3) is multiplied by Φ^* ($*$ denotes complex conjugation) and, after some manipulations, the resultant equation is integrated over the meridional plane, using the boundary conditions. The equation then becomes

$$\int_{-1}^{1} dy \int_{-H}^{0} dz \left(\frac{1}{B}\left|\frac{\partial \Phi}{\partial y}\right|^2 + \left|\frac{\partial \Phi}{\partial y}\right|^2 + k^2|\Phi|^2\right) = \int_{-1}^{1} dy \int_{-H}^{0} dz \frac{|\Phi|^2}{U-c}\frac{\partial \pi}{\partial y}$$

$$+ \frac{i\beta\sin\theta}{k}\int_{-1}^{1} dy \int_{-H}^{0} dz \frac{\Phi^*}{U-c}\frac{\partial \Phi}{\partial y}. \tag{4-4}$$

Since

$$\frac{1}{U-c} = \frac{U-c_r+ic_i}{|U-c|^2},$$

the imaginary part of (4-4) may yield

$$C_i \int_{-1}^{1} dy \int_{-H}^{0} dz \frac{|\Phi|^2}{|U-c|^2} \frac{\partial \pi}{\partial y}$$
$$= \frac{\beta \sin\theta}{k} \int_{-1}^{1} dy \int_{-H}^{0} dz \frac{1}{|U-c|^2} [c_i (\Phi^* \frac{\partial \Phi}{\partial y})_i - (U-c_r)(\Phi^* \frac{\partial \Phi}{\partial y})_r] \qquad (4-5)$$

where the subscripts r and i indicate real and imaginary parts. Equation (4-5) is the necessary condition for instability in a general nonzonal flow. If $\theta=0$ (a zonal flow), (4-5) becomes equation (7.4.22) of Pedlosky (1979) for the boundary conditions as used in this study. In the zonal case, (4-5) indicates that if the mode is to become unstable, the potential vorticity gradient of the basic current must be positive in some subregions of the meridional plane and negative in others.

Since Φ vansihes on $y=\pm 1$, Φ may be expressed as a Fourier series.

$$\Phi = \sum_{j=0}^{\infty} A_j \cos(j+\tfrac{1}{2})\pi y \qquad (4-6)$$

Using (4-6), one can rewrite (4-5), whenever $\theta \neq 0$,

$$C_i = \frac{\frac{\beta \sin\theta}{k} \int_{-1}^{1} dy \int_{-H}^{0} dz \left\{ \frac{U-c_r}{|U-c|^2} \sum_{j=0}^{\infty} |A_j|^2 (j+\frac{1}{2})\frac{\pi}{2} \sin 2(j+\frac{1}{2})\pi y \right\}}{\int_{-1}^{1} dy \int_{-H}^{0} dz \left\{ \frac{1}{|U-c|^2} \frac{\partial \pi}{\partial y} \sum_{j=0}^{\infty} |A_j|^2 \frac{1}{2} [1+\cos 2(j+\frac{1}{2})\pi y] \right\}} \qquad (4-7)$$

In the zonzonal case, the flow may be unstable (i.e., $C_i>0$) for some combinations of θ and $U-C_r$ even if the distribution of the potential vorticity gradients in the meridional plane is not positive in some subregions and negative in others.

In order to obtain the range of allowable real and imaginary phase speeds for a given U(y,z), (4-3) is written

in terms of N (= ϕ/U-C).

$$(U-c)\left[\frac{\partial^2 N(U-c)}{\partial y^2}+\frac{\partial}{\partial z}\frac{1}{B}\frac{\partial N(U-c)}{\partial z}-k^2 N(U-c)\right]+N(U-c)\frac{\partial \pi}{\partial y}$$
$$+\frac{i\beta\sin\theta}{k}\frac{\partial N(U-c)}{\partial y}=0. \qquad (4\text{-}8)$$

The boundary conditions also become

$$N=0, \quad y=\pm 1$$

and

$$\frac{\partial N}{\partial z}=0, \quad z=0, -H$$

With some manipulations, (4-8) then becomes

$$\frac{\partial}{\partial z}\left[\frac{1}{B}(U-c)^2\frac{\partial N}{\partial z}\right]+\frac{\partial}{\partial y}\left[(U-c)^2\frac{\partial N}{\partial y}\right]-k^2 N(U-c)^2+N(U-c)\beta\cos\theta$$
$$+\frac{i\beta\sin\theta}{k}\frac{\partial N(U-c)}{\partial y}=0. \qquad (4\text{-}9)$$

If (4-9) is multiplied by N^* and integrated over the meridional plane, one obtains

$$\int_{-1}^{1}dy\int_{-H}^{0}dz\,(U-c)^2\left\{\frac{1}{B}\left|\frac{\partial N}{\partial z}\right|^2+\left|\frac{\partial N}{\partial y}\right|^2+k^2|N|^2\right\}$$
$$=\int_{-1}^{1}dy\int_{-H}^{0}dz\left[(U-c)\beta\cos\theta+\frac{i\beta\sin\theta}{k}\frac{\partial U}{\partial y}\right]|N|^2$$
$$+\frac{i\beta\sin\theta}{k}\int_{-1}^{1}dy\int_{-H}^{0}dz\,(U-c)N^*\frac{\partial N}{\partial y}. \qquad (4\text{-}10)$$

(4-10) can be divided into real and imaginary parts. The imaginary part is

$$c_r\int_{-1}^{1}dy\int_{-H}^{0}dz\,P=\int_{-1}^{1}dy\int_{-H}^{0}dz\,UP-\frac{\beta\cos\theta}{2}\int_{-1}^{1}dy\int_{-H}^{0}dz\,J$$
$$+\frac{\beta\sin\theta}{2kc_i}\int_{-1}^{1}dy\int_{-H}^{0}dz\frac{\partial U}{\partial y}J$$
$$+\frac{\beta\sin\theta}{2kc_i}\int_{-1}^{1}dy\int_{-H}^{0}dz\left[\left(N^*\frac{\partial N}{\partial y}\right)_r(U-c_r)+\left(N^*\frac{\partial N}{\partial y}\right)_i c_i\right] \qquad (4\text{-}11)$$

where

$$P=\frac{1}{B}\left|\frac{\partial N}{\partial z}\right|^2+\left|\frac{\partial N}{\partial y}\right|^2+k^2|N|^2$$

$$J=|N|^2$$

and the real part is

$$\int_{-1}^{1}dy\int_{-H}^{0}dz\,[U^2-2C_rU+C_r^2-C_i^2]\,P=\beta\cos\theta\int_{-1}^{1}dy\int_{-H}^{0}dz\,UJ$$
$$-\beta\cos\theta\,C_r\int_{-1}^{1}dy\int_{-H}^{0}dz\,J$$
$$+\frac{\beta\sin\theta}{k}\int_{-1}^{1}dy\int_{-H}^{0}dz\left[\left(N^*\frac{\partial N}{\partial y}\right)_r C_i-\left(N^*\frac{\partial N}{\partial y}\right)_i(U-C_r)\right]. \qquad (4\text{-}12)$$

Expressing N as a Fourier series,

$$N=\sum_{j=0}^{\infty}B_j\cos(j+\tfrac{1}{2})\pi y \qquad (4\text{-}13)$$

and using the relation,

$$N^*\frac{\partial N}{\partial y}=\sum_{j=0}^{\infty}|B_j|^2(j+\tfrac{1}{2})\frac{\pi}{2}\sin 2(j+\tfrac{1}{2})\pi y$$

one can rewrite (4-11),

$$C_r=\frac{\int_{-1}^{1}dy\int_{-H}^{0}dz\,UP}{\int_{-1}^{1}dy\int_{-H}^{0}dz\,P}-\frac{\frac{\beta\cos\theta}{2}\int_{-1}^{1}dy\int_{-H}^{0}dz\,J}{\int_{-1}^{1}dy\int_{-H}^{0}dz\,P}+\frac{\frac{\beta\sin\theta}{2kC_i}\int_{-1}^{1}dy\int_{-H}^{0}dz\,\frac{\partial U}{\partial z}J}{\int_{-1}^{1}dy\int_{-H}^{0}dz\,P}$$
$$+\frac{\frac{\beta\sin\theta}{2kC_i}\int_{-1}^{1}dy\int_{-H}^{0}dz\,(U-C_r)\sum_{j=0}^{\infty}|B_j|^2(j+\frac{1}{2})\frac{\pi}{2}\sin 2(j+\frac{1}{2})\pi y}{\int_{-1}^{1}dy\int_{-H}^{0}dz\,P} \qquad (4\text{-}14)$$

Since

$$\int_{-1}^{1}dy\left|\frac{\partial N}{\partial y}\right|^2=\sum_{j=0}^{\infty}|B_j|^2\pi^2(j+\tfrac{1}{2})^2\geq\sum_{j=0}^{\infty}|B_j|^2\frac{\pi^2}{4}$$

and

$$\int_{-1}^{1}dy\,|N|^2=\sum_{j=0}^{\infty}|B_j|^2$$

it follows that

$$\int_{-1}^{1}dy\int_{-H}^{0}dz\,P\geq(k^2+\frac{\pi^2}{4})\int_{-1}^{1}dy\int_{-H}^{0}dz\,J. \qquad (4\text{-}15)$$

Using (4-15) in (4-14) and taking $U=U_{max}$ and $\frac{\partial U}{\partial y}=(\frac{\partial U}{\partial y})_{max}$, one obtains

$$C_r\leq U_{max}+\frac{\beta\sin\theta}{2kC_i(k^2+\frac{\pi^2}{4})}\left(\frac{\partial U}{\partial y}\right)_{max},$$

and taking $U=U_{min}$, one obtains

$$C_r\geq U_{min}-\frac{\beta\cos\theta}{2(k^2+\frac{\pi^2}{4})}$$

Therefore, bounds on the real phase speed are

$$U_{min} - \frac{\beta \cos\theta}{2(k^2+\frac{\pi^2}{4})} \le C_r \le U_{max} + \frac{\beta \sin\theta}{2kC_i(k^2+\frac{\pi^2}{4})} \left(\frac{\partial U}{\partial y}\right)_{max}. \qquad (4\text{-}16)$$

If $\frac{\partial U}{\partial y}$ vanishes,

$$U_{min} - \frac{\beta \cos\theta}{2(k^2+\frac{\pi^2}{4})} \le C_r \le U_{max} \qquad (4\text{-}17)$$

which becomes equation (7.5.14) of Pedlosky (1979) if $\theta=0$ (a strictly eastward flow). In a nonzonal case ($\theta \neq 0$), (4-17) indicates that the lower bound of the phase speed is slightly higher than in the zonal case.

Consider now an obvious inequality

$$\begin{aligned} 0 &\ge \int_{-1}^{1} dy \int_{-H}^{0} dz\, (U-U_{max})(U-U_{min})P \\ &= \int_{-1}^{1} dy \int_{-H}^{0} dz \left\{ U^2P - (U_{max}+U_{min})UP + U_{max}U_{min}P \right\} \end{aligned} \qquad (4\text{-}18)$$

Substituting for $\int_{-1}^{1} dy \int_{-H}^{0} dz\, UP$ and $\int_{-1}^{1} dy \int_{-H}^{0} dz\, U^2P$ in (4-18) using (4-11) and (4-12) yields

$$\begin{aligned} 0 \ge & \left[C_r^2 + C_i^2 - (U_{max}+U_{min})C_r + U_{max}U_{min} \right] \int_{-1}^{1} dy \int_{-H}^{0} dz\, P \\ & + \beta \cos\theta \int_{-1}^{1} dy \int_{-H}^{0} dz \left(U - \frac{U_{max}+U_{min}}{2} \right) J \\ & + \left[\frac{U_{max}+U_{min}}{2} - C_r \right] \frac{\beta \sin\theta}{kC_i} \int_{-1}^{1} dy \int_{-H}^{0} dz\, \frac{\partial U}{\partial y} J \\ & + \left[\frac{U_{max}+U_{min}}{2} - C_r \right] \frac{\beta \sin\theta}{kC_i} \int_{-1}^{1} dy \int_{-H}^{0} dz\, (U-C_r) \sum_{j=0}^{\infty} |B_j|^2 (j+\tfrac{1}{2}) \frac{\pi}{2} \sin 2(j+\tfrac{1}{2})\pi y \end{aligned} \qquad (4\text{-}19)$$

Replacing U and $\frac{\partial U}{\partial y}$ by U_{min} and $\left(\frac{\partial U}{\partial y}\right)_{min}$, and using (4-15), (4-19) becomes

$$\begin{aligned} \left(\frac{U_{max}-U_{min}}{2}\right)^2 + \frac{\beta \cos\theta}{(k^2+\frac{\pi^2}{4})} \frac{U_{max}-U_{min}}{2} - \left[\frac{U_{max}+U_{min}}{2} - C_r \right] \frac{\beta \sin\theta}{kC_i(k^2+\frac{\pi^2}{4})} \left(\frac{\partial U}{\partial y}\right)_{min} \\ \ge \left(C_r - \frac{U_{max}+U_{min}}{2} \right)^2 + C_i^2 \end{aligned} \qquad (4\text{-}20)$$

If one considers the case of $\frac{\partial U}{\partial y}=0$, (4-20) becomes

$$\left(\frac{U_{max}-U_{min}}{2}\right)^2+\frac{\beta\cos\theta}{(k^2+\frac{\pi^2}{4})}\,\frac{U_{max}-U_{min}}{2} \geq \left(C_r-\frac{U_{max}+U_{min}}{2}\right)^2+C_i^2 \quad (4\text{-}21)$$

which becomes, in turn, equation (7.5.18) of Pedlosky (1979), if $\Theta=0$ (a strictly eastward flow case). Equation (4-21) indicates that the complex phase speeds of unstable waves must lie within a semi-circle in the C-plane whose radius is given by the square root of the left-hand side of (4-21). Equation (4-21) also indicates that the radius is smaller in the nonzonal case than in the zonal case.

3. Formulation of radiating instability

In order to investigate the radiating instability of a nonzonal flow, the linearized, dimensional two-layer form of the potential vorticity equation in a rotated Cartesian coordinate system introduced in Chapter III (equation 3-1) is used.

$$\left(\frac{\partial}{\partial t}+U_n\frac{\partial}{\partial x}\right)\left[\left(\frac{\partial^2}{\partial x^2}+\frac{\partial^2}{\partial y^2}\right)\phi_n-\frac{1}{R_n^2}(-1)^n(\phi_2-\phi_1)\right]$$

$$+\frac{\partial\phi_n}{\partial x}\left[\beta\cos\theta-\frac{1}{R_n^2}(-1)^n U_s\right]-\frac{\partial\phi_n}{\partial y}\beta\sin\theta=0, \quad n=1,2 \qquad (4\text{-}22)$$

where ϕ_n represents the structure of the evolving perturbation field, Θ is a flow orientation with the usual convention, and $U_s=U_1-U_2$. Assuming a form of solution

$$\phi_n=\Phi_n(y)\,e^{i(kx-\omega t)} \qquad (4\text{-}23)$$

and substituting (4-23) in (4-22), one obtains for both layers

$$\frac{\partial^2 \Phi_1}{\partial y^2} + \frac{i\beta \sin\theta}{U_1 k - \omega} \frac{\partial \Phi_1}{\partial y} + \left[-k^2 - \frac{1}{R_1^2} + \frac{k(\beta \cos\theta + \frac{1}{R_1^2} U_s)}{U_1 k - \omega} \right] \Phi_1 + \frac{1}{R_1^2} \Phi_2 = 0, \quad (4\text{-}24a)$$

$$\frac{\partial^2 \Phi_2}{\partial y^2} + \frac{i\beta \sin\theta}{U_2 k - \omega} \frac{\partial \Phi_2}{\partial y} + \left[-k^2 - \frac{1}{R_2^2} + \frac{k(\beta \cos\theta - \frac{1}{R_2^2} U_s)}{U_2 k - \omega} \right] \Phi_2 + \frac{1}{R_2^2} \Phi_1 = 0. \quad (4\text{-}24b)$$

Assuming a cross-flow structure function

$$\Phi_n = A_n e^{ry}$$

and substituting this in (4-24a) and (4-24b), one obtains respectively

$$\frac{A_2}{A_1} = \frac{-\left[r^2 + \frac{i\beta \sin\theta}{U_1 k - \omega} r + \left[-k^2 - \frac{1}{R_1^2} + \frac{k(\beta \cos\theta + \frac{1}{R_1^2} U_s)}{U_1 k - \omega} \right] \right]}{\frac{1}{R_1^2}} \quad (4\text{-}25a)$$

and

$$\frac{A_2}{A_1} = \frac{-\frac{1}{R_2^2}}{r^2 + \frac{i\beta \sin\theta}{U_2 k - \omega} r + \left[-k^2 - \frac{1}{R_2^2} + \frac{k(\beta \cos\theta - \frac{1}{R_2^2} U_s)}{U_2 k - \omega} \right]} \quad (4\text{-}25b)$$

(4-25a) and (4-25b) are combined, yielding a relation for the cross-flow wavenumber r.

$$r^4 + Ar^3 + Br^2 + Cr + D = 0 \quad (4\text{-}26)$$

where

$$A = i\beta \sin\theta \left[\frac{1}{U_1 k - \omega} + \frac{1}{U_2 k - \omega} \right]$$

$$B = -2k^2 - \frac{1}{R_1^2} - \frac{1}{R_2^2} + \frac{k(\beta \cos\theta + \frac{1}{R_1^2} U_s)}{U_1 k - \omega} + \frac{k(\beta \cos\theta - \frac{1}{R_2^2} U_s)}{U_2 k - \omega} - \frac{\beta^2 \sin^2\theta}{(U_1 k - \omega)(U_2 k - \omega)}$$

$$C=\frac{i\beta\sin\theta}{U_1k-\omega}\left[-k^2-\frac{1}{R_2^2}+\frac{k(\beta\cos\theta-\frac{1}{R_2^2}U_s)}{U_2k-\omega}\right]$$
$$+\frac{i\beta\sin\theta}{U_2k-\omega}\left[-k^2-\frac{1}{R_1^2}+\frac{k(\beta\cos\theta+\frac{1}{R_1^2}U_s)}{U_1k-\omega}\right]$$

$$D=\left[-k^2-\frac{1}{R_1^2}+\frac{k(\beta\cos\theta+\frac{1}{R_1^2}U_s)}{U_1k-\omega}\right]\left[-k^2-\frac{1}{R_2^2}+\frac{k(\beta\cos\theta-\frac{1}{R_2^2}U_s)}{U_2k-\omega}\right]-\frac{1}{R_1^2R_2^2}$$

As shown in Fig. 4.1, the flow profile is symmetric about y=0. Therefore, a solution will be sought only for the region y>0. Assuming an infinitely wide ocean, the boundary conditions are

$\Phi_n\to 0$ as y=H→∞ (i.e., v→0 as y=H→∞ where v is a fluctuating current in the cross-flow direction).

$\frac{d\Phi_n}{dy}=0$ at y=0 (i.e., u=0 at y=0 where u is a fluctuating current in the along-flow direction).

The matching conditions at the interface, $y=y_o$, between Regions I and II are

$$\left[\frac{\Phi_n}{U_nk-\omega}\right]_{y=y_o}=0 \qquad (4\text{-}27a)$$

$$\left[(U_nk-\omega)\frac{d\Phi_n}{dy}\right]_{y=y_o}=0 \qquad (4\text{-}27b)$$

Equation (4-27a) stipulates that the displacement of the material interface between the two regions of the flow be the same in both regions on either sides of the interface. Equation (4-27b) stipulates that the tangential pressure gradient at the interface be equal on both sides of the interface.

Depending on the choice of boundary condition at y=0,

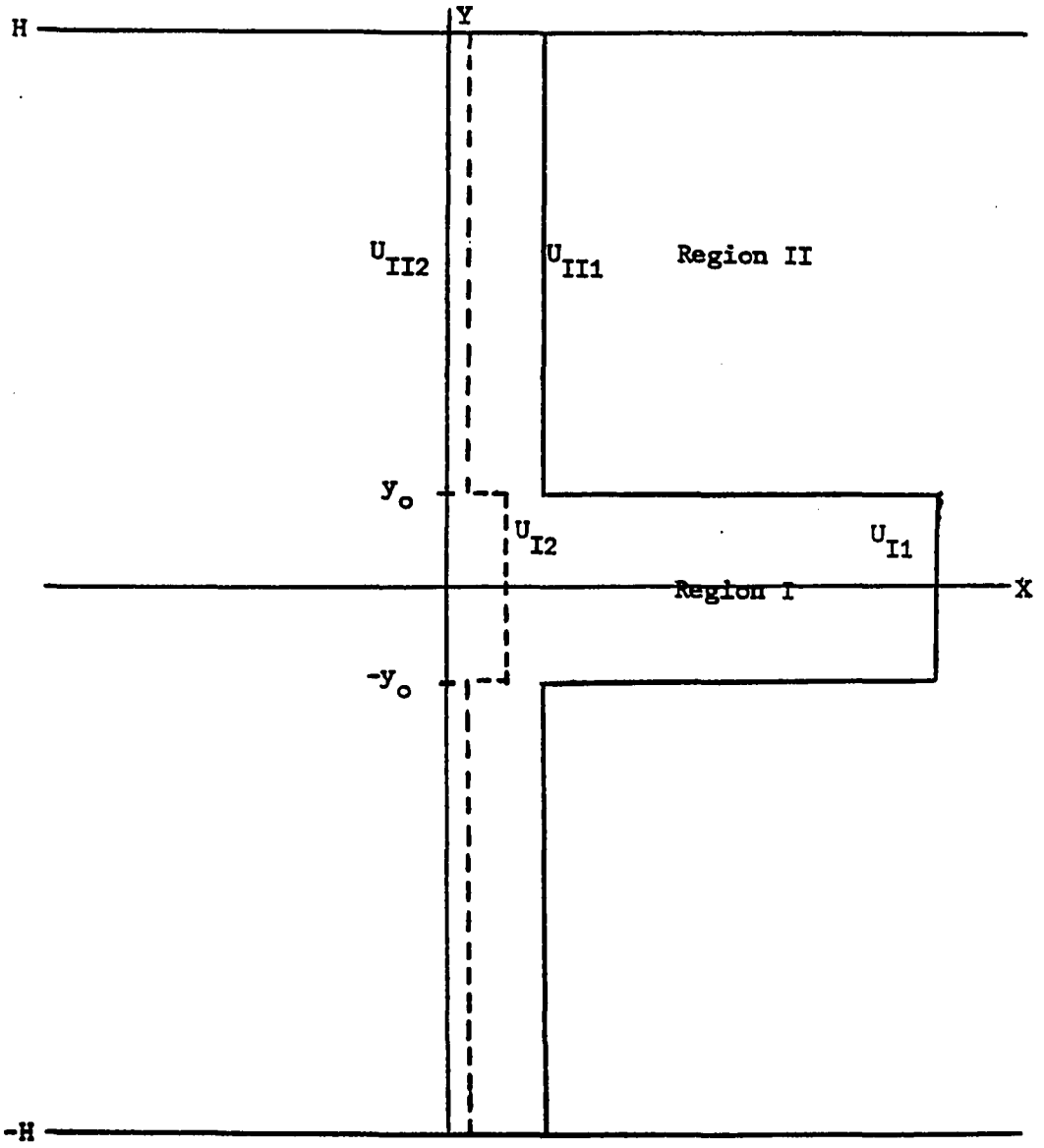

Figure 4.1 Flow structure of a two-layer system in the cross-flow direction. I and II indicate regions. 1 and 2 indicate the upper and lower layer, respectively.

there are two kinds of solutions. When the condition u=0 at y=0 (as in the present case) is used, a sinuous (antisymmetric) solution, which has an even eigenfunction, is obtained. When the condition v=0 at y=0 is used, a varicose (symmetric) solution, which has an odd eigenfunction, is obtained. The varicose mode tends to have a large amplitude of fluctuation at y=0. Rayleigh (1879) first used the word "varicosity" to describe the symmetric instability photographed in a lab experiment he performed. The sinuous mode tends to have large amplitudes in the far-fields.

In the present study, only the sinuous modes are sought since radiating instability results in large amplitude fluctuations in the far-field. In order to find cross-flow structure functions in Region II, one must obtain cross-flow wavenumbers by solving (4-26) with given parameters U_1, U_2, R_1 and R_2. Since (4-26) is a fourth order polynomial, there exist four roots. The two roots which satisfy the infinite boundary condition in Region II are taken. The structure functions in the upper and lower layers of Region II are

$$\Phi_{II1} = a_1 e^{m_1 y} + a_2 e^{m_2 y} \qquad (4\text{-}28a)$$

where Re $m_1<0$ and Re $m_2<0$, and

$$\Phi_{II2} = \left(\frac{A_2}{A_1}\right)_{m_1} a_1 e^{m_1 y} + \left(\frac{A_2}{A_1}\right)_{m_2} a_2 e^{m_2 y} \qquad (4\text{-}28b)$$

where $\left(\frac{A_2}{A_1}\right)_{m_1}$ and $\left(\frac{A_2}{A_1}\right)_{m_2}$ are the amplitude ratios between the upper and lower layers for the corresponding cross-flow

wavenumbers m_1 and m_2, respectively. Radiation is indicated by Φ_{III} and Φ_{II2} having wavelike structures in y-direction.

Using the boundary condition $\frac{d\Phi}{dy}=0$ at y=0, one can obtain the structure functions in the upper and lower layers of Region I.

$$\Phi_{I1}=C_1(d_1 e^{l_1 Y}-d_2 e^{l_2 Y}+e^{l_3 Y})+C_2(d_3 e^{l_1 Y}-d_4 e^{l_2 Y}+e^{l_4 Y}) \qquad (4\text{-}29a)$$

$$\Phi_{I2}=C_1(h_1 d_1 e^{l_1 Y}-h_2 d_2 e^{l_2 Y}+h_3 e^{l_3 Y})+C_2(h_1 d_3 e^{l_1 Y}-h_2 d_4 e^{l_2 Y}+h_4 e^{l_4 Y}) \qquad (4\text{-}29b)$$

where

$$h_1=\left(\frac{A_2}{A_1}\right)_{l_1}, \quad h_2=\left(\frac{A_2}{A_1}\right)_{l_2}, \quad h_3=\left(\frac{A_2}{A_1}\right)_{l_3}, \quad h_4=\left(\frac{A_2}{A_1}\right)_{l_4},$$

$$d_1=\frac{(h_2-h_3)l_3}{(h_1-h_2)l_1}, \quad d_2=\frac{(h_1-h_3)l_3}{(h_1-h_2)l_2}, \quad d_3=\frac{(h_2-h_4)l_4}{(h_1-h_2)l_1}, \quad d_4=\frac{(h_1-h_4)l_4}{(h_1-h_2)l_2}$$

where C_1 and C_2 are the undetermined coefficients.

Using the matching conditions at the interface between Regions I and II, one can reduce the number of the undetermined coefficients from four to one and a dispersion relation is obtained (see Appendix). By solving (4-26) and the dispersion relation simultaneously, one can find a number of unstable modes. Each mode is examined to see if it is radiating or trapped. The parameters defining the flow structure (Fig. 4.1) in the cases to be studied are shown in Table 4.1.

4. Results

The flow speeds in each of the four cases were chosen

Table 4.1 Four cases of flow conditions to be examined.

	Case I	Case II	Case III	Case IV
U_{I1} (cm/sec)	30	30	15	30
U_{I2} "	3	3	1	3
U_{II1} "	7	7	3	7
U_{II2} "	1	1	0	1
R_1 (km)	49	49	49	49
R_2 "	69	69	69	69
y_o "	200	200	200	200
θ (^{o})	0	30	30	60

U_{I1}=Flow speed in the upper layer of Region I
U_{I2}=Flow speed in the lower layer of Region I
U_{II1}=Flow speed in the upper layer of Region II
U_{II2}=Flow speed in the lower layer of Region II
R_1=Rossby radius in the upper layer $((g\Delta\rho/\rho D_1)^{1/2}/f)$
R_2=Rossby radius in the lower layer $((g\Delta\rho/\rho D_2)^{1/2}/f)$
y_o=A half-width of Region I in cross-flow direction

to approximate the known circulation as closely as possible. The flow speeds in Region I are the same as those used in Chapter II. The flow speeds in the upper layer of Region II were estimated by comparing the mean temperature gradients in the region where the current is unknown and 152°E, along the KEC, where the temperature gradient and the flow speed are known (Schmitz, 1984). The flow speeds in the lower layer of Region II were guesses. The approximate flow orientations of the KEC east of 152°E and the Kuroshio Current are 30° and 60°, respectively. The orientation of the southeastward branch of the KEC is taken to be 330°. However, since the radiational characteristics are almost the same between 30° and 330° cases as found in Chapter III, only the case of 30° orientation is investigated. The width of Region I is chosen to be 400 km (200 km between the x-axis and the northern boundary of Region I). The pair of Rossby radii (49 km; 69 km) are used as representative values near the western boundary (Chapters II and III). The zonal flow case is also examined for comparison with the nonzonal cases. In all cases, distinct modes are identified by frequency, growth rate, and real and imaginary phase speeds as functions of wavenumber. Each mode of solution is numbered arbitrarily but consistently from case to case, because of the similarity of the functions.

a. Case I (zonal flow with a strong vertical shear)

In this case, five modes of the solution exist in the frequency-wavenumber range considered (Fig. 4.2). In each mode, frequencies, phase speeds, growth rates, and imaginary phase speeds change nearly linearly with wavenumber, except for the growth rates and imaginary phase speeds in modes 3 and 4 where the variation with wavenumber shows a parabola-like shape. Table 4.2 shows the ranges of wave periods (T), wavelengths (L), phase speeds (C), growth periods (T_g), and imaginary phase speeds (C_i) of the unstable waves. The values presented are shown in two categories: a "solution range" comprising of both the trapped and radiating instabilities and a "radiation ranges" consisting of only the radiating instabilities, where they exist. (This terminology is used further in this chapter.) Three out of five modes contain radiating waves. Mode 1 exhibits only radiating instability. Modes 4 and 5 exhibits only trapped waves. In general, the trapped waves have short wavelengths and periods (e.g., modes 2 and 3) or high phase speeds (e.g., modes 4 and 5). Also, radiating waves in this case appear to have low growth rates.

In Figs. 4.3 and 4.4 the cross-flow structure of eigenfunctions are displayed with the accompanying T, L, C, T_g, and C_i for one or more representative wave(s) in

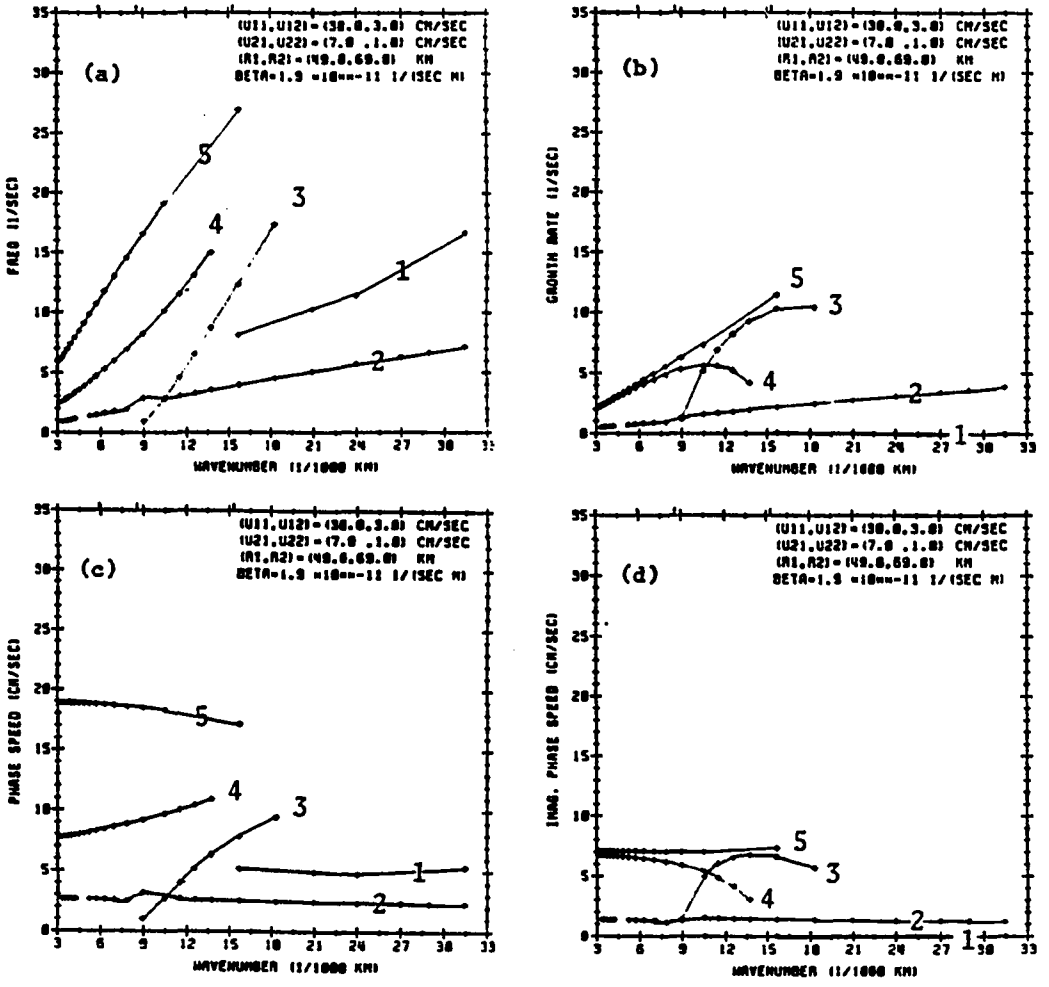

Figure 4.2 (a) Frequency [10^{-7} sec^{-1}], (b) growth rate [10^{-7} sec^{-1}], (c) phase speed [cm/sec], and (d) imaginary phase speed [cm/sec] as a function of wavenumber [10^{-8} cm^{-1}] for case I.

Table 4.2 Ranges of period (T), wavelength (L), phase speed (C), growth period (T_g), and imaginary phase speed (C_i) of (a) all unstable waves and of (b) radiating unstable waves present in each mode for case I. The underline in T_g indicates a unit of [years].

		mode 1	mode 2	mode 3	mode 4	mode 5
solution range	T [days]	43-91	101-727	42-814	42-291	27-121
	L [km]	200-400	200-2000	350-700	450-2000	400-2000
	C [cm/sec]	5-6	2-3	1-10	8-11	17-19
	T_g [days] [years]	139	182-4	69-580	128-364	63-331
	C_i [cm/sec]	0	1-2	1-7	3-7	7
radiation range	T [days]	43-91	143-727	814	only Trapped waves	only Trapped waves
	L [km]	200-400	300-2000	700		
	C [cm/sec]	5-6	3	1		
	T_g [days] [years]	139	252-4	580		
	C_i [cm/sec]	0	1	1		

Figure 4.3 Structure of eigenfunctions in the cross-flow direction for mode 1 in case I.

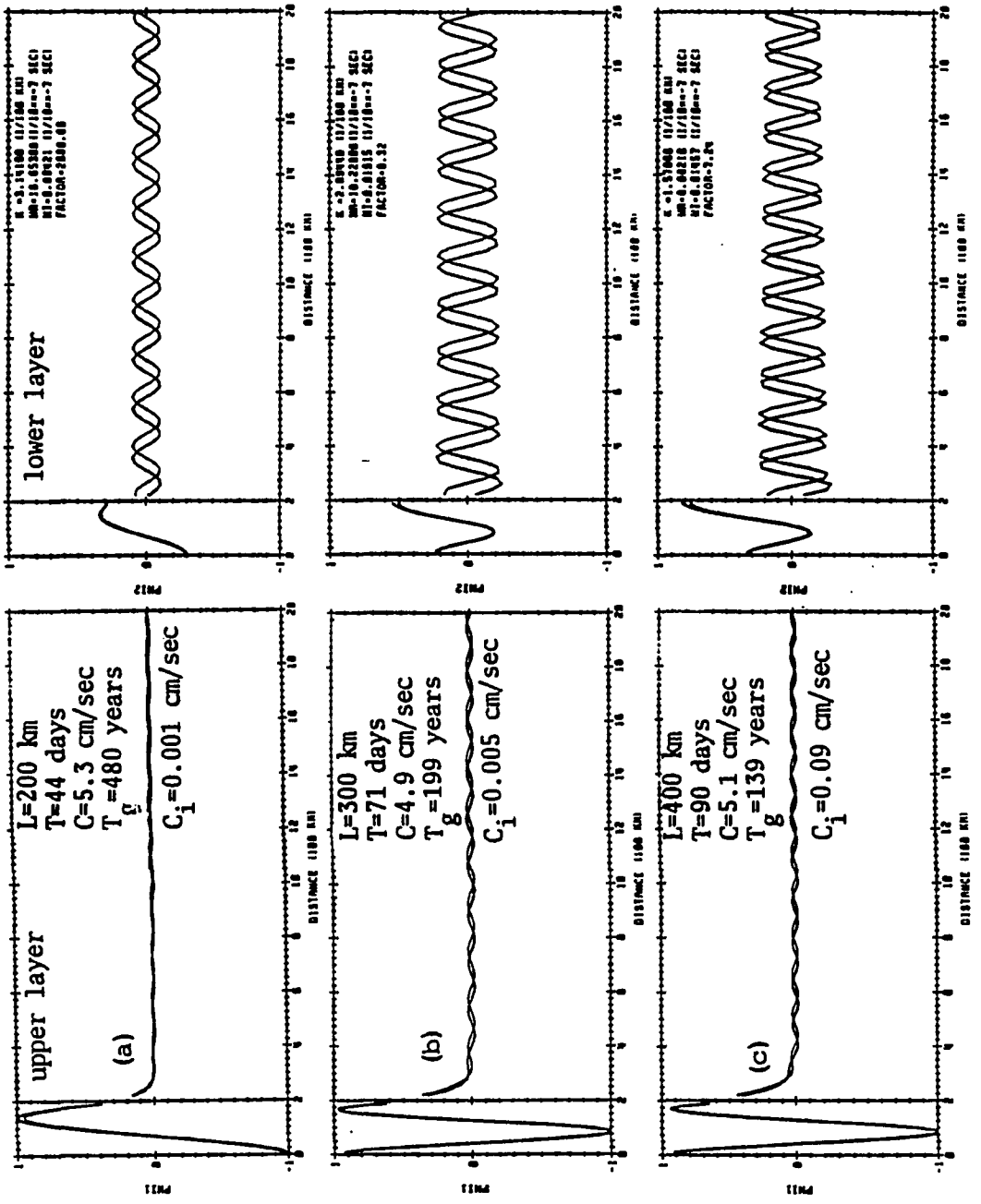

Figure 4.4 Structure of eigenfunctions in the cross-flow direction for (a) mode 2, (b) mode 2, and (c) mode 3 in case I.

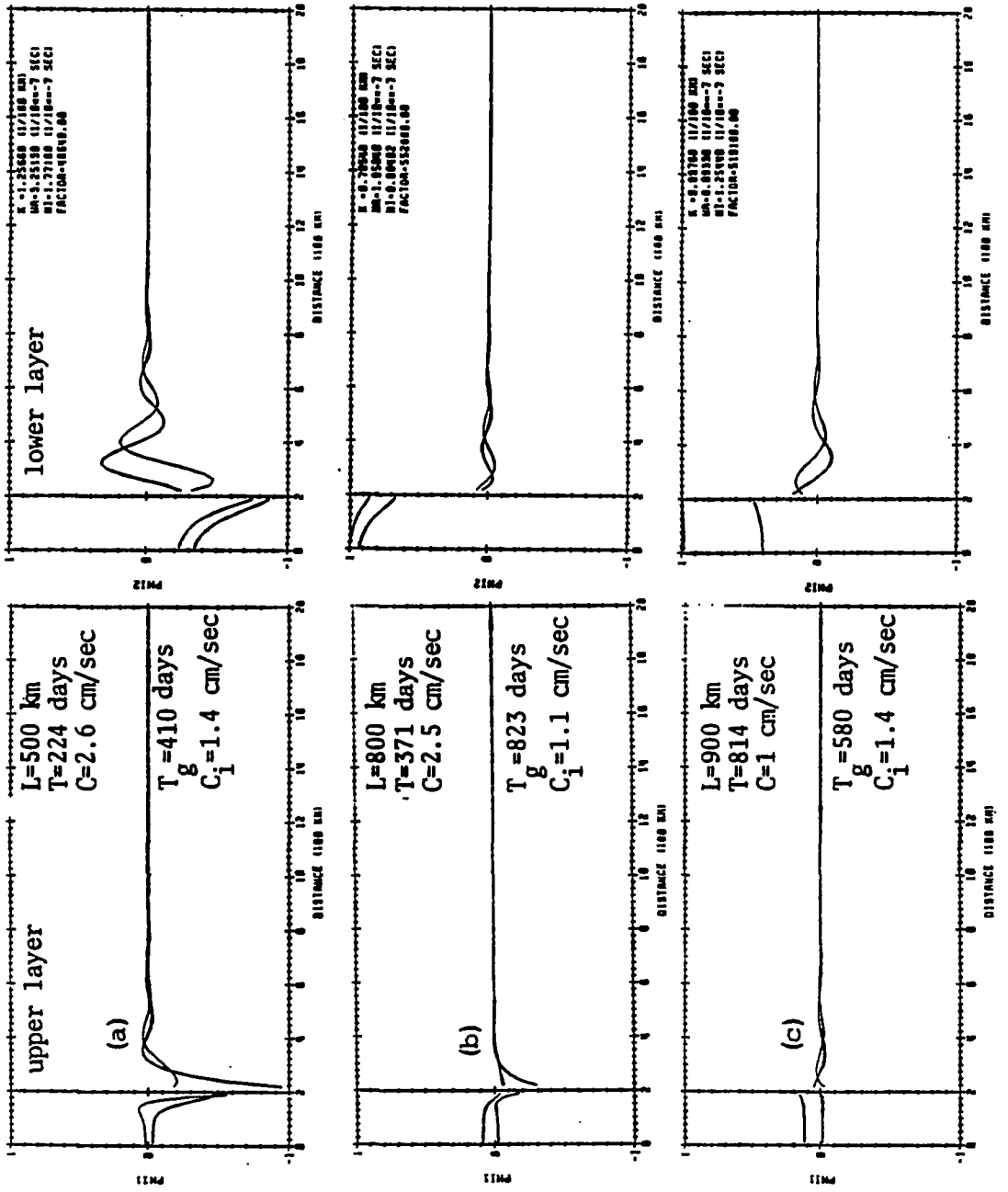

each mode. From the cross-flow structure, one can determine length scales of decay (hereafter referred to as LSOD) and which layer is intensified (i.e., surface or bottom, depending on the amplitudes of the upper and lower layer eigenfunctions). An LSOD is a distance between the line y=0 and a point in Region II where the amplitude decays to zero.

Radiating waves in mode 1 show very long LSODs and therefore are nearly like neutrally stable waves, and are obviously bottom-intensified. Fig. 4.3c show a wave which is the most comparable with the observed waves in this particular mode. The eigenfunctions of mode 2 show the maximum LSOD at a wavelength of 500 km and the minimum LSOD at a wavelength of 800 km (Figs. 4.4a-b). At wavelengths other than 500 and 800 km the LSOD slowly increases towards the maximum or slowly decreases towards the minimum. The radiating waves in mode 2 are bottom-intensified. Only one solution among those investigated is of the radiation type in mode 3. It has LSODs of 500-700 km and appears to be slightly bottom-intensified (Fig. 4.4c).

A radiating wave is deemed comparable to an observed one whenever the wave period, wavelength, phase speed, growth rate, LSOD are comparable. Furthermore, the theoretical wave must be surface-intensified, to be consistent with the generally observed tendency of the ocean to exhibit larger temperature fluctuations in the

upper thermocline as opposed to the deep ocean. The observed dominant ranges in the KEC region are wave periods of 1 year or slightly less, wavelengths of 500-800 km, phase speeds of 2-5 cm/sec, growth periods of several months, and LSODs larger than 500 km. In the zonal case, none of the modes has radiating waves within the above ranges. Hence, the zonal case is not satisfactory in explaining the observed spatial and temporal characteristics. For comparison purposes, a wave with values of T, L, C, T_g, and LSOD closest to the observed dominant ranges in each mode is listed in Table 4.6 and represented in Figs. 4.3c, 4.4a, 4.4c.

b. Case II (30^o flow with a strong vertical shear)

In this case the mean flow is the same as that in case I (zonal flow) except for the new flow orientation of 30^o (Table 4.1). This approximates the KEC in the western boundary region. There exist six modes of the solution (Fig. 4.5) in contrast to the five modes found in the zonal case. Also, the range of wavelengths covered by each mode is broader in this case than in the zonal case. Frequency, growth rate, phase speed and imaginary phase speed are generally higher than in the zonal case, and four out of the six modes contain radiating waves (Table 4.3). Mode 2 exhibits only radiating instability, and modes 5 and

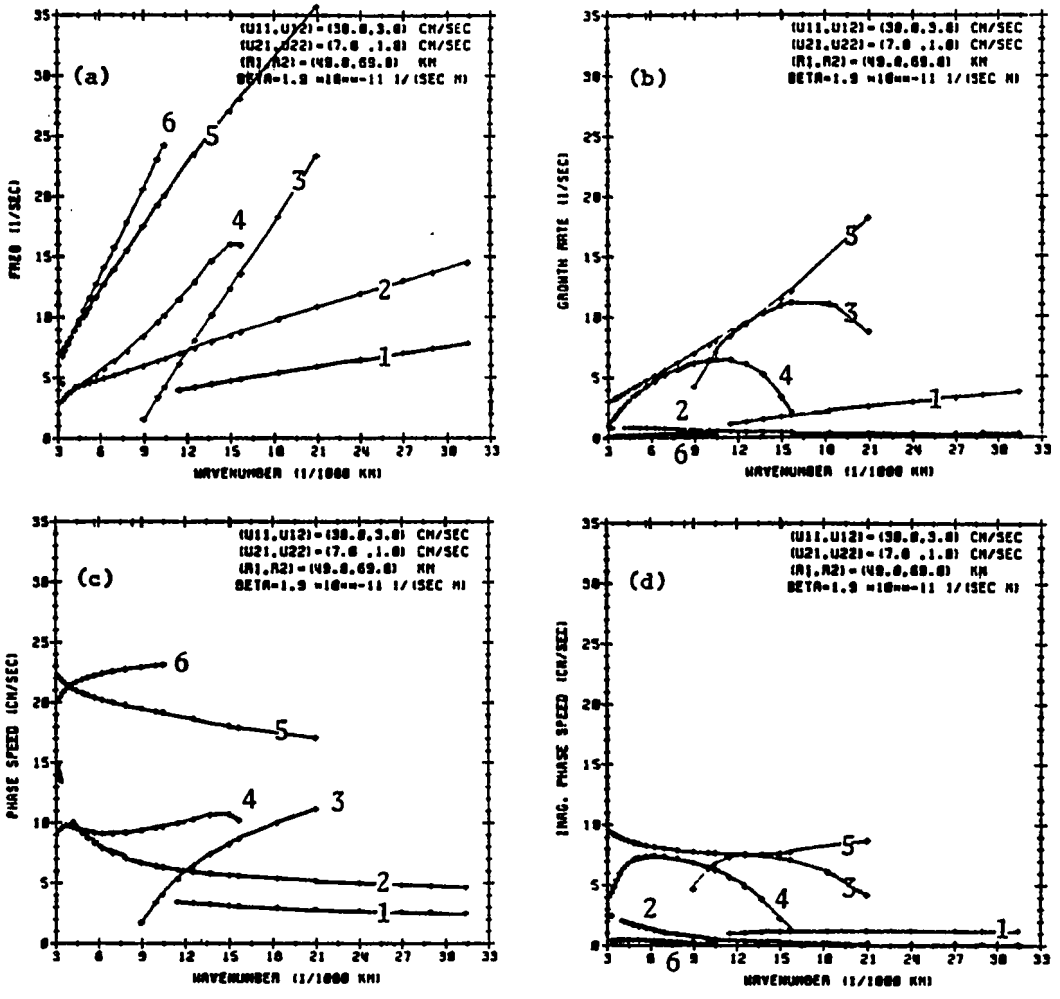

Figure 4.5 (a) Frequency [10^{-7} sec^{-1}], (b) growth rate [10^{-7} sec^{-1}], (c) phase speed [cm/sec], and (d) imaginary phase speed [cm/sec] as a function of wavenumber [10^{-8} cm^{-1}] for case II.

Table 4.3 Ranges of period (T), wavelength (L), phase speed (C), growth period (T_g), and imaginary phase speed (C_i) of (a) all unstable waves and of (b) radiating unstable waves present in each mode for case II. The underline in T_g indicates a unit of [years].

		mode 1	mode 2	mode 3	mode 4	mode 5	mode 6
solution range	T [days]	91-182	50-243	31-481	42-485	21-104	30-107
	L [km]	200-550	200-2000	300-700	400-2000	500-2000	700-1000
	C [cm/sec]	3-4	5-15	2-11	9-11	17-22	20-23
	T_g [days] [years]	191-661	2.5-14	65-173	112-606	40-242	242-727
	C_i [cm/sec]	1	<0.5	4-7	1-7	8-10	<0.5
radiation range	T [days]	150-182	50-243	220-480	145-242		
	L [km]	400-500	200-2000	630-700	1200-2000		
	C [cm/sec]	3-4	5-15	2	8-10	only Trapped waves	only Trapped waves
	T_g [days] [years]	416-727	2.5-14	110-175	173-606		
	C_i [cm/sec]	1	<0.5	5-6	4-7		

6 exhibit only trapped instability. Both trapped modes have high phase speeds, but the phase speeds are always less than the maximum flow speed as discussed in Section 2. In modes 1, 3, and 4, the unstable waves with short period and wavelength are trapped. In general, the growth rates are larger than in the zonal case (the lower bound of the complex phase speed is in nonzonal flows). A very low growth rate, however, does not guarantee radiation, as in the zonal case.

The structure of the eigenfunctions in mode 1 show that LSODs of all radiating waves are longer than 1200 km and that the amplitudes in both layers are nearly equal (Fig. 4.6). In mode 2, LSODs decrease from >2000 km at a wavelength of 200 km to a nearly zero (i.e., almost totally trapped) at a wavelength of 800 km (Figs. 4.7a-b). The radiating waves in this range are bottom-intensified. At wavelengths longer than 900 km, the LSOD increases and the waves become more surface-intensified with increasing wavelength (Fig. 4.7c). The LSODs in mode 3 are 800-1000 km, and the waves have no intensification in any particular layer (Fig. 4.8a). In mode 4, the radiating waves have LSODs longer than 1000 km, increasing with wavelength, and the waves have similar amplitudes in both layers (Figs. 4.8b-c).

In this flow regime, wave periods, wavelengths, phase speeds, and growth periods of the radiating waves are

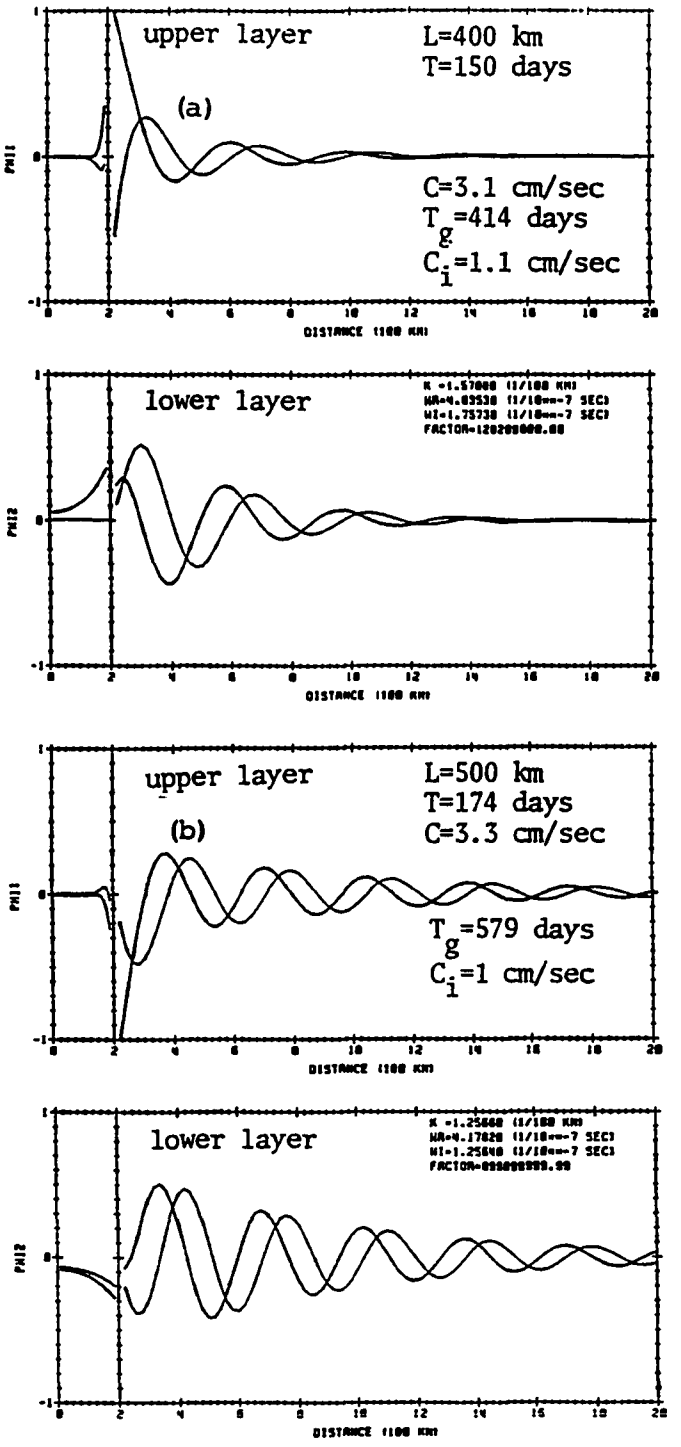

Figure 4.6 Structure of eigenfunctions in the cross-flow direction for mode 1 in case II.

Figure 4.7 Structure of eigenfunctions in the cross-flow direction for mode 2 in case II.

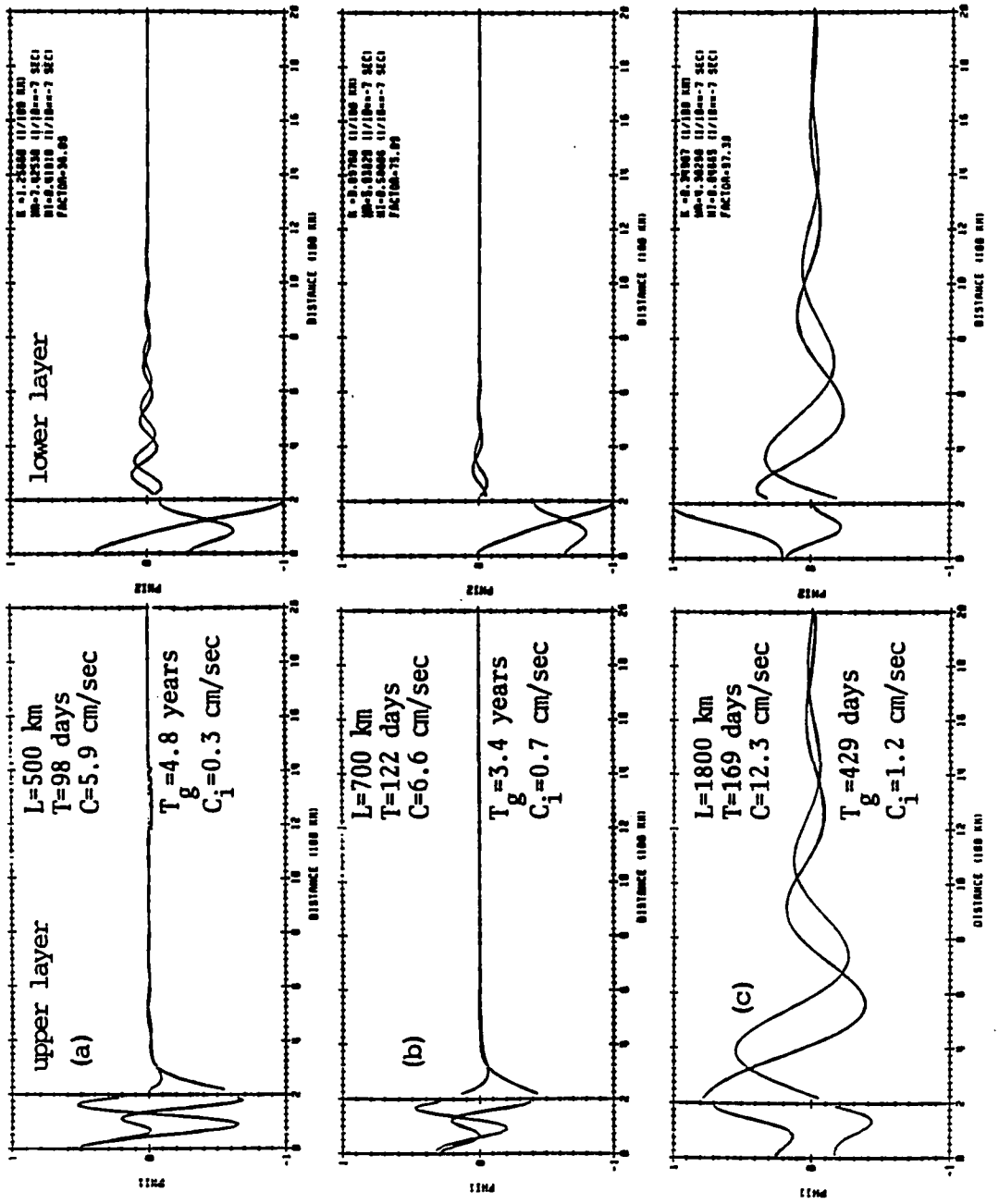

Figure 4.8 Structure of eigenfunctions in the cross-flow direction for (a) mode 3, (b) mode 4, and (c) mode 4 in case II.

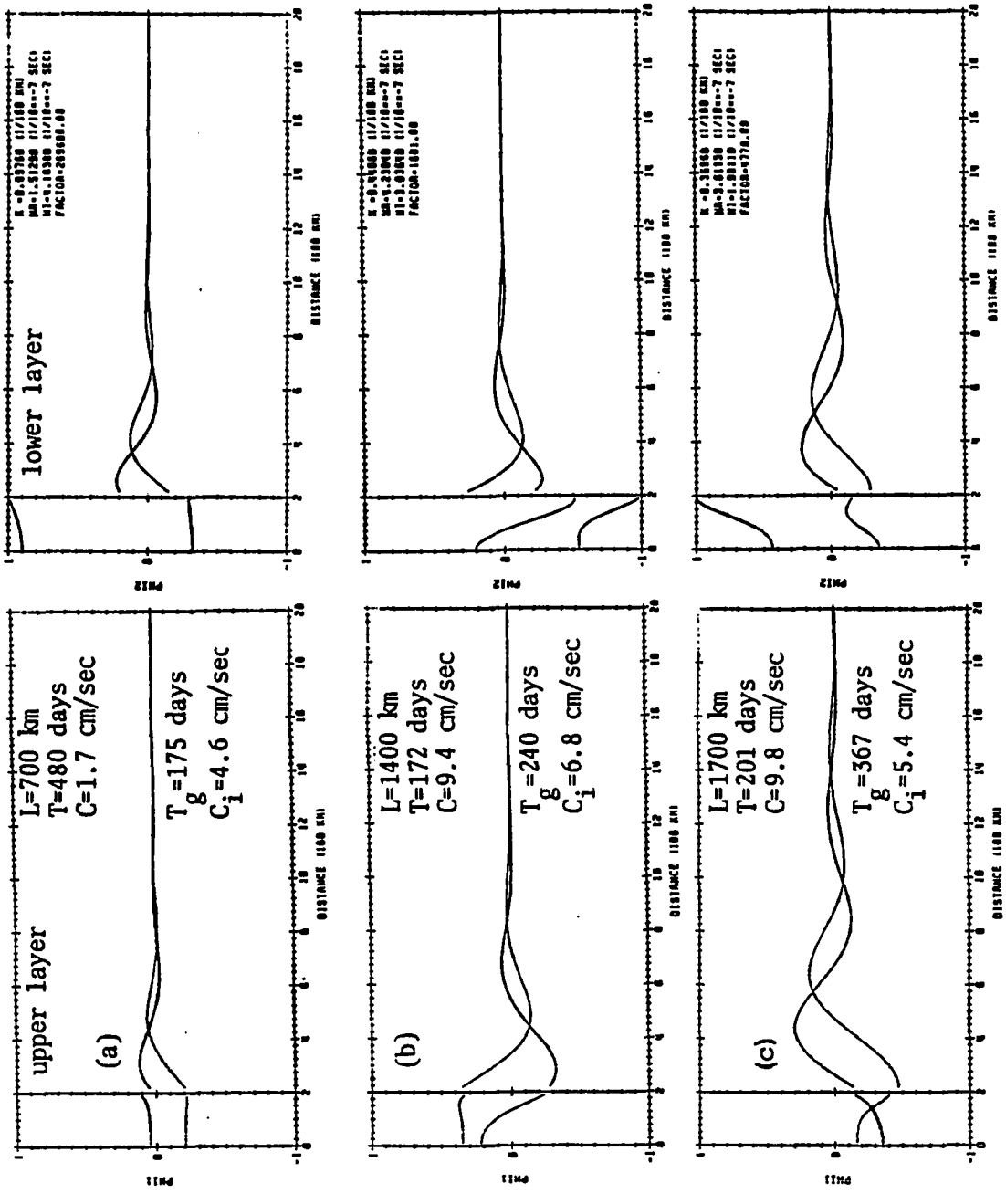

closer to the observed ranges than in the zonal case. Also, the LSODs are longer, and the waves are less bottom-intensified than in the zonal case. Table 4.6 lists the values of T, L, C, T_g, LSOD, and the type of intensification of solutions that came close to the observed ranges for each mode. See also Figs. 4.6b, 4.7a, 4.8a, and 4.8b. We have tacitly assumed that only one mode present in the real ocean. The table shows that the waves of modes 1 and 3 explain the observed spatial and temporal characteristics better than those in the zonal case.

c. Case III (30^{o} flow with a weak vertical shear)

The mean flow in this case is the same as that in case II but the flow speeds have been changed to U_{I1}=15, U_{I2}=1, U_{III}=3 and U_{II2}=0 cm/sec. This approximates the KEC at 165^{o}E. The solution has 6 modes as in case II, but the ranges of wavenumbers and periods exhibited by each mode are generally narrower (Fig. 4.9). In modes 1 and 2 the solutions exist over two disjoint ranges in the frequency-wavenumber domain. The frequency, growth rate, phase speed, and imaginary phase speed of unstable waves in this case are nearly half the magnitude as those in case II. In this case, four out of the six modes contain radiating waves. Mode 2 exhibits only radiating instability, and modes 3 and 6 exhibit only trapped waves

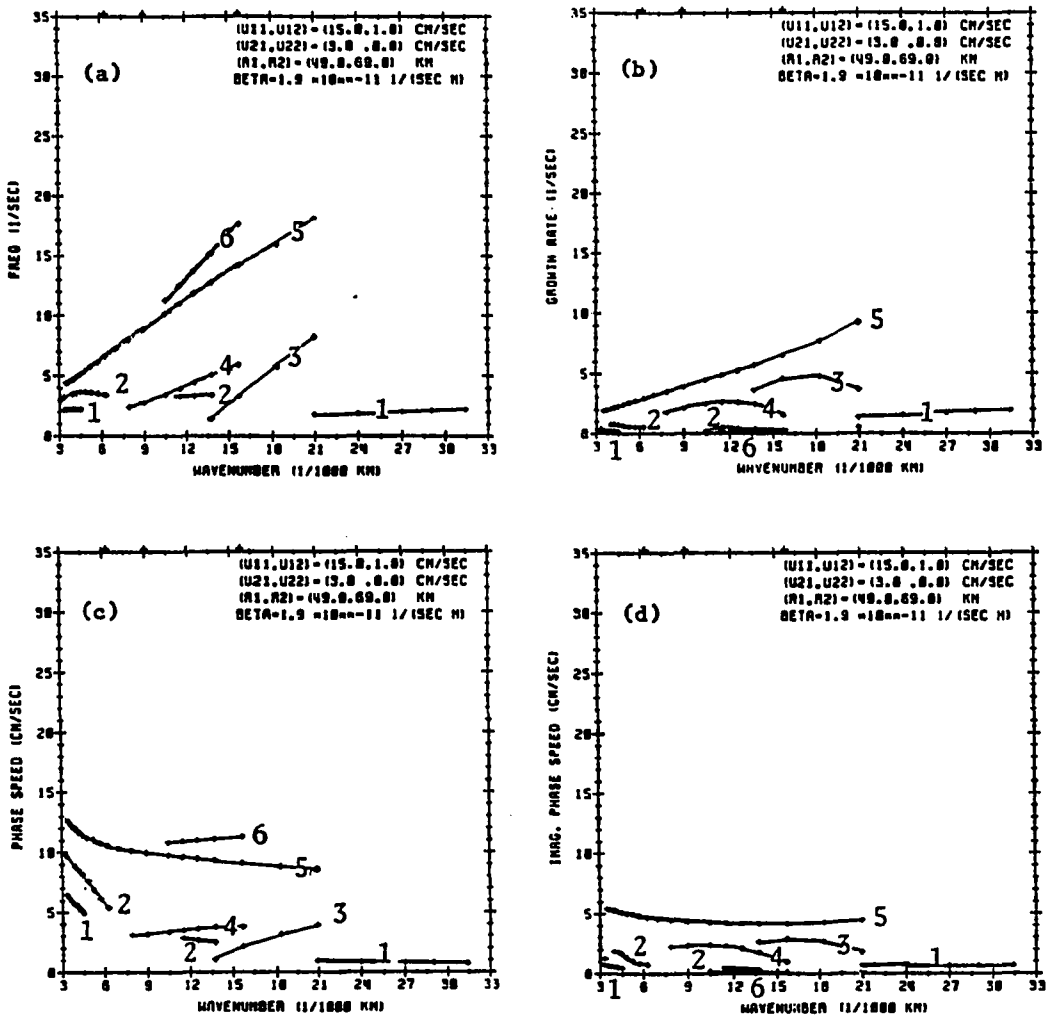

Figure 4.9 (a) Frequency [10^{-7} sec^{-1}], (b) growth rate [10^{-7} sec^{-1}], (c) phase speed [cm/sec], and (d) imaginary phase speed [cm/sec] as a function of wavenumber [10^{-8} cm^{-1}] for case III.

(Table 4.4). In modes 1, 4, and 5, the unstable waves with short period and wavelength are trapped as in the previous cases. In general, the radiating waves have lower growth rates than in the zonal case, indicating a higher growth rate associated with larger shear.

The eigenfunctions in mode 1 show LSODs of 600-900 km with slight bottom-intensification at wavelengths of 300 km and shorter (Figs. 4.10a-b). The LSODs are very long and the waves are surface-intensified at wavelengths longer than 1600 km (Fig. 4.10c). In mode 2, the LSODs decrease with wavelength and the waves are bottom-intensified at wavelengths of 450-550 km (Figs. 11a-b). At wavelengths longer than 1000 km, the LSODs become longer and the waves become more surface-intensified as the wavelength increases (Fig. 4.11c). In mode 4, only one solution among those investigated is of the radiating type, and the wave has LSODs of 700 km with similar amplitudes in both layers. The LSODs in mode 5 are longer than 900 km, increasing with wavelength and the waves have similar amplitudes in both layers (Figs. 4.12b-c).

Drawing from the findings of Chapter II, one would expect that a weaker current shear (characteristic of the interior North Pacific) would result in unstable waves of shorter wavelengths, lower phase speeds, lower growth rates, and longer periods than with stronger current shear (characteristic of the western boundary). It is also found

Table 4.4 Ranges of period (T), wavelength (L), phase speed (C), growth period (T_g), and imaginary phase speed (C_i) of (a) all unstable waves and of (b) radiating unstable waves present in each mode for case III. The underline in T_g indicates a unit of [years].

		mode 1	mode 2	mode 3	mode 4	mode 5	mode 6
solution range	T [days]	364-406; 333	217-226; 199-227	112-727	121-316	41-165	41-64
	L [km]	200-300; 1400-2000	450-550; 1000-2000	300-450	400-800	300-2000	400-600
	C [cm/sec]	1; 5-7	2-3; 5-10	1-3	3-4	9-13	7-11
	T_g [days] [years]	364-559; 8.1	5.1-6.7; 2.5-5.1	152-197	280-13.5	78-364	10.1
	C_i [cm/sec]	<1; <1	<0.5; 1-2	2-3	4-5	1-2	0.2
radiation range	T [days]	333	217-226; 199-227	only Trapped waves	308	150-165	only Trapped waves
	L [km]	1400-2000	450-550; 1000-2000		800	>1500	
	C [cm/sec]	5-7	2-3; 5-10		3	12-13	
	T_g [days] [years]	8.1	5.1-6.7; 2.5-5.1		433	34-409	
	C_i [cm/sec]	<1	<0.5 1-2		2	5	

Figure 4.10 Structure of eigenfunctions in the cross-flow direction for mode 1 in case III.

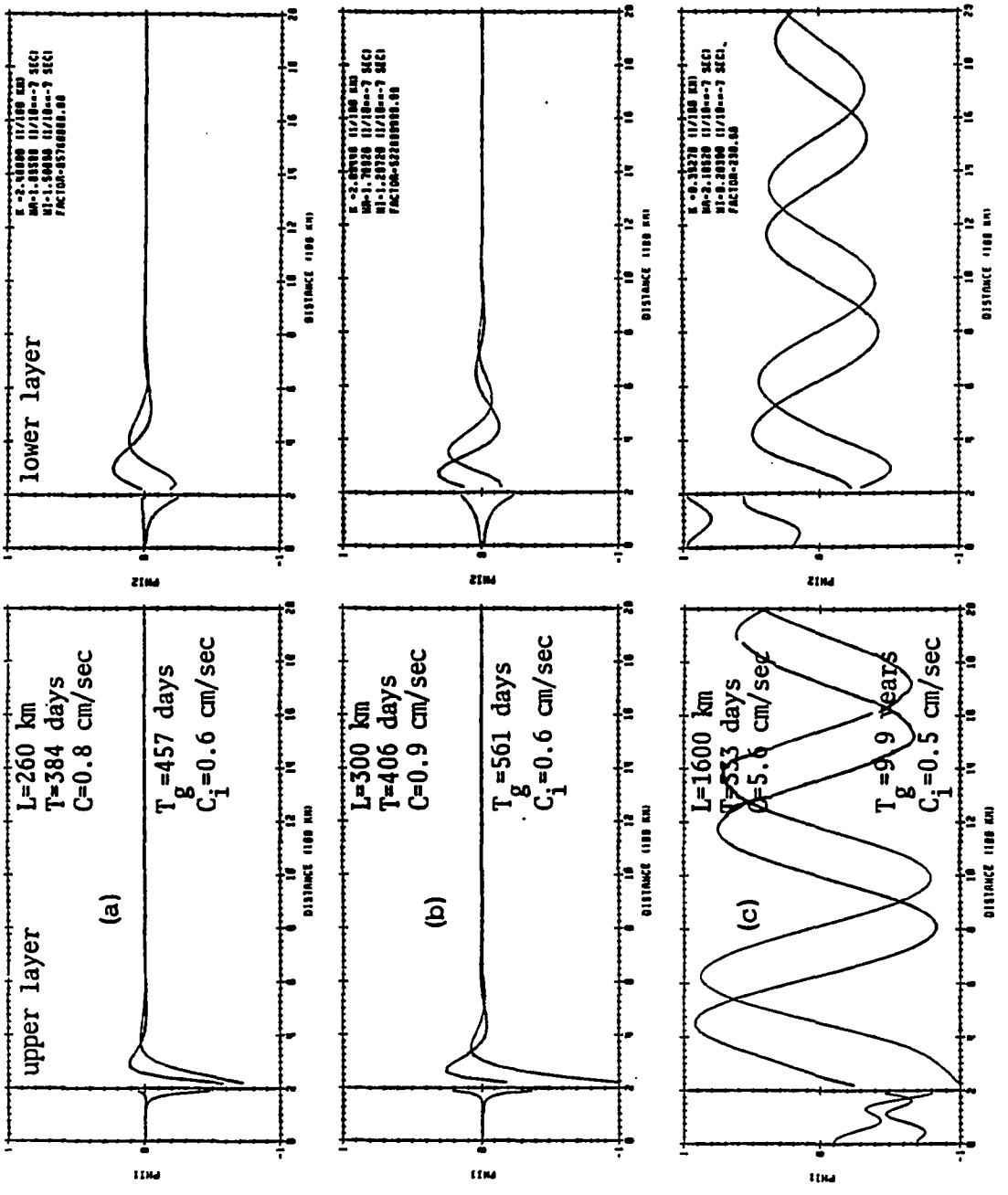

Figure 4.11 Structure of eigenfunctions in the cross-flow direction for mode 2 in case III.

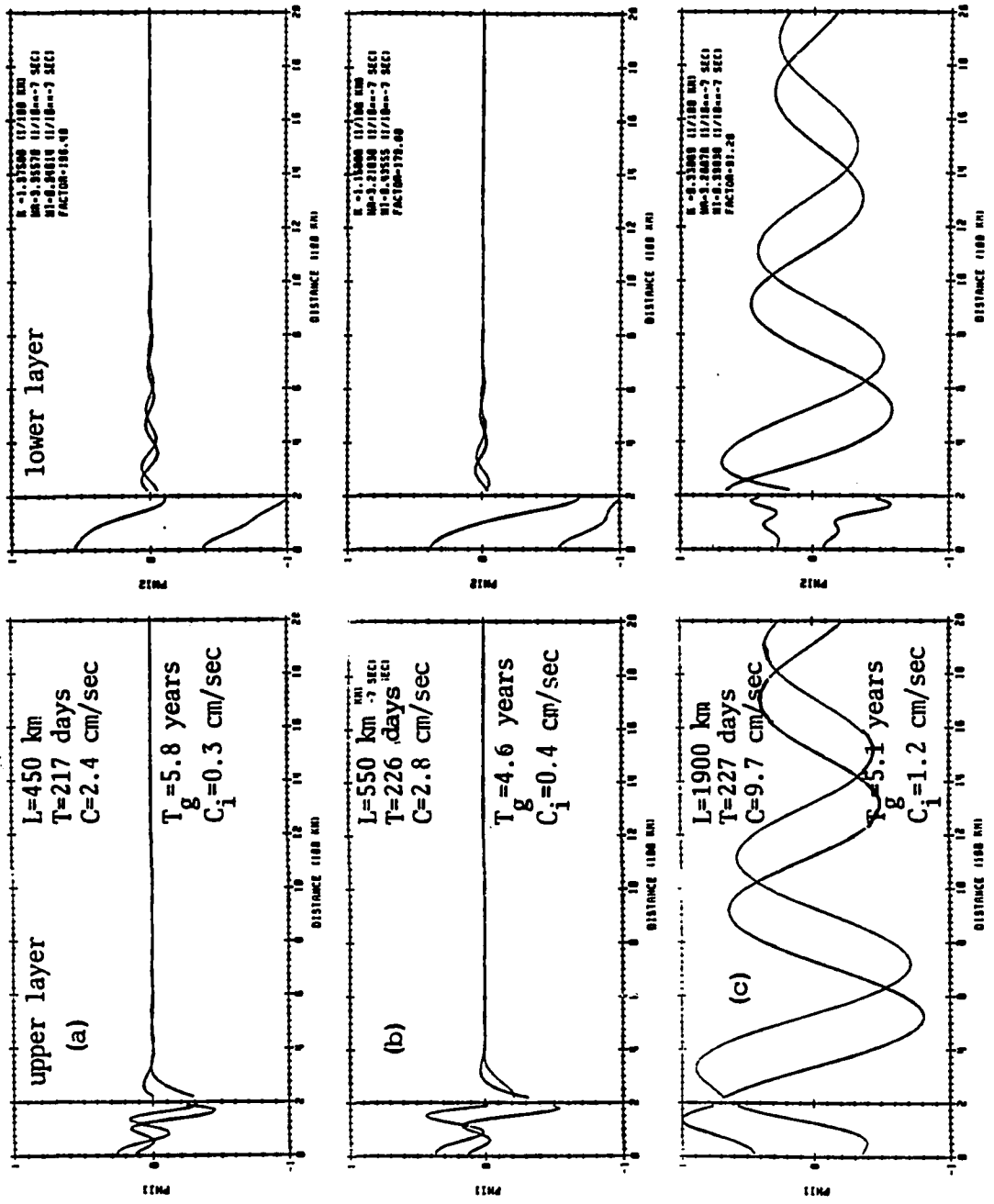

Figure 4.12 Structure of eigenfunctions in the cross-flow direction for (a) mode 4, (b) mode 5, and (c) mode 5 in case III.

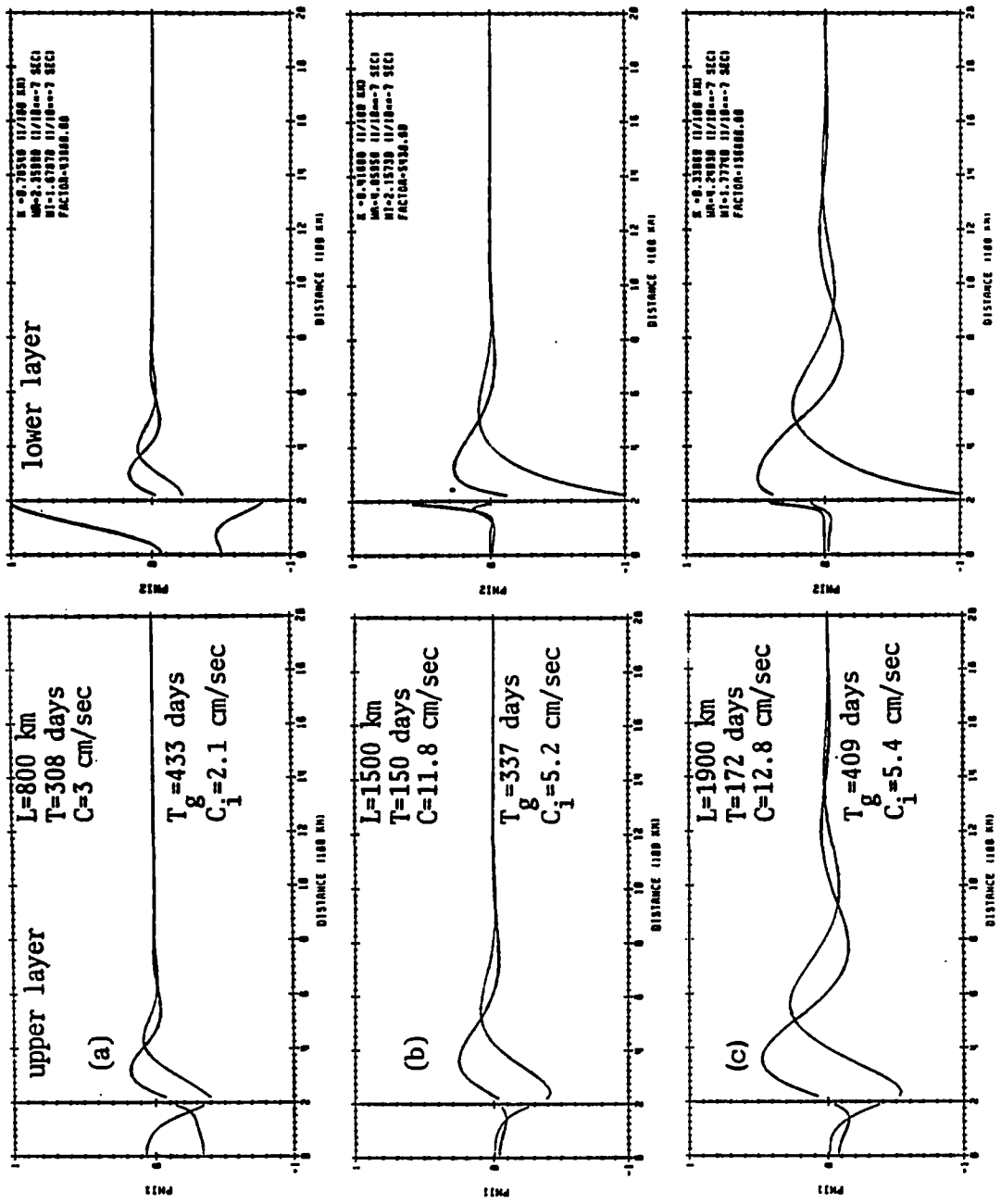

that the observed length scales are smaller and the observed time scales are larger in the interior region than in the western boundary. The radiating unstable waves generally manifest this behaviour, and in the observed ranges of time and length scales the theory predicts shorter LSOD and greater bottom-intensification in the interior region. In general, it seems that a stronger shear flow has a greater tendency towards radiating instability. Radiating unstable waves of each mode with values of T, L, C, T_g, LSOD, and the type of intensification closest to the observed dominant ranges are listed in Table 4.6 and also displayed in Figs. 4.10b, 4.11a, 4.12a, and 4.12b.

d. Case IV (60^o flow with a strong vertical shear)

The mean flow is the same as that in case II except for the new flow orientation of 60^o. A current with the flow orientation and strong vertical shear models the Kuroshio Current. One should, however, note that caes IV is not a suitable approximation for the flow structure that we used, since the Kuroshio Current is a flow along the boundary. No solution exists at wavelengths shorter than 300 km. At longer wavelengths there are six modes of the solution, as in the other nonzonal cases (Fig. 4.13). Frequencies, phase speeds, growth rates, and imaginary

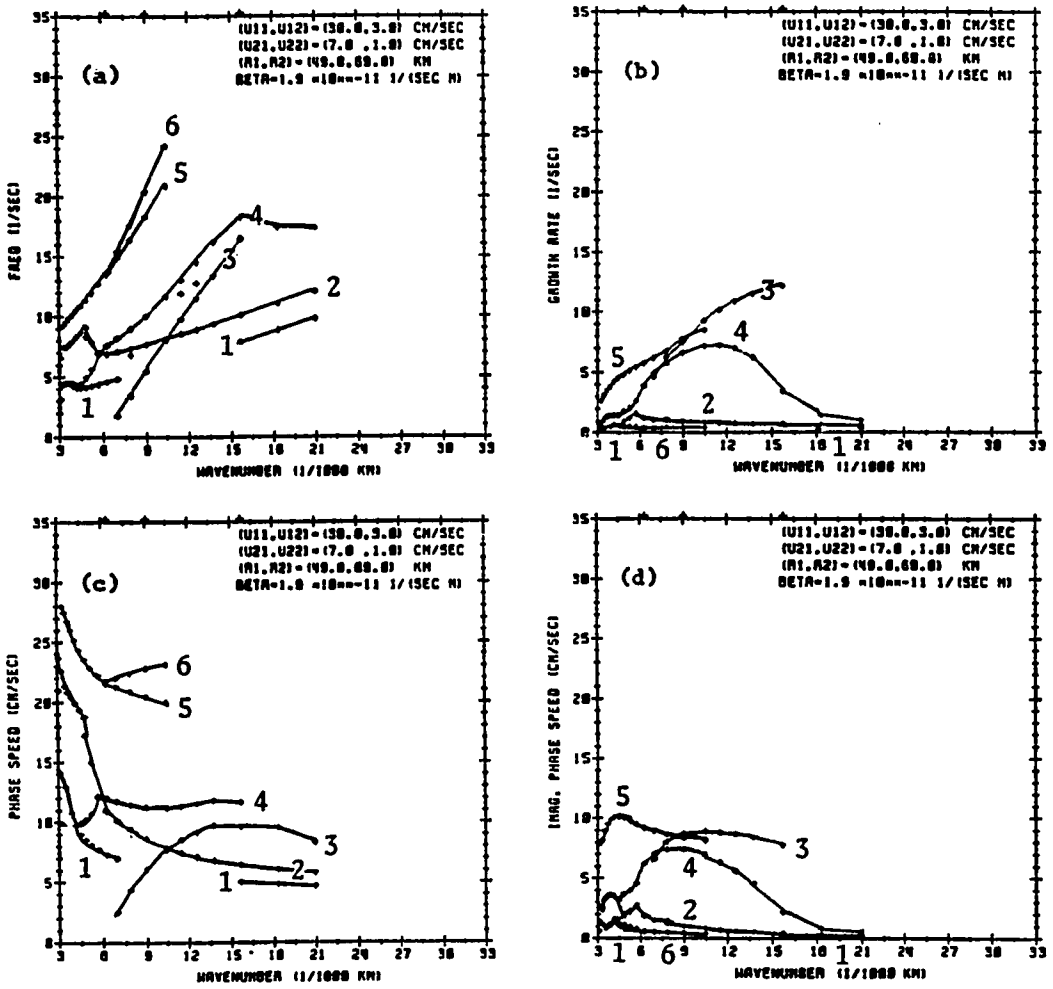

Figure 4.13 (a) Frequency [10^{-7} sec^{-1}], (b) growth rate [10^{-7} sec^{-1}], (c) phase speed [cm/sec], and (d) imaginary phase speed [cm/sec] as a function of wavenumber [10^{-8} cm^{-1}] for case IV.

phase speeds are higher than in case II (strong vertical shear; 30^{o} orientation). Five out of the six modes contain radiating waves, an increase in the number of radiating modes with a more meridional flow orientation (Table 4.5). Modes 1 and 2 exhibit exclusively radiating instability. The growth rates of these modes are low, as in the other cases. In modes 3, 4, and 5, the unstable waves with short wavelength and period are trapped. Modes 5 and 6 have high phase speed but the maximum phase speed is smaller than the maximum flow speed as determined by (4-17). The unstable waves in mode 5 radiate, despite their high growth rates; this is contrary to the more typical findings, where unstable waves with high growth rates were trapped. The mode 5 waves in case II, which occurred in the same ranges of periods and wavelengths as the mode 5 waves in this case, were exclusively trapped waves. Finally, the unstable waves in mode 6 are all trapped waves despite their very low growth rates. This was also found in case II and, again, is contrary to the more typical findings.

The eigenfunctions in mode 1 show very long LSODs at wavelengths shorter than 400 km, and the waves become less bottom-intensified as the wavelength approaches 400 km (Figs. 4.14a-b). At wavelengths longer than 900 km, the waves become strongly surface-intensified with very long LSODs (Fig. 4.14c). In mode 2, the LSODs at wavelengths of

Table 4.5 Ranges of period (T), wavelength (L), phase speed (C), growth period (T_g), and imaginary phase speed (C_i) of (a) all unstable waves and of (b) radiating unstable waves present in each mode for case IV. The underline in T_g indicates a unit of [years].

		mode 1	mode 2	mode 3	mode 4	mode 5	mode 6
solution range	T [days]	74-93; 151-182	61-104	44-428	40-164	35-79	35-54
	L [km]	300-400; 900-2000	300-2000	400-900	300-1400	600-2000	600-1000
	C [cm/sec]	5; 7-14	6-24	3-11	10-12	20-28	22-23
	T_g [days] [years]	3.4-6.7; 3.4-6.7	1.3-4	60-162	100-727	80-260	6.7
	C_i [cm/sec]	0.1; 1-2	0.2-4	6-9	0.5-7	8-10	0.2-2
radiation range	T [days]	74-93; 151-182	61-104	215-428	89-164	57-79	
	L [km]	300-400; 900-2000	300-2000	800-900	900-1400	1100-2000	
	C [cm/sec]	5; 7-14	6-24	3-4	10-12	22-28	only Trapped waves
	T_g [days] [years]	3.4-6.7; 3.4-6.7	1.3-4	116-159	149-502	134-260	
	C_i [cm/sec]	0.1; 1-2	0.2-4	7-8	3-7	8-9	

Figure 4.14 Structure of eigenfunctions in the cross-flow direction for mode 1 in case IV.

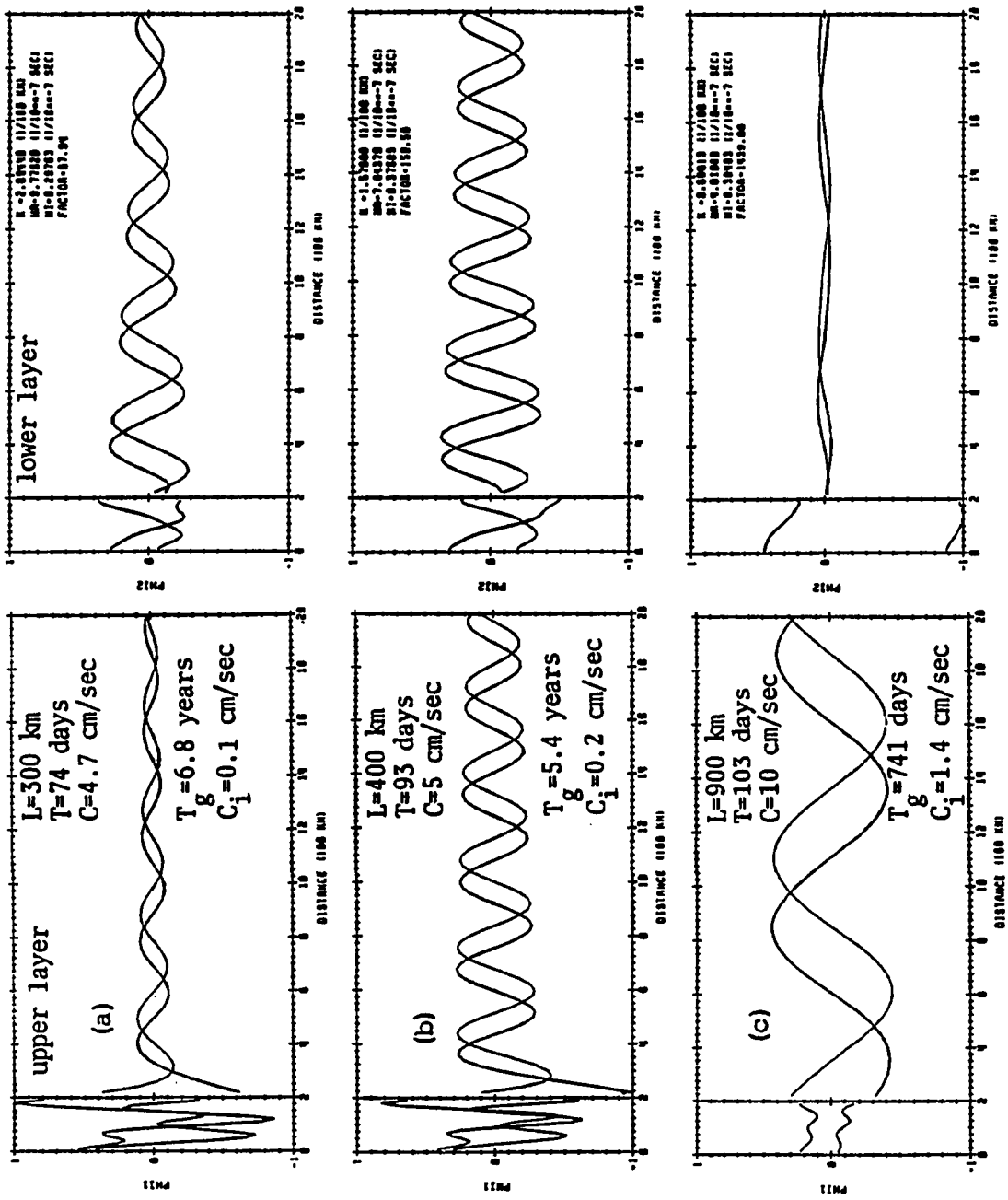

300-600 km decrease and the waves become more surface-intensified as the wavelength increases (Fig. 4.15a). The LSODs are shortest at a wavelength of 600 km. At wavelengths longer than 700 km, the LSOD increases rapidly with wavelength and the waves rapidly become surface-intensified (Figs. 4.15b-c). In mode 3, the waves at wavelengths of 800-900 km have nearly equal amplitudes in both layers with LSODs longer than 1500 km (Figs. 4.16a-b). For mode 4, LSODs are longer than 1400 km, increasing with wavelength, and the waves become more surface-intensified as the wavelength increases (Fig. 4.17). The waves in mode 5 show nearly equal amplitudes in both layers with LSODs longer than 1000 km (Fig. 4.18).

In general, radiating waves in case IV have longer wavelengths, shorter periods, higher phase speeds, higher growth rates, longer LSODs and more surface-intensification than those in any other cases. These characteristics together with those in the 30^{o} flow cases concur with the observed trend of decreasing length scales and increasing time scales towards the east. As was done previously, unstable waves of each mode closest to the observed values of T, L, C, T_g and LSOD, and the type of intensification are listed in Table 4.6 and also shown in Figs. 4.14c, 4.15b, 4.16a, 4.17, and 4.18. Comparing only one mode at a time (i.e., not considering possible superpositions of the modes), it was found that mode 3 is in better agreement

Figure 4.15 Structure of eigenfunctions in the cross-flow direction for mode 2 in case IV.

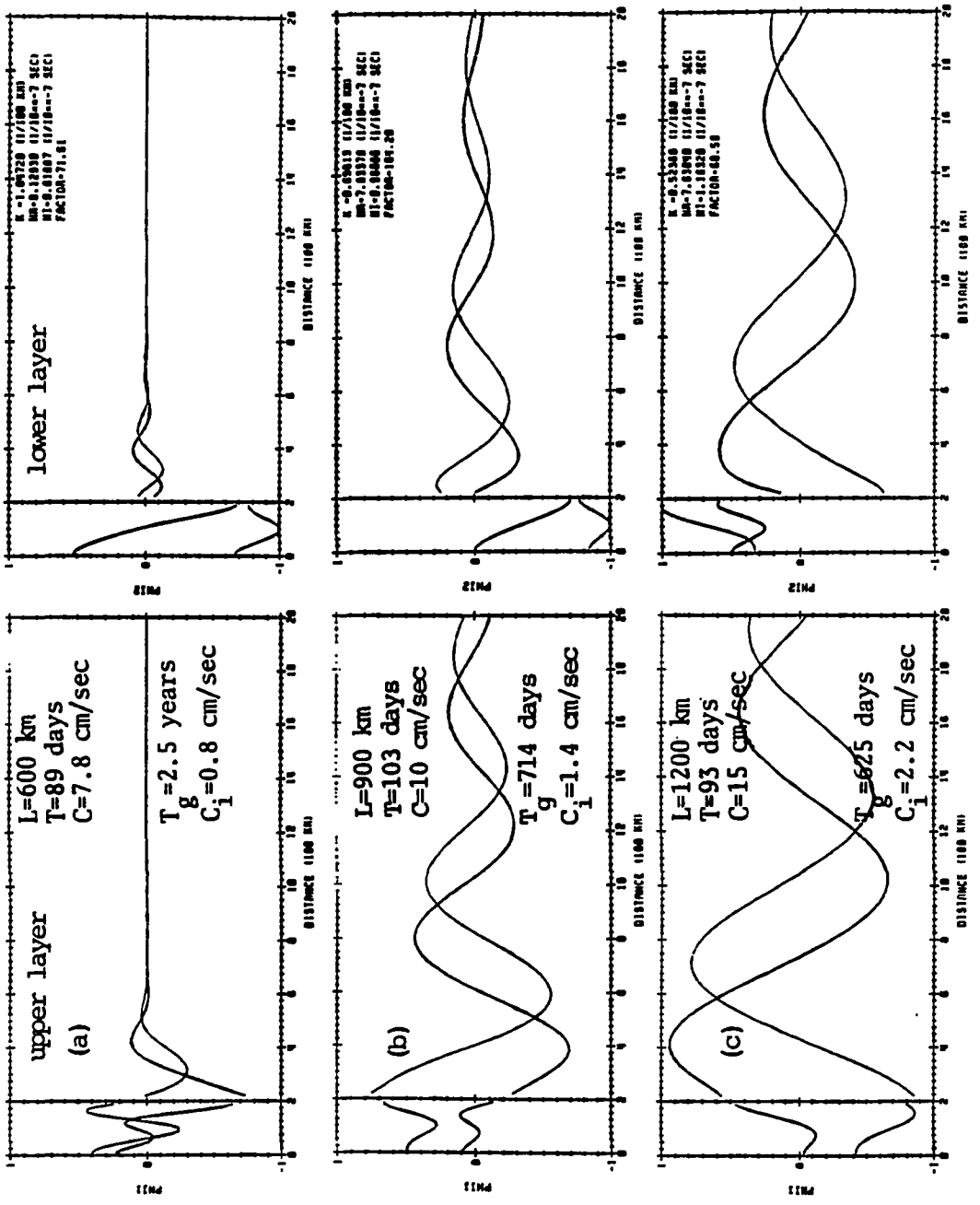

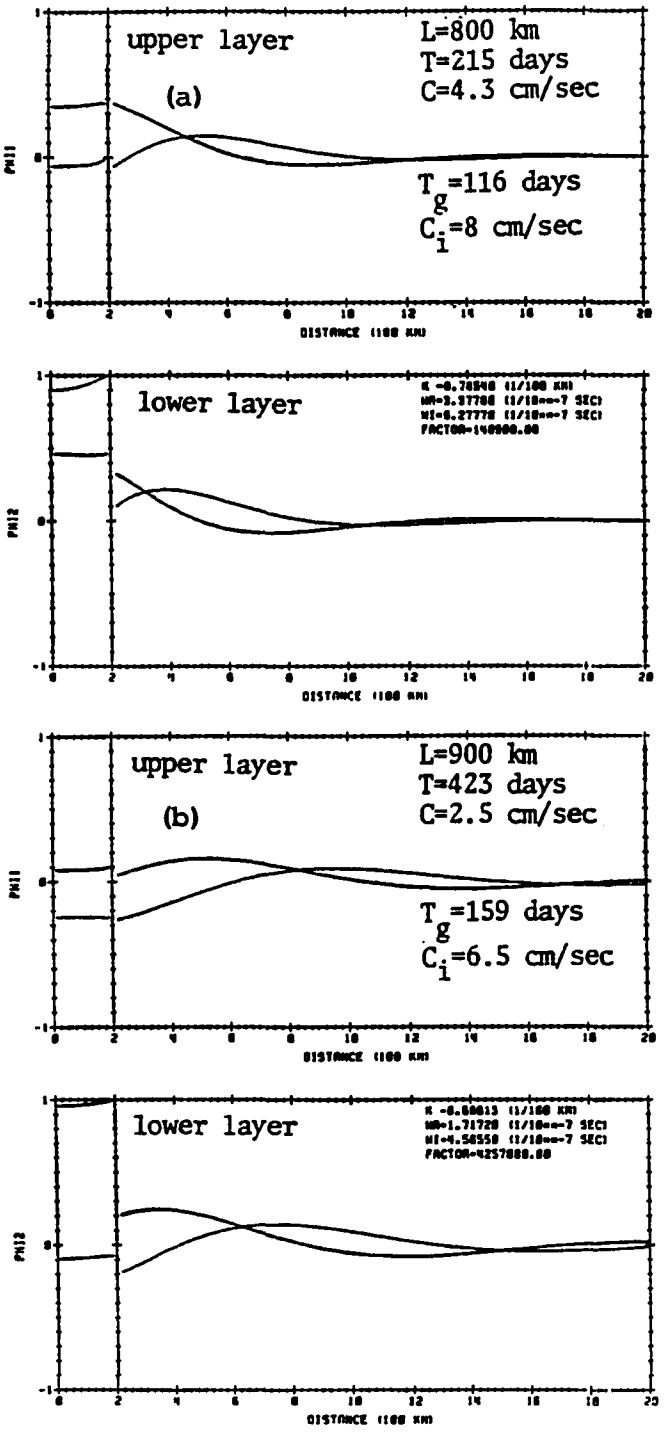

Figure 4.16 Structure of eigenfunctions in the cross-flow direction for mode 3 in case IV.

Figure 4.17 Structure of eigenfunctions in the cross-flow direction for mode 4 in case IV.

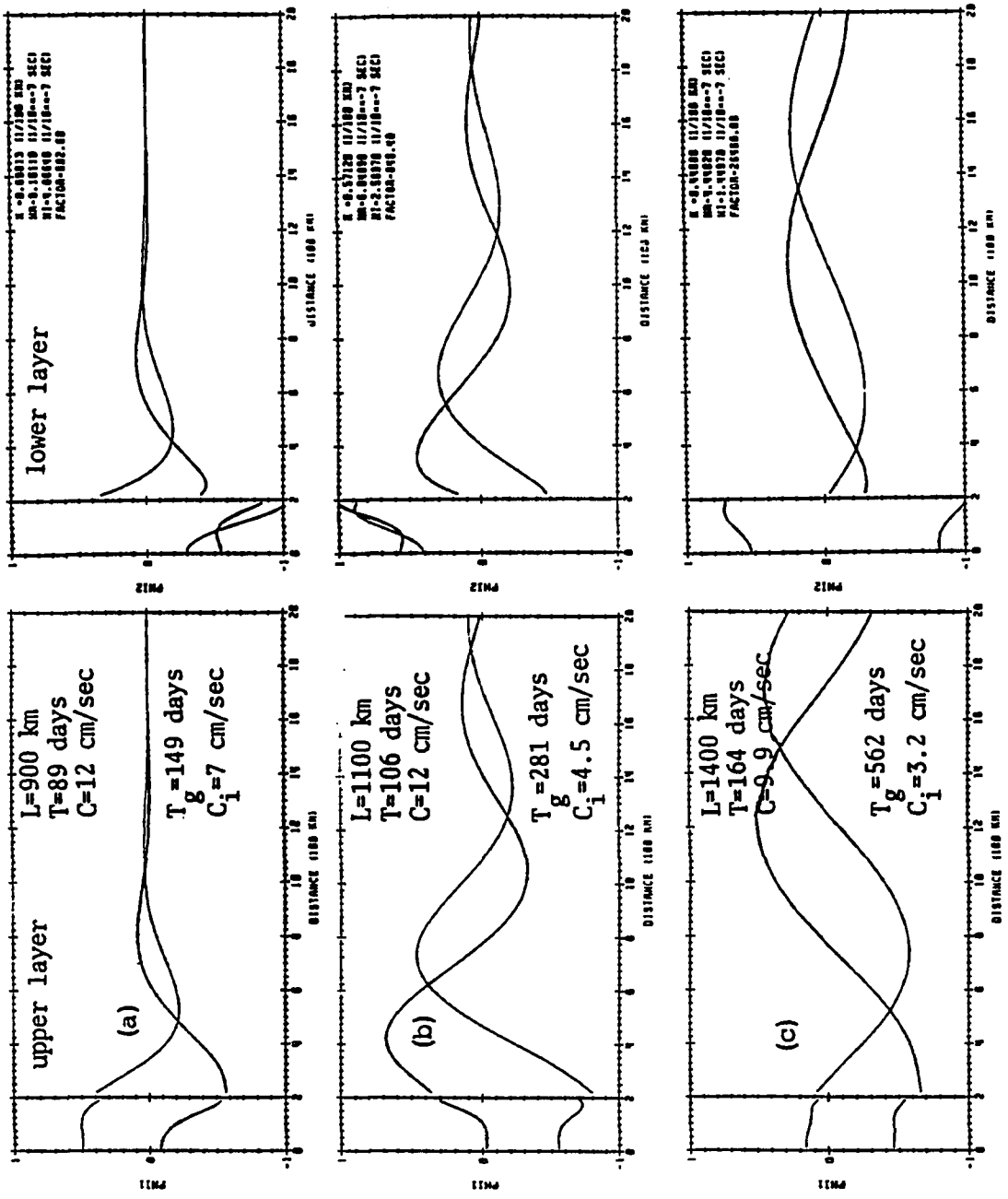

Figure 4.18 Structure of eigenfunctions in the cross-flow direction for mode 5 in case IV.

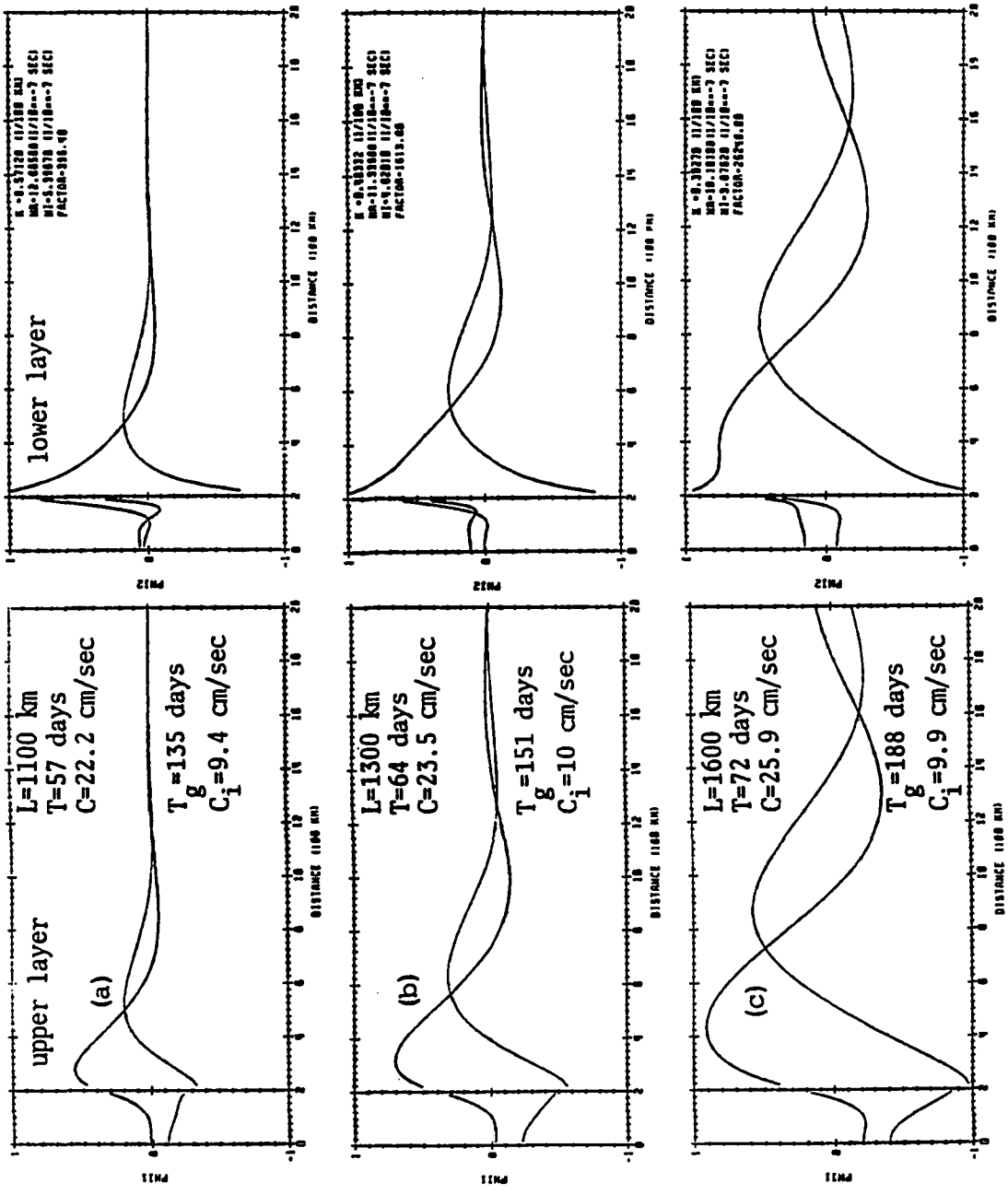

with the observation near the western boundary than the other modes.

5. Summary and conclusions

There are five unstable modes of the solution in the zonal case and six modes in the nonzonal cases. Frequencies, phase speeds, growth rates and imaginary phase speeds as functions of wavenumber have similar shapes in all cases. The solution exists over broad ranges in the frequency-wavenumber domain in the three cases with the strong vertical shear, but it exists over narrow and divided ranges in the case with the weak shear. Over the solution range (radiating plus trapped waves), frequencies, phase speeds, growth rates, and imaginary phase speeds generally increase with increasing vertical shear at a fixed flow orientation and increase as the flow orientation changes from zonal to 60^{o} at a fixed vertical shear.

In general, unstable waves with short wavelengths and short periods, and those with high phase speeds are trapped. In the nonzonal cases investigated, waves with low growth rate do not necessarily radiate. In the zonal case, however, waves with low growth rates radiated. The number of modes which contain radiating waves increases as the flow orientation increases (three, four, and five in the zonal, 30^{o}, and 60^{o} flow cases, respectively). In

the radiating ranges, frequencies, growth rates, and phase speeds also increase with increasing vertical shear and angle of orientation. The length scales of decay increase as the flow orientation changes from zonal to 60° at a fixed vertical shear, and as the vertical shear increases at a fixed flow orientation. Concurrently, wave amplitude intensification changes with vertical shear and flow orientation. In general, bottom-intensification occurs with zonal flow. Roughly equal amplitudes in both layers are found with 30° flow, and surface-intensification developes as the flow orientation changes to 60° at a fixed vertical shear. Also, the waves are more surface-intensified when the vertical shear is stronger at a fixed orientation.

In each mode, radiating waves in the nonzonal cases show spatial and temporal characteristics closer to the observed dominant ranges than those in the zonal case. This is clearly seen by comparing the radiating waves summarized in Table 4.6. For the flow condition near the western boundary (approximated by the 60° flow orientation), the radiating waves in modes 2, 3 and 4 (especially mode 3) show fair agreement with the observed dominant ranges. In the case of the 30° flow with the strong shear, modes 1 and 3 appear to be within the observed dominant ranges. Radiation in modes 1 and 4 of the 30° flow case with the weak shear is in less

Table 4.6 Summary of wavelengths, periods, phase speeds, growth periods, imaginary phase speeds, length scales of decay, and type of intensification of radiating waves closest to the observed dominant ranges. The waves listed here represent each radiating mode. SFC and BTM indicate surface- and bottom-intensification, UP and LO indicate upper and lower layers, and SFC&BTM indicates similar amplitudes in both layers.

	Case	L [km]	T [days]	C [cm/sec]	T_g [days] or [years]	C_i [cm/sec]	LSOD [km]	Type of Intensification
mode 1	I	400	90	5	139	0.001	2000	BTM
	II	500	174	3.3	579	1	2000	SFC&BTM
	III	300	406	0.9	559	0.6	500(UP) 900(LO)	BTM
	IV	900	151	6.9	6.6	0.4	2000	SFC
mode 2	I	500	224	2.6	410	1.4	800(LO)	BTM
	II	500	98	5.9	4.1	0.3	1000	BTM
	III	450	217	2.4	5.8	0.3	800(LO)	BTM
	IV	900	103	10	714	1.4	2000	SFC
mode 3	I	700	814	1	580	1.4	500(UP) 700(LO)	BTM
	II	600-700	220-481	1.8-2.4	110-173	4.8-6.4	1000-1200	SFC&BTM
	IV	800	215	4.3	116	8	1500	SFC&BTM
mode 4	II	1200	145	9	173	7.3	1000	SFC&BTM
	III	800	308	3	433	2.2	700	SFC&BTM
	IV	900	89	12	149	7	1400	SFC
mode 5	III	1500	150	11.6	337	5.2	700	SFC&BTM
	IV	1100	57	22	134	9.4	1000	SFC&BTM

agreement with the observations. In the zonal case, none of the modes have the radiating waves closely resembling the observetions. Therefore, the zonal flow is regarded as the least appropriate model flow to explain the observed temperature fluctuations. In the mid-latitude western North Pacific, radiating instability based on a nonzonal mean current appears to be a more realistic process than that based on a zonal flow for the fairly energetic internal temperature fluctuations observed away from the main axis of the KEC.

Appendix Dispersion relation

$$\omega^4+\alpha\omega^3+\beta\omega^2+\gamma\omega+\delta=0$$

where

$$\alpha=-[2Q(U_{I1}+U_{I2})+2R(U_{I2}+U_{I1})+2S(U_{I1}+U_{I2})+T(U_{I1}+U_{I2}+U_{I1}+U_{I2})+2V(U_{I1}+U_{I2})]k/(Q+R+S+T+V)$$

$$\beta=\{Q[(U_{I1}+U_{I2})^2+2U_{I1}U_{I2}]+R[(U_{I2}+U_{I1})^2+2U_{I2}U_{I1}]+S[(U_{I1}+U_{I2})^2+2U_{I1}U_{I2}]+T[U_{I1}U_{I2}+(U_{I1}+U_{I2})(U_{I1}+U_{I2})+U_{I1}U_{I2}]+V[(U_{I1}+U_{I2})^2+2U_{I1}U_{I2}]\}k^2/(Q+R+S+T+V)$$

$$\gamma=-\{2QU_{I1}U_{I2}(U_{I1}+U_{I2})+2RU_{I2}U_{I1}(U_{I2}+U_{I1})+2SU_{I1}U_{I2}(U_{I1}+U_{I2})+T[U_{I1}U_{I2}(U_{I1}+U_{I2})+U_{I1}U_{I2}(U_{I1}+U_{I2})]+2VU_{I1}U_{I2}(U_{I1}+U_{I2})\}k^3/(Q+R+S+T+V)$$

$$\delta=[QU_{I1}^2U_{I2}^2+RU_{I2}^2+U_{I1}^2+SU_{I1}^2U_{I2}^2+TU_{I1}U_{I2}U_{I1}U_{I2}+VU_{I1}^2U_{I2}^2]k^4/(Q+R+S+T+V)$$

$$Q=m_1m_2(f_1-f_2)(K_3C_4-C_3K_4)$$

$$R=(m_1f_2-m_2f_1)(Y_3C_4-C_3Y_4)$$

$$S=(m_1f_1-m_2f_2)(X_3K_4-K_3X_4)$$

$$T=(m_1-m_2)[f_1f_2(C_3X_4-X_3C_4)+(K_3Y_4-Y_3K_4)]$$

$$V=(f_1-f_2)(Y_3X_4-X_3Y_4)$$

$$C_3=d_1e^{l_1Y_0}-d_2e^{l_2Y_0}+e^{l_3Y_0}$$

$$C_4=d_3e^{l_1Y_0}-d_4e^{l_2Y_0}+e^{l_4Y_0}$$

$$K_3=h_1d_1e^{l_1Y_0}-h_2d_2e^{l_2Y_0}+h_3e^{l_3Y_0}$$

$$K_4=h_1d_3e^{l_1Y_0}-h_2d_4e^{l_2Y_0}+h_4e^{l_4Y_0}$$

$$X_3=\frac{h_2-h_3}{h_1-h_2}l_3e^{l_1Y_0}-\frac{h_1-h_3}{h_1-h_2}l_3e^{l_2Y_0}+l_3e^{l_3Y_0}$$

$$X_4=\frac{h_2-h_4}{h_1-h_2}l_4e^{l_1Y_0}-\frac{h_1-h_4}{h_1-h_2}l_4e^{l_2Y_0}+l_4e^{l_4Y_0}$$

$$Y_3=\frac{h_2-h_3}{h_1-h_2}h_1l_3e^{l_1Y_0}-\frac{h_1-h_3}{h_1-h_2}h_2l_3e^{l_2Y_0}+h_3l_3e^{l_3Y_0}$$

$$Y_4=\frac{h_2-h_4}{h_1-h_2}h_1l_4e^{l_1Y_0}-\frac{h_1-h_4}{h_1-h_2}h_2l_4e^{l_2Y_0}+h_4l_4e^{l_4Y_0}$$

$$d_1=\frac{h_2-h_3}{h_1-h_2}\frac{l_3}{l_1},\quad d_2=\frac{h_1-h_3}{h_1-h_2}\frac{l_3}{l_2},\quad d_3=\frac{h_2-h_4}{h_1-h_2}\frac{l_4}{l_1},\quad d_4=\frac{h_1-h_4}{h_1-h_2}\frac{l_4}{l_2}$$

$$h_1=\left(\frac{A_2}{A_1}\right)_{l_1},\quad h_2=\left(\frac{A_2}{A_1}\right)_{l_2},\quad h_3=\left(\frac{A_2}{A_1}\right)_{l_3},\quad h_4=\left(\frac{A_2}{A_1}\right)_{l_4},\quad f_1=\left(\frac{A_2}{A_1}\right)_{m_1},\quad f_2=\left(\frac{A_2}{A_1}\right)_{m_2}.$$

See Table 4.1 for further definitions.

REFERENCES

Bernstein, R., and W. White, 1974: Time and length scales of baroclinic eddies in the central North Pacific. J. Phys. Oceanogr., 4, 613-624

----------, 1981: Stationary and traveling mesoscale perturbations in the Kuroshio Extension current. J. Phsy. Oceanogr., 11, 692-704

Emery, W. J., W. G. Lee, and L. Magaard, 1984: Geographic distributions of density, Brunt-Vaisala frequency and Rossby radii in the North Atlantic and North Pacific. J. Phys. Oceanogr., 14, 294-317

----------, and L. Magaard, 1976: Baroclinic Rossby waves as inferred from temperature fluctuations in the eastern Pacific. J. Mar. Res., 34, 365-385

Gill, A. E., J. S. A. Green, and A. J. Simmons, 1974: Energy partition in the large-scale oceanic circulation and the production of mid-ocean eddies. Deep-sea Res., 21, 499-528.

Harrison, D. E., W. J. Emery, J. P. Dugan, and B.-C. Li, 1983: Mid-latitude mesoscale temperature variability in six multiship XBT surveys. J. Phys. Oceanogr., 13, 648-662

Holland, W. R., and L. B. Lin, 1975: On the generation of mesoscale eddies and their contribution to the oceanic general circulation I. A preliminary numerical

experiment. J. Phys. Oceanogr., 5, 642-657.

Kang, Y. Q., J. M. Price, and L. Magaard, 1982: On stable and unstable Rossby waves in non-zonal oceanic shear flow. J. Phys. Oceanogr., 12, 528-537.

----------, and L. Magaard, 1980: Annual baroclinic Rossby waves in the central North Pacific. J. Phys. Oceanogr., 10, 1159-1167

Magaard, L., 1983: On the potential energy of baroclinic Rossby waves in the North Pacific. J. Phys. Oceanogr., 7, 41-49

McIntyre, M. E. and M. A. Weissman, 1978: On radiating instabilities and resonant over-reflection. J. Atmos. Sci., 35, 1190-1196.

Mizuno, K., and W. B. White, 1983: Annual and interannual variability in the Kuroshio current system. J. Phys. Oceanogr., 13, 1847-1867

Orlanski, I., and M. D. Cox, 1973: Baroclinic instability in ocean currents. Geophys. Fluid Dyn., 4, 297-332.

Pedlosky, J., 1975: The amplitude of baroclinic wave triads and mesoscale motion in the ocean. J. Phys. Oceanogr., 5, 608-614.

----------, 1977: On the radiation of mesoscale energy in the mid-ocean. Deep-Sea Res., 24, 591-600.

----------, 1979: Geophysical Fluid Dynamics. Springer-Verlag, 624 pp.

Price, J. M., and L. Magaard, 1980: Rossby wave analysis of

the baroclinic potential energy in the upper 500 meters of the North Pacific. J. Mar. Res., 38, 249-264

Rayleigh, Lord, 1879: On the instability of jets. Scientific Papers, 1, 474-487.

Robinson, A. R., and J. C. McWilliams, 1974: The baroclinic instability of the open ocean. J. Phys., Oceanogr., 4, 281-294.

Roden, G. I., 1977: On long-wave disturbances of dynamic height in the North Pacific. J. Phys. Oceanogr., 7, 41-49

Schmitz, W. J., 1984: Observations of the vertical structure of the eddy field in the Kuroshio Extension. J. Geophys. Res., 89, 6355-6364.

Talley, L. D., 1982: Instabilities and radiation of thin, baroclinic jets. Ph.D. Dissertation, MIT/WHOI Joint program, 233 pp.

White, W. B., 1977: Secular variability in the baroclinic structure of the interior North Pacific from 1950-1970. J. Mar. Res., 35, 3, 587-607

----------, 1982: Traveling wave-like mesoscale perturbations in the North Pacific. J. Phys. Oceanogr., 12, 231-243

----------, 1983: Westward propagation of short term climatic anomalies in the western North Pacific Ocean from 1964-1974. J. Mar. Res., 41, 113-125

----------, and L. Bernstein, 1979: Design of an

oceanographic network in the mid-latitude North Pacific. J. Phys. Oceanogr., 9, 592-606.

----------, and A. E. Walker, 1974: Time and depth scales of anomalous subsurface temperature at Ocean Weather Station P, N, and V in the North Pacific. J. Geophys. Res., 1979, 4517-4522

Wilson, W. S., and J. P. Dugan, 1978: Mesoscale thermal variability in the vicinity of the Kuroshio Extension. J. Phys. Oceangr., 8, 537-540.